

ANALYSIS OF AN INTERFEROMETRIC STOKES IMAGING POLARIMETER

by

Sukumar Murali

A Dissertation Submitted to the Faculty of the

COLLEGE OF OPTICAL SCIENCES

In Partial Fulfillment of the Requirements

For the Degree of

DOCTOR OF PHILOSOPHY

In the Graduate College

THE UNIVERSITY OF ARIZONA

2010

THE UNIVERSITY OF ARIZONA
GRADUATE COLLEGE

As members of the Dissertation Committee, we certify that we have read the dissertation prepared by Sukumar Murali entitled Analysis of an Interferometric Stokes Imaging Polarimeter and recommend that it be accepted as fulfilling the dissertation requirement for the Degree of Doctor of Philosophy.

Dr. David Tyler

Date: 29 October 2010

Dr. William Dallas

Date: 29 October 2010

Dr. Matthew Kupinski

Date: 29 October 2010

Final approval and acceptance of this dissertation is contingent upon the candidate's submission of the final copies of the dissertation to the Graduate College. I hereby certify that I have read this dissertation prepared under my direction and recommend that it be accepted as fulfilling the dissertation requirement.

Dissertation Director: Dr. David Tyler

Date: 29 October 2010

STATEMENT BY AUTHOR

This dissertation has been submitted in partial fulfillment of requirements for an advance degree at the University of Arizona and is deposited in the University Library to be made available to borrowers under rules of the Library.

Brief quotations from this dissertation are allowable without special permission, provided that accurate acknowledgement of source is made. Requests for permission for extended quotation from or reproduction of this manuscript in whole or in part may be granted by the head of the major department or the Dean of the Graduate College when in his or her judgement the proposed use of the material is in the interests of scholarship. In all other instances, however, permission must be obtained from the author.

Sukumar Murali

ACKNOWLEDGMENTS

My graduate school experience at the College of Optical Sciences has been wonderful and a rewarding one. There are a number of people to whom i wish to express my heartfelt gratitude.

First and foremost, I wish to acknowledge my advisor **Dr. David Tyler** and his wife **Mrs. Lyn Tyler** for their kindness, generosity and care towards me over the past decade. Thank you both for making me a part of your family and supporting me through difficult times.

Dr. David Tyler has been a critical influence on my academic career and personal development. He has been a friend, philosopher, and most importantly, an excellent advisor. I have always admired his patience, tolerance, enthusiasm, ability to motivate and bring the best out of me. His growth as a researcher, intuitive insights, quick grasp of difficult problems and providing elegant solutions have amazed me over the years. Thank you for all you have done to help me realize this day.

Many thanks to my committee members **Dr. William Dallas**, and **Dr. Matthew Kupinski** for agreeing to be a part of the dissertation panel, taking the time to review my dissertation, and being flexible with the time constraints I faced.

I would like to thank **Dr. Russell Chipman** for teaching me the concepts in polarization, reviewing my dissertation, and providing me with useful suggestions. I owe a lot of my understanding of polarization to the discussions with his group members, **Dr. Karlton Crabtree** in particular for his patient listening, great ideas, and suggestions.

The support of my friends **Hariharan Muralimanohar**, **Omjyoti Dutta**, **Corrie Hannah**, **Rania Abdel Maksoud**, **Brian Miller**, **Eliaz Martinez**, and **Jihun Kim** means more than i can say. They have had a significant influence through their association which has helped me improve in many aspects of my personal life. A special thanks to **Corrie Hannah**, **Paula Smith**, and **Edith Rappaport** for proofreading my manuscript and making me look good on paper.

Thanks are due to **Mr. Dan O'Connell** of Hnu photonics for providing me an opportunity to apply some of my Optics knowledge in an industrial setting. Thank you for your kindness and support.

My undying gratitude is reserved for the administrative staff of the College of Optical Sciences - **Bobbie Doss**, **Stella Hosteller**, **Gail Varin**, **Kina Adams**, **Juliet Hughes**, **Tammy Orr**, **Didi Lawson**, **Allison Huff MacPherson** and **Anabel Garcia**. Thank you for your excellent work on my behalf and helping me out in more than a few difficulties.

Finally, **Dr. Samuel Stearns** (Sandia National Labs and University of New Mexico) was instrumental in seeing that i continue my graduate work leading to my PhD in Optical Sciences for which i feel most fortunate.

DEDICATION

To my wonderful parents, Varalakshmi Neelakantam (Amma) and Murali Balakrishnan (Daddy), the reason for my existence in this universe. I thank them for their support and teaching me the fundamental principles of adjustment, tolerance, and sacrifice through their own lives.

“Vazhga Valamudan”

TABLE OF CONTENTS

LIST OF TABLES	8
LIST OF FIGURES	9
NOMENCLATURE	12
ABSTRACT	17
CHAPTER 1 INTRODUCTION	19
CHAPTER 2 BIREFRINGENT CRYSTAL ASSEMBLY	30
2.1 Physical and functional description of a BCA	32
2.2 BCA configurations used in other ISIPs	36
CHAPTER 3 SIMULATION DESCRIPTION	40
3.1 A telescope model - monochromatic illumination	41
3.2 BCA models	45
3.2.1 Mueller Model	46
3.2.2 Jones Model	52
3.2.3 Comparison of Mueller and Jones BCA models	55
3.3 Modeling finite spectral bandwidth	56
3.4 A detector model with noise effects	59
3.5 User inputs	64
3.6 IDL implementation	67
3.7 Simulation example	69
CHAPTER 4 RECONSTRUCTOR ALGORITHM	72
4.1 Unit cell, polarization domain, pixel and detector geometry	73
4.2 Reconstruction based on Mueller approach	76
4.3 Reconstruction of calibration fringes	86
CHAPTER 5 SAMPLING REQUIREMENTS	90
5.1 Tracing rays, pixel size and detector model	91
5.2 Singular value decomposition and condition numbers	97
5.3 Choosing pixel sizes, wedge angles and unit cells using condition number as a metric	103
5.4 Nyquist Sampling the PSF	119

TABLE OF CONTENTS – *Continued*

CHAPTER 6	BIAS-VARIANCE TRADEOFF AND SENSITIVITY ANALYSIS . . .	129
6.1	Bias-variance tradeoff : Choosing unit cell size	133
6.2	Bias-variance tradeoff: Dispersion effects	155
6.3	Sensitivity analysis: Shot noise limited detection	176
6.3.1	Design Considerations	181
CHAPTER 7	SUMMARY, CONCLUSIONS, AND RECOMMENDATIONS	187
REFERENCES	192

LIST OF TABLES

3.1	Transmission of the BCA.	69
5.1	Angle between the rows of the measurement matrix corresponding to the largest condition number: 12027.655 (2 X 2 unit cell case).	111
5.2	Unit cells of the calibration fringes corresponding to the largest condition number: 12027.655	112
5.3	Unit cells of the calibration fringes corresponding to the condition number: 10.6	112
5.4	Unit cells of the calibration fringes corresponding to the condition number: 66.46	113
5.6	Statistics on the condition number arrays in oversampled cases (2 X 2 unit cell).	115
6.1	SNR values for detector images obtained at various object brightness levels.	139
6.2	Average number of PDE per pixel at various brightness levels of point source, flat field, and satellite object.	140

LIST OF FIGURES

1.1	Pattern of linear polarizers (taken from [32]).	21
1.2	Four channel polarimeter (taken from [32]).	23
1.3	Four detector photo polarimeter (taken from [32]).	24
1.4	A simultaneous polarimetric imaging configuration.	25
2.1	Birefringent Crystal Assembly.	31
2.2	Visibility of fringe patterns.	33
2.3	BCA configuration used by Oka (taken from [36]).	37
2.4	BCA using Savart plates (taken from [39]).	37
3.1	Telescope model.	42
3.2	Calibration fringes and difference images.	56
3.3	Broad band imaging effects on the horizontal calibration fringes. . . .	57
3.4	Simulation object and images at various stages.	70
4.1	Geometry of the detector, unit cell and idea of a polarization domain. .	74
4.2	Pixel representation in a unit cell.	78
4.3	Reconstruction technique.	81
4.4	Circular object and fringe modulated image.	82
4.5	Reconstructed Stokes images using a 3 X 3 unit cell.	84
4.6	Comparison of reconstruction methods.	85
4.7	Reconstruction of horizontal calibration fringes.	87
4.8	Reconstruction of 45 calibration fringes.	87
4.9	Reconstruction of RHC calibration fringes.	88
4.10	Reconstruction of a generic fringe pattern.	88
5.1	Magnitude of Fourier spectrum of the calibration fringes.	93
5.2	The changes in position of side lobe as function of the wedge angle. .	95
5.3	Nyquist sampled calibration fringes.	98
5.4	Mean and std-dev condition number for a unit cell size 2 X 2.	106
5.5	Natural log of condition number array surface (2D) for the 2 X 2 unit cell at Nyquist sampling.	107
5.6	Natural log of condition number array surface (3D) for the 2 X 2 unit cell at Nyquist sampling.	108
5.7	Metrics of condition number arrays for a unit cell size 3 X 3.	116
5.8	Condition numbers of larger unit cells.	118
5.9	Nyquist sampling the PSF.	120

LIST OF FIGURES – *Continued*

5.10	Point source images: True image and Fringe modulated image.	121
5.11	Reconstructed Stokes images of the point source.	121
5.12	Error metric as a function of number of unit cells sampling 1.22λ $F/\#$	123
5.13	Magnitude of the Fourier transform of a point source (PSF width - $1.22 \times \lambda \times F/\# = 16$ pixels).	125
5.14	Magnitude of the Fourier transform of a point source (PSF width - $1.22 \times \lambda \times F/\# = 7$ pixels).	126
5.15	Effect of varying PSFs in the Fourier domain.	127
6.1	Objects used in the imaging.	136
6.2	Noisy images: Point source Left to Right: 10^4 PDE, 10^5 PDE, 10^6 PDE, and 10^7 PDE.	137
6.3	Noisy images: Satellite object Top to Bottom: 10^5 PDE, 10^6 PDE, 10^7 PDE, and 10^8 PDE.	137
6.4	Noisy images: Flat field Top to Bottom: 10^6 PDE, 10^7 PDE, 10^8 PDE, and 10^9 PDE.	138
6.5	Point source: MSE, bias, and variance curves (10^4 PDE).	142
6.6	Point source: MSE, bias, and variance curves (10^5 PDE).	143
6.7	Point source: MSE, bias, and variance curves (10^6 PDE).	144
6.8	Point source: MSE, bias, and variance curves (10^7 PDE).	145
6.9	Flat field: MSE, bias, and variance curves (10^6 PDE).	146
6.10	Flat field: MSE, bias, and variance curves (10^7 PDE).	147
6.11	Flat field: MSE, bias, and variance curves (10^8 PDE).	148
6.12	Flat field: MSE, bias, and variance curves (10^9 PDE).	149
6.13	Satellite object: MSE, bias, and variance curves (10^5 PDE).	150
6.14	Satellite object: MSE, bias, and variance curves (10^6 PDE).	151
6.15	Satellite object: MSE, bias, and variance curves (10^7 PDE).	152
6.16	Satellite object : MSE, bias, and variance curves (10^8 PDE).	153
6.17	Dispersion effects of the BCA.	156
6.18	Region 1: Normalized MSE, Normalized Bias, and Normalized Vari- ance - 10^5 PDE.	158
6.19	Region 2: Normalized MSE, Normalized Bias, and Normalized Vari- ance - 10^5 PDE.	159
6.20	Region 3: Normalized MSE, Normalized Bias, and Normalized Vari- ance - 10^5 PDE.	160
6.21	Region 4: Normalized MSE, Normalized Bias, and Normalized Vari- ance - 10^5 PDE.	161
6.22	Region 1: Normalized MSE, Normalized Bias, and Normalized Vari- ance - 10^6 PDE.	162
6.23	Region 2: Normalized MSE, Normalized Bias, and Normalized Vari- ance - 10^6 PDE.	163

LIST OF FIGURES – *Continued*

6.24	Region 3: Normalized MSE, Normalized Bias, and Normalized Variance - 10^6 PDE.	164
6.25	Region 4: Normalized MSE, Normalized Bias, and Normalized Variance - 10^6 PDE.	165
6.26	Region 1: Normalized MSE, Normalized Bias, and Normalized Variance - 10^7 PDE.	166
6.27	Region 2: Normalized MSE, Normalized Bias, and Normalized Variance - 10^7 PDE.	167
6.28	Region 3: Normalized MSE, Normalized Bias, and Normalized Variance - 10^7 PDE.	168
6.29	Region 4: Normalized MSE, Normalized Bias, and Normalized Variance - 10^7 PDE.	169
6.30	Region 1: Normalized MSE, Normalized Bias, and Normalized Variance - 10^8 PDE.	170
6.31	Region 2: Normalized MSE, Normalized Bias, and Normalized Variance - 10^8 PDE.	171
6.32	Region 3: Normalized MSE, Normalized Bias, and Normalized Variance - 10^8 PDE.	172
6.33	Region 4: Normalized MSE, Normalized Bias, and Normalized Variance - 10^8 PDE.	173
6.34	Signal to Noise Ratio (SNR) as a function of source DOP (shot noise limited case).	178
6.35	Signal to Noise Ratio (SNR) as a function of change in DOP due to unpolarized background (shot noise limited case).	179
6.36	Visibility of Fringes obtained for linearly polarized input light.	185
7.1	Potential uses of Fourier approach and Slide reconstruction spatial approach.	190

NOMENCLATURE

θ_r	Angular resolution of the telescope.
BCA	Birefringent Crystal Assembly.
θ_{CA}	Orientation of the crystal axis with respect to the x axis.
C_n	Calibration fringe pattern associated with the nth polarization state.
D	Telescope diameter.
$d\lambda$	Bandwidth of the light allowed in the ISIP.
DOP	Degree Of Polarization.
$\vec{\mathbf{E}}$	Electric field.
E_x	x component of the Electric field.
E_y	y component of the Electric field.
EM	Error Metric.
e-ray	Extra-ordinary ray.
\mathbf{F}	Measurement matrix.
F_1	Second element of the first row of the ISIP Mueller matrix .
F_2	Third element of the first row of the ISIP Mueller matrix .
F_3	Fourth element of the first row of the ISIP Mueller matrix .

f_s	Sampling frequency.
F_0	First element of the first row of the ISIP Mueller matrix .
f_{max}	Maximum spatial frequency.
F_{mn}	Measurement matrix element of the nth polarization state derived from the mth pixel of an unit cell.
FFT	Fast Fourier Transform.
HWR	Half Wave Retarder.
im	Image function.
IFOV	Instantaneous Field Of View.
im	Image function.
ISIP	Interferometric Stokes Imaging Polarimeter.
J	Jones matrix.
λ	Wavelength of light used.
LHC	Left Hand Circular.
M	Total number of pixels in the unit cell.
MSE	Mean Square Error.
M	Mueller matrix .
$NMSE$	Normalized Mean Square Error.
n_e	Extra-ordinary refractive index.

n_o	Ordinary refractive index.
$\vec{\mathbf{O}}$	Vector formed from pixel measurements.
ob	Object function.
o-ray	Ordinary ray.
OPD	Optical path difference.
OTF	Optical Transfer Function.
ϕ	Phase difference or Phase shift.
P_{incoh}	Incoherent Transfer Function.
p_{incoh}	Incoherent Point Spread Function.
PAB	Pixel Averaged Bias.
$PANB$	Pixel Averaged Normalized Bias.
$PANV$	Pixel Averaged Normalized Variance.
PAV	Pixel Averaged Variance.
PBS	Polarizing Beam Splitter.
PDE	Photon Detection Events.
PSF	Point Spread Function.
PSG	Polarization State Generator.
QWR	Quarter Wave Retarder.

R	Product of the normalized ratio surfaces.
R_1	Ratio surface constructed from horizontal and 45 calibration fringes.
R_2	Ratio surface constructed from 45 and RHC calibration fringes.
R_3	Ratio surface constructed from horizontal and RHC calibration fringes.
RSI	Reconstructed Stokes Image.
RHC	Right Hand Circular.
RMS	Root Mean Squared.
\vec{S}	Stokes vector
$\vec{\hat{S}}$	Estimated Stokes vector.
σ	Singular value.
\tilde{S}_0	Estimation of the 1st Stokes component.
\tilde{S}_1	Estimation of the 2nd Stokes component.
\tilde{S}_2	Estimation of the 3rd Stokes component.
\tilde{S}_3	Estimation of the 4th Stokes component.
S_0	1st Stokes component.
S_1	2nd Stokes component.
S_2	3rd Stokes component.
S_3	4th Stokes component.

SNR Signal to Noise Ratio.

SOP State Of Polarization.

SVR Spatially Varying Retarder.

θ Orientation of the fast-axis in the spatially varying retarder.

θ_{TA} Orientation of the transmission axis of the linear polarizer with respect to the x-axis.

T_{pupil} Fourier transform of the telescope pupil function.

t_{pupil} Transmittance of the telescope pupil function.

TSI True Stoke Image.

θ_{wp} Orientation of the wedgeplane with respect to the x-axis.

$\overrightarrow{U_H}$ Vector constructed from 45 calibration unit cell.

$\overrightarrow{U_H}$ Vector constructed from horizontal unit cell.

$\overrightarrow{U_{RHC}}$ Vector constructed from RHC calibration unit cell.

V_{45} Visibility of 45 calibration fringes.

V_H Visibility of horizontal calibration fringes.

V_{RHC} Visibility of RHC calibration fringes.

Θ Wedge angle of the SVR.

ABSTRACT

Estimation of Stokes vector components from an interferometric fringe encoded image is a novel way of measuring the State Of Polarization (SOP) distribution across a scene. Imaging polarimeters employing interferometric techniques encode SOP information across a scene in a single image in the form of intensity fringes. The lack of moving parts and use of a single image eliminates the problems of conventional polarimetry - vibration, spurious signal generation due to artifacts, beam wander, and need for registration routines. However, interferometric polarimeters are limited by narrow bandpass and short exposure time operations which decrease the Signal to Noise Ratio (SNR) defined as the ratio of the mean photon count to the standard deviation in the detected image.

A simulation environment for designing an Interferometric Stokes Imaging polarimeter (ISIP) and a detector with noise effects is created and presented. Users of this environment are capable of imaging an object with defined SOP through an ISIP onto a detector producing a digitized image output. The simulation also includes bandpass imaging capabilities, control of detector noise, and object brightness levels.

The Stokes images are estimated from a fringe encoded image of a scene by means of a reconstructor algorithm. A spatial domain methodology involving the idea of a unit cell and slide approach is applied to the reconstructor model developed using Mueller calculus. The validation of this methodology and effectiveness compared to a discrete approach is demonstrated with suitable examples. The pixel size required to sample the fringes and minimum unit cell size required for reconstruction are investigated using condition numbers. The importance of the PSF of fore-optics (telescope) used in imaging the object is investigated and analyzed using a point source imaging example and a Nyquist criteria is presented.

Reconstruction of fringe modulated images in the presence of noise involves choosing an optimal sized unit cell. The choice of the unit cell based on the size of the polarization domain and illumination level is analyzed using a bias-variance tradeoff to obtain the minimum Mean Square Error. A similar tradeoff study is used to analyze the choice of the bandpass filters under various illumination levels. Finally, a sensitivity analysis of the ISIP is presented to explore the applicability of this device to detect low degrees of polarization in areas such as remote sensing.

CHAPTER 1

INTRODUCTION

Imaging polarimetry is an emerging technology that is finding increasing applications in the field of remote sensing, medicine, machine vision, bio sciences, and solar astronomy across a wide range of wavelength - ultra violet (UV) to infra red (IR). Polarization is one of the fundamental physical quantities that characterize electromagnetic fields while others are wavelength, intensity and coherence [1]. Polarization measurements yield unique information about the vector nature of the optical radiation measured across a scene. This information is different from the intensity and spectral measurements from the scene [1]. Intensity measurements indicate the magnitude of flux in the wavelength range measured and spectral measurements, hyper-spectral and multi-spectral imaging, indicate the distribution of power over wavelength. Polarization measurements have been used study surface roughness [2], geometry [3], measure stress and spatio-temporal birefringence [4, 5], target detection in scattering and turbid media [6], reduce clutter [7], enhance contrast [1], and even help with the diagnosis of retinas with pathology [8].

Polarization of an optical field can be represented by means a Jones vector in case of coherent field or a Stokes vector in case of incoherent radiation. However, applications of passive polarimetry like remote sensing where the source is not controlled, the polarization information is represented by means of Stokes vector images of the scene being imaged. The Stokes vector can be written as follows:

$$\vec{S}(x, y) = \begin{bmatrix} S_0(x, y) \\ S_1(x, y) \\ S_2(x, y) \\ S_3(x, y) \end{bmatrix} = \begin{bmatrix} I_H(x, y) + I_V(x, y) \\ I_H(x, y) - I_V(x, y) \\ I_{45}(x, y) - I_{135}(x, y) \\ I_{RHC}(x, y) - I_{LHC}(x, y) \end{bmatrix} \quad (1.1)$$

where (x, y) indicates the spatial dependence of the energy from the scene. $I_H, I_V, I_{45}, I_{135}, I_{RHC}$ and I_{LHC} represent the horizontal, vertical, 45, 135, right hand circular (RHC) and left hand circular (LHC) polarized energies from the scenes. The Stokes vector elements are formed from time averaged intensities and sign of the individual elements (S_1, S_2 , and S_3) in the Stokes vector indicates the dominating energy from a particular polarization compared to its orthogonal counterpart. For example, a positive sign and a non-zero value of the Stokes component S_1 indicates dominating energy from the horizontally polarized component of the source compared to the energy from the vertically polarized component. By definition in Equation 1.1 it is apparent that the computation of Stokes vector images from a scene requires multiple images or a single image must contain more information than found in a conventional system. Using multiple images obtained with a linear polarizer and a combination of a linear polarizer and a quarter wave retarder at various transmission axis and fast axis orientations in front of the detector is a conventional way to compute the Stokes vectors.

Polarization optics normally reduce the throughput of the system which causes a reduction in the Signal to Noise Ratio (SNR) which can be compensated for by long exposure times or multiple measurements either of which may not be a concern in active polarimetry like ellipsometry and Mueller matrix polarimetry. However, Stokes imaging polarimeters used in remote sensing may be so limited by practical aspects of real time imagery which require short exposure times, such as motion of objects in the

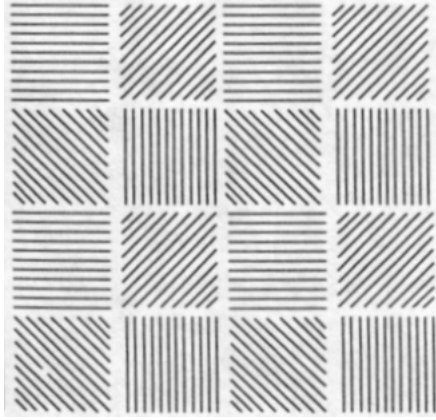


Figure 1.1: Pattern of linear polarizers (taken from [32]).

scene or motion of the sensor relative to the scene. The images recorded by a Stokes polarimeter for polarimetric estimation must be made under similar conditions of source-scene geometry, illumination levels and without any scene changes in between image measurements. Conventional time sequential Stokes polarimeters employing rotating retarders and polarizers require motorized stages that can introduce vibrations apart from increasing the volume and complexity of the measurement system. Moreover, the rotation systems are prone to vibration inducing beam wander. The image shifts due to vibrations or beam wander causes the polarimetric data reduction process to introduce artifacts in the Stokes images. In fact, image misregistration of the order of $1/20^{th}$ of a pixel have been shown to cause artifacts in the polarization images [9] and registration algorithms [10] are required to correct for the rotation and translation of the images.

Polarimeters enabling simultaneous measurement of Stokes vector elements can be categorized into division of wave front [11, 12, 13, 14, 15, 16, 17, 18, 19, 20] and division of amplitude polarimeters [21, 22, 23, 24, 25, 26, 27, 28, 29, 30, 31]. In division of wave front polarimeters measurements are made across the wave front at different locations without any division in amplitude and in division of amplitude polarimeters

the energy in the wave front is divided and passed through various polarization optics before incident onto a detector.

An example of the division of wave front polarimeter is the division of focal plane array (FPA) polarimeter [32] which has found its applications in a wide range of spectrum - visible, short wave infra red (SWIR) and long wave infra red (LWIR) [1]. In this polarimeter, a linear polarizer array with a pattern like the one shown in Figure 1.1 is formed on a substrate using micro lithography and placed in front of the detector. Each linear polarizer is about the size of a detector pixel and makes a polarization measurement in a part of the wave front. Linear polarizers with four different transmission axis orientations are adjacent to each other and combine together to form a super pixel which assumes that the polarization of the incoming light does not vary much over the four linear polarizers. There are no circular polarization components measured and hence this is an incomplete polarimeter. This polarimeter requires more pixels compared to other polarimeters to represent the image and Stokes parameters associated with a particular field of view. It also suffers from artifacts due to intensity gradients and instantaneous field of view (IFOV) errors. The films laid over the pixels can lead to small errors (IFOV) where the pixels in a unit cell do not point in the same direction

One example of the division of amplitude polarimeter capable of measuring all four Stokes components at all pixel locations is the four channel polarimeter shown in Figure 1.2. This polarimeter has two polarization beam splitters (PBS), a half wave retarder (HWR- fast axis oriented at 22.5 degrees with respect to x axis), a quarter wave retarder (QWR-fast axis oriented at 45 degrees with respect to x axis) and four detectors. The PBS used in this configuration [32] have 80 % and 20 % transmissions for the parallel and perpendicular components. A calibration procedure determines the transfer Mueller matrix which is then used along with the detector measurements

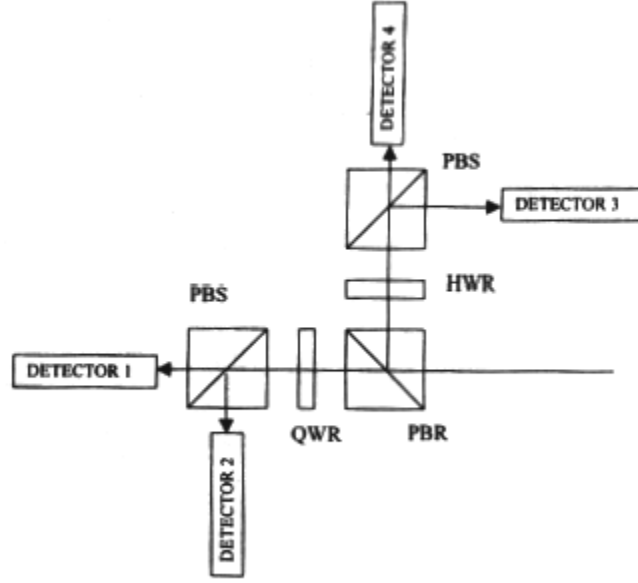


Figure 1.2: Four channel polarimeter (taken from [32]).

to reconstruct the incident Stokes vector elements. The mechanical alignment to the required tolerances, spatial registration issues, complexity and size of this system are the main drawbacks of this kind of polarimeter.

Another example of the division of amplitude polarimeter is the four detector photopolarimeter shown in Figure 1.3. The input light beam is incident on each of the detectors sequentially. Each time the incident light encounters detectors D1, D2, and D3 a part of the light is absorbed and the other part is specularly reflected to the remaining detectors. The reflection of detector D4 is minimal and absorbs most of the light incident on it. The light absorbed by the detectors is a linear combination of the Stokes components of the input light. The output of each of the detectors is related to the Stokes vector of incident light by a Mueller matrix. The four detected signals are related to the input Stokes vector by the following relation:

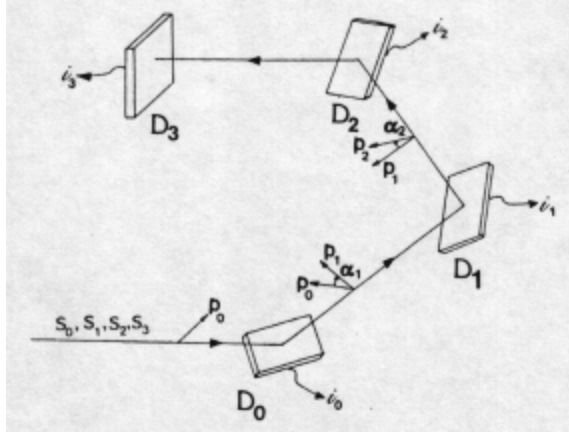


Figure 1.3: Four detector photo polarimeter (taken from [32]).

$$\mathbf{I} = \begin{bmatrix} i_0 \\ i_1 \\ i_2 \\ i_3 \end{bmatrix} = \mathbf{A} \begin{bmatrix} S_0 \\ S_1 \\ S_2 \\ S_3 \end{bmatrix}$$

Where \mathbf{I} is the vector of detector measurements and \mathbf{A} is the Mueller matrix of the instrument. The incident Stokes components are then reconstructed from:

$$\vec{\tilde{\mathbf{S}}} = \mathbf{A}^{-1}\mathbf{I}$$

where $\vec{\tilde{\mathbf{S}}}$ is the estimated Stokes vector. This polarimeter is not generally used for imaging and any modifications of this system to accommodate imaging applications can be challenging.

Other polarimeters [32] that can perform simultaneous Stokes vector measurements are Photopolarimeter using conical diffraction, Photopolarimeter using planar diffraction and Parallel slab polarimeter. Like the four detector Photopolarimeter these polarimeters are more suited for active polarimetry and would require considerable modifications before they could be used for imaging polarimetry in areas like

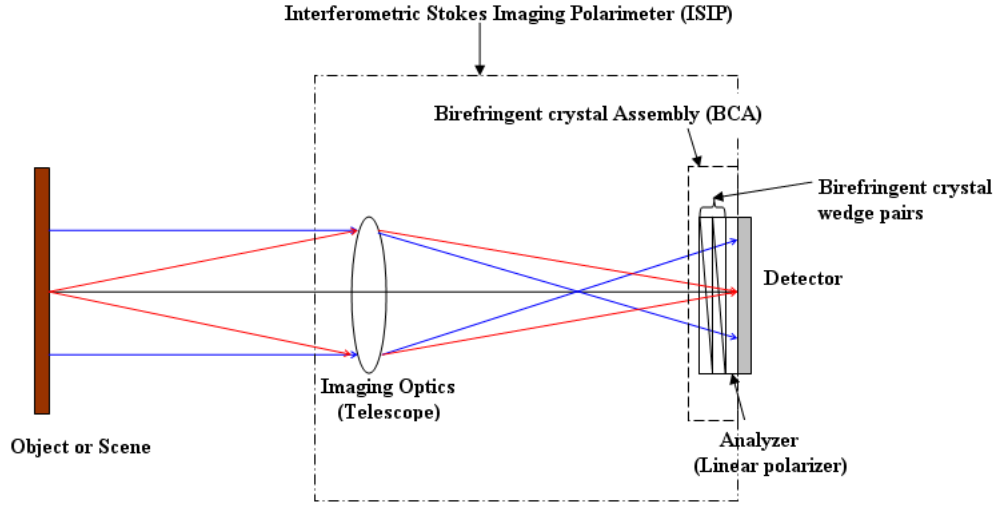


Figure 1.4: A simultaneous polarimetric imaging configuration.

remote sensing.

One of the novel methods that enable simultaneous measurement of Stokes vector components is the interferometric imaging polarimetry that encodes polarization information in the form of intensity fringes [34, 36]. This method of encoding polarization information provides simultaneous measurement of both time dependent State Of Polarization (SOP) and space dependent SOP across the scene of interest. A configuration of the Interferometric Stokes Imaging Polarimeter (ISIP) is shown in Figure 1.4.

The basic unit that provides this polarimeter the simultaneous imaging capability is the Birefringent Crystal Assembly (BCA) which consists of four birefringent crystal wedges combined to form two spatially varying retarders, and an analyzer (linear polarizer). The BCA is placed at the focal plane of an imaging optical system - a telescope and aligned with the field of view of the telescope. The image of an object or a scene from the telescope is incident on the front face of the BCA and a polarization dependent fringe modulated image exits the rear face of the BCA. A description of

the construction and working principle of the BCA along with the variations in the BCA used by researchers are provided in Chapter 2.

The telescope along with the BCA forms the Interferometric Stokes Imaging Polarimeter (ISIP) (Figure 1.4) which maps the SOP of the incoming light from an object or scene into a fringe modulated image. The shapes of the fringes in the image depend on the fast axis orientations of the SVRs, transmission axis of linear polarizer (analyzer) and polarization of incident light. The spatial period of these fringes are inversely related to the wedge angle of the spatially varying retarders in the BCA. The fringe modulation is recorded by a detector array of pixels. The fringe modulated image is usually corrupted by noise from the detector and its associated electronic circuitry during the process of digitization. The process of designing an optimal configuration for an ISIP involves choosing right values for the BCA - wedge angles and thickness of the spatially varying retarders, and telescope design parameters - field of view, diameter of the entrance pupil and focal length, and detector design parameters - pixel size and array dimension.

Analysis of a fringe modulated image for various settings of these physical design parameters is feasible with simulation models of the BCA, telescope and detector. A simulation environment capable of creating models for each of the ISIP components with user defined parameters is created in IDL and presented in Chapter 3. While telescope and detector models are straightforward, the BCA model requires the knowledge of Mueller matrices of the individual elements forming the BCA. Apart from studying isolated effects on the output image like changes in fringe frequency with wedge angle, the simulation also provides capabilities to image a user defined object with defined SOP, including detector noise, broad band effects, and effects of frame integration time.

The fringe modulated image from the detector has to be reconstructed into Stokes

images in order to display the polarization content in the object or scene. This process is achieved by means of a reconstructor algorithm which employs matrix inversion or Fourier domain approaches. The basic methodology in the reconstruction algorithm used in this work is similar to the previous work [34]. However, a new Mueller model for the spatially varying retarders in the BCA and a slide approach are used in the reconstruction procedure. The effectiveness of the reconstruction algorithm and the improved performance of the slide approach over the conventional discrete approach is demonstrated with reconstruction examples of calibration fringe and generic fringe patterns. Calibration fringe patterns are the basic images obtained during the calibration procedure by illuminating the BCA with light beams of known uniform polarization and intensity. These images are required to derive the elements of the measurement matrix and hence the synthesis matrix used in the reconstruction procedure. Development of the algorithm, the idea of a unit cell, slide approach and reconstruction examples of the calibration fringe and generic fringe patterns are presented in Chapter 4.

Fringes that encode the polarization information are sampled by the detector pixels that have finite physical size. In order to produce a faithful reconstruction of the polarization information it is important that the detector pixels record the fringe modulations accurately. The size of the detector pixels should be chosen to at least Nyquist sample the fringes for a faithful reconstruction of the Stokes vector components. The fringes can be Nyquist sampled by either fixing the wedge angle of the spatially varying retarders and choosing a suitable pixel size or vice versa. The sampling requirements for the ISIP configuration forms the main topic of analysis and discussion of Chapter 5.

The reconstruction procedure with measurement matrices formed from unit cell size of 2×2 is shown to have high condition numbers for fringes of varying spatial

frequencies including Nyquist and hence not suited for the reconstruction procedure as it can produce huge errors in the estimated Stokes images in the presence of noise. The minimum size of the unit cell required for reconstruction with Nyquist sampled fringes is shown to be 3×3 . Finally, the importance of choosing a unit cell size that Nyquist samples the Point Spread Function (PSF) of the imaging optics (telescope) is discussed and demonstrated with a point source imaging example.

Measurements from most polarization sensing optical systems are corrupted by the noise of detector and its associated circuitry which decreases the *SNR* in the detections. To overcome this problem either multiple measurements or long exposure times can be used. However, long integration time is not an attractive feature in remote sensing applications for which the ISIP is being considered. Using multiple measurements to overcome noise effects translates to using unit cells with increased number of pixels in the reconstruction procedure. Although large unit cells ($> 3 \times 3$) decrease the noise effects (variance), there is an accompanying increase in reconstruction errors (bias) and loss in spatial resolution. The terms bias and reconstruction error essentially mean the same and the choice of one over the other will depend on the context of the discussion. The choice of unit cells with dimensions $> 3 \times 3$ in the reconstruction of Stokes images under various noise levels is investigated using a bias-variance tradeoff statistical approach which forms the first part of Chapter 6.

In the second part of Chapter 6, a similar approach is used to analyze reconstructions of fringe modulated images obtained when the light emitted or reflected by the object or scene has energy over a broad band. The fringe encoded image formed under broad illumination suffers from spatially periodic loss of visibility. The loss in visibility with bandwidth is a characteristic on any interferometer. In the ISIP the loss is due to the interference of multiple intensity fringe patterns of varying spatial frequency formed due to the dispersive nature of the birefringent crystals in the ISIP.

This problem is countered by the use of a bandpass filter in the ISIP that limits the spectral range over which the energy is collected by the ISIP. A larger bandwidth implies less variance and an increase in bias due to the loss in visibility of the fringes. Given the knowledge of source brightness and spectra of the source or scene, a bias-variance tradeoff study for the broadband imaging case helps in the choice of an optimal bandpass filter.

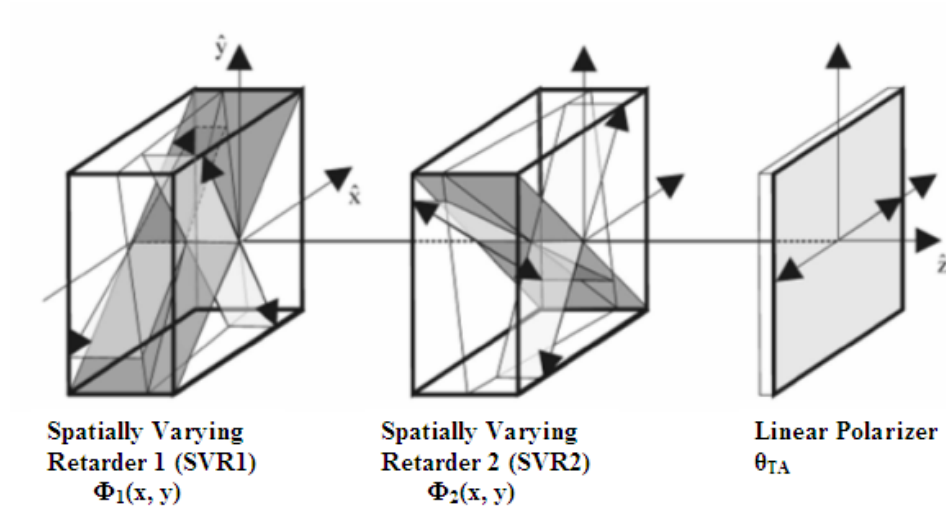
Finally, the sensitivity of the ISIP is analyzed for shot noise limited detections. Sensitivity of a polarimeter [33] in general is defined in terms of the minimum detectable polarization which is the minimum detectable modulated flux (polarized energy from the source) against the statistical fluctuations from the unpolarized background. The modulated flux in the case of the ISIP is the fringe modulations, the depth of which ideally is equal to the Degree Of Polarization (DOP) of incident light from the object or scene. Detection of the fringe modulations can be challenging in cases where the unpolarized energy collected from background exceeds the polarized energy from source or when the energy emitted or reflected from the source or object has a $DOP < 1$. In both cases the magnitude of polarized flux with respect to the total incident flux on the entrance face of the BCA is greatly reduced and the fringe modulations from the polarized flux gets corrupted by the shot noise fluctuations from the unpolarized portion. In the last part of Chapter 6 both cases of decrease in DOP along with shot noise effects are considered and the Signal to Noise Ratio (SNR) will be defined. The SNR of the estimations are analyzed as a function of the DOP. The magnitude of the SNR variation with DOP is a decisive factor in the applicability of the ISIP for measurements in the fields of both active and passive polarimetry.

CHAPTER 2

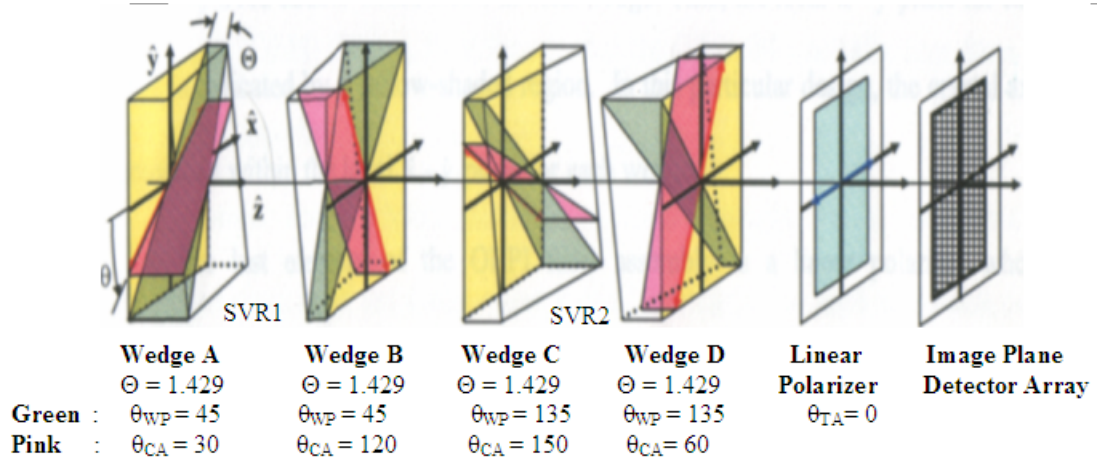
BIREFRINGENT CRYSTAL ASSEMBLY

The Interferometric Stokes Imaging Polarimeter (ISIP) is a common path interferometer that encodes all the polarization information into a single image [34, 36]. This imaging polarimeter has no moving parts and does not require users to register the images to produce Stokes vector components. The ISIP is a novel device, and while it certainly has some important limitations, it does not suffer from the same problems of conventional Stokes polarimeters (see Chapter 1). The ISIP consists of 1) fore-optics (telescope) that image an object or scene 2) BCA and 3) a detector that records the BCA traversed fringe modulated image. The terms fore-optics and telescope will be used interchangeably throughout this work depending on the context of the discussion. The BCA is the primary component that makes the ISIP a snapshot polarimeter. Hence a functional and physical description of the BCA is important in order to understand the working principle of the ISIP. The simulation model of the BCA used in this work is based on Jay S. Van Delden's polarimeter [34]. In this Chapter the following aspects of the polarimeter are described:

- Physical and functional description of a BCA.
- BCA configurations used in other ISIPs.



(a) Layout of the BCA (taken from [34]).



(b) A Realization of the BCA (taken from [35]).

Figure 2.1: Birefringent Crystal Assembly.

2.1 Physical and functional description of a BCA

The layout of a BCA is shown in Figure 2.1a. The BCA consists of two spatially varying retarders (SVRs), SVR 1, SVR 2, and a linear polarizer as in Figure 2.1a. Both retarders are constructed from uniaxial birefringent crystals. The double headed arrows in Figure 2.1a indicate orientation of axis based on the optical element. These arrows are along the direction of the crystal axis in the case of wedges and in the linear polarizer, they indicate the orientation of the transmission axis. Single headed arrows at each optical element in Figure 2.1a show the directions of the cartesian coordinates x and y . Each of the spatially varying retarders is made of two wedges with a common wedge plane. The direction of the wedge planes in SVR 1 and SVR 2 make 45 degrees and 135 degrees with the x axis respectively and is shown as θ_{wp} under each retarder in Figure 2.1b. The angles between the wedge planes and x axis do not matter as long as the relative wedge angle of the SVRs is 90 degrees as it provides a spatial varying phase retardation in orthogonal directions. The wedges in SVR 1 and SVR 2 are cut in such a way so as the crystal axis in each wedge is orthogonal to the other. A light ray seeing refractive index n_e in the first wedge would see n_o in the second wedge and vice versa. In Figure 2.1b the crystal axis and its corresponding plane in each wedge are shown in pink while the wedge plane in each wedge is shown in green. The crystal axes of the first and second wedges which form SVR 1, make 30 degrees and 120 degree angles with respect to x axis. Similarly, in SVR 2, the crystal axis of the first and second wedges make 150 degrees and 60 degrees with respect to the x axis. The angle of the crystal axis with respect to the x axis in each wedge is shown in Figure 2.1b (θ_{CA} under each wedge) and is chosen to be different from the angle of the wedge plane. This difference causes the crystal axis plane to decouple from the wedge plane in each wedge. When crystal axis planes are coupled in the direction of

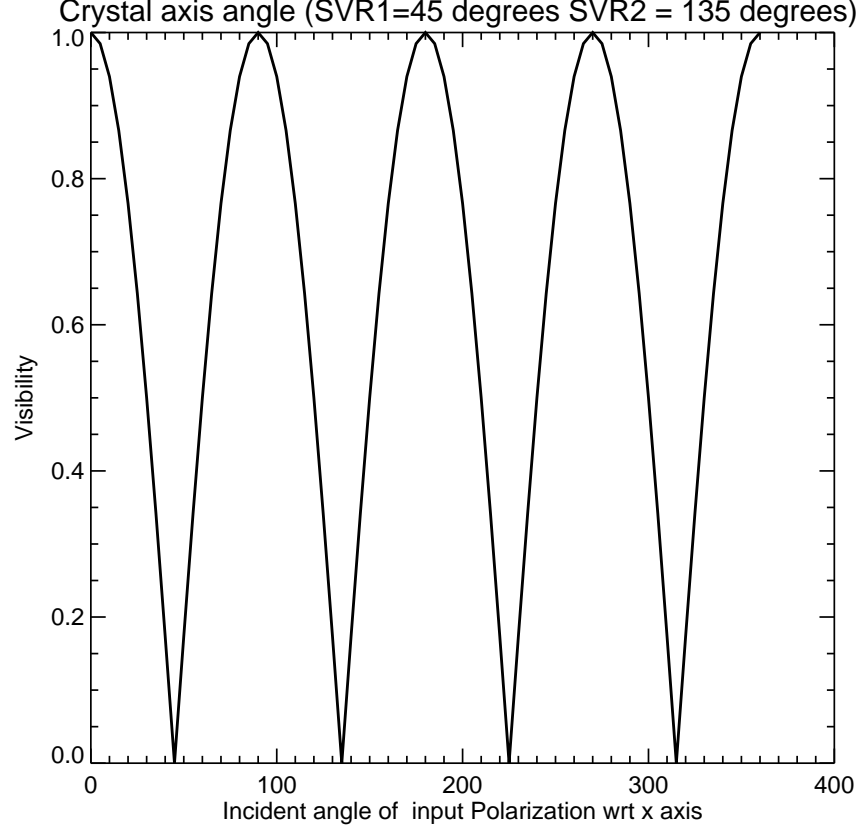


Figure 2.2: Visibility of fringe patterns.

the wedge plane in both SVRs, input light linearly polarized in the direction parallel or perpendicular to the crystal axis in the entrance wedge will not be modulated. The lack of modulation for input polarization orientations - 45, 135, 225, and 315 degrees with respect to x axis, is shown by zero visibilities in Figure 2.2. Hence decoupling the wedge plane from the crystal axis plane ensures that all linear polarizations are modulated into fringe patterns.

When a light ray of arbitrary polarization is incident on the entrance surface of SVR 1, the polarization of the ray can be projected onto axes perpendicular and parallel to the crystal axis. These projections determine the amplitude of the light waves travelling at two speeds. The wedges in the SVRs are made of positive uniaxial

birefringent crystal which implies that in the first wedge of SVR 1, the faster wave experiences an ordinary index (n_o) perpendicular to the crystal axis and the slower wave experiences extraordinary index (n_e) along the crystal axis. The polarization of any light wave incident on the first wedge can be projected onto vectors parallel and perpendicular to the crystal axis with a possible phase difference between them. The paths taken by the light wave with these polarizations are called the ordinary and extraordinary rays, respectively. As is common practice the waves themselves are referred to as extraordinary rays (e-rays) and ordinary ray (o-rays). In the first wedge the e-ray and o-ray see the same physical path length but different optical path lengths due to the different refractive indices as seen by these rays. On reaching the wedge plane, the o-ray sees refractive index n_e , and e-ray sees refractive index n_o from the second wedge. In the second wedge, the o-ray from the first wedge travels as the e-ray, and the e-ray travels as o-ray. Hence the rays in SVR 1 are named oe secondary ray and eo secondary ray respectively.

Due to the oblique incidence at the wedge plane, the oe and eo secondary rays get refracted in different directions according to Snell's law:

$$n_e * \sin \theta_1 = n_o * \sin \theta_{eo}, n_o * \sin \theta_1 = n_e * \sin \theta_{oe}$$

where θ_1 is the incident angle of the e-ray and o-ray at the oblique plane, θ_{eo} and θ_{oe} represent new directions of the eo and oe secondary rays in the second wedge of SVR 1. This change in direction makes the eo and oe secondary rays see different physical path lengths while traversing the second wedge. Both oe and eo secondary rays acquire an optical path difference (OPD) based on their transverse position of entry at the first wedge. The transverse coordinates on the entrance face of the first wedge for which there is zero optical path difference between eo and oe secondary

rays is called the mechanical center-line axis of the system. Assuming the wedges are identically shaped, the OPD between the oe and eo secondary rays is linearly proportional to the distance between the mechanical center-line axis and point where the ray entered the first wedge as measured along the common wedge plane.

The divergent eo and oe secondary rays exit SVR 1 and are incident on the first wedge of SVR 2. The eo ray gets coupled into the eigen modes of the first wedge of SVR 2, giving rise to rays eoe & eoo and similarly oe ray gives rise to rays oeo & oee. At the wedge plane oeo & eoo rays see a refractive index n_e and oee & eoe rays see n_o respectively. Thus four tertiary eigen rays are created in the second wedge of SVR 2 : ooeo, eoee, oeeo and eoee. Due to the oblique incidence at the wedge plane of SVR 2 these tertiary rays get refracted in different directions and emerge from the back surface of SVR 2 diverging from one another. These tertiary eigen rays, after passing through SVR 2, have undergone a phase retardation whose gradient is orthogonal to the one imposed by SVR 1. A close look at Figure 2.1b reveals that the ooeo and eoee tertiary rays will be linearly polarized at 60 degrees while oeeo and eoee tertiary rays will be polarized at 150 degrees.

Finally, the unique mapping system created by the ISIP is complete when the tertiary eigen rays pass through a linear polarizer that transmits only that component of the electric field that is parallel to its transmission axis. Thus the tertiary eigen rays exiting the linear polarizer are all polarized identically causing their corresponding wave fronts to interfere and produce a unique polarization mapping in the form of an irradiance fringe pattern. The polarization of the input ray has been encoded into a unique irradiance fringe pattern. There are no restrictions on the transmission axis orientation of the linear polarizer.

Since every wave front incident on the ISIP creates four tertiary wave fronts, this device can be analyzed as a four beam common path interferometer. To observe the

fringes from this interferometer, the four beams must be diverging relative to each other and the detector needs be placed conjugate to a plane where the beams are still overlapping. If a telescope is used in front of the ISIP, a finite PSF is created on the entrance face of the ISIP and the detector must be placed so that the four PSFs overlap substantially. If the beams or the PSFs diverge significantly before the detector then there will be no interference.

In this section an attempt has been made to explain the construction and working principle of the ISIP as much as to give a basic framework for the further work. The Figures 2.1a and 2.1b are taken from Van Delden's work [35]. A more detailed description and analysis on the construction and functionality of the device has already been done by Van Delden [35].

2.2 BCA configurations used in other ISIPs

The BCA assembly used by Oka [36] as in Figure 2.3 is similar to Van Delden's configuration [35, 34]. This assembly consists of a two prism pairs and an analyzer forming the BCA while a CCD image sensor records the intensity output. The prism pairs PR1 and PR2 are made out of birefringent crystals and the analyzer is a linear polarizer. The arrows in the prism pairs as in Figure 2.3 indicate the direction of the fast axis of the crystal with respect to the x axis in each prism. In the analyzer the arrow indicates the direction of the transmission axis with respect to the x axis.

The differences in the configurations used by Oka [36] and Van Delden [34] are in the choice of direction of the wedge planes, fast axis orientations in the prisms (wedges), and crystal material. The direction of the wedge planes used by Van Delden coupled into both x and y directions while in Oka's configuration the direction of the wedge plane was either in x or y direction. Such choices of directions for wedges would be easier to fabricate assuming that the dimensions of the BCA is equal in x or y

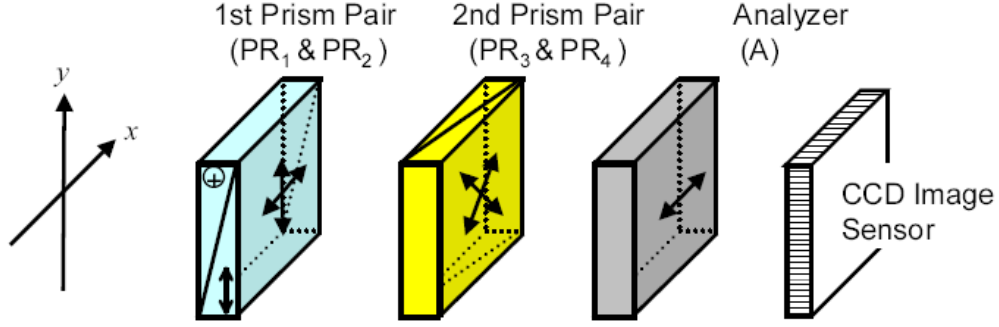


Figure 2.3: BCA configuration used by Oka (taken from [36]).

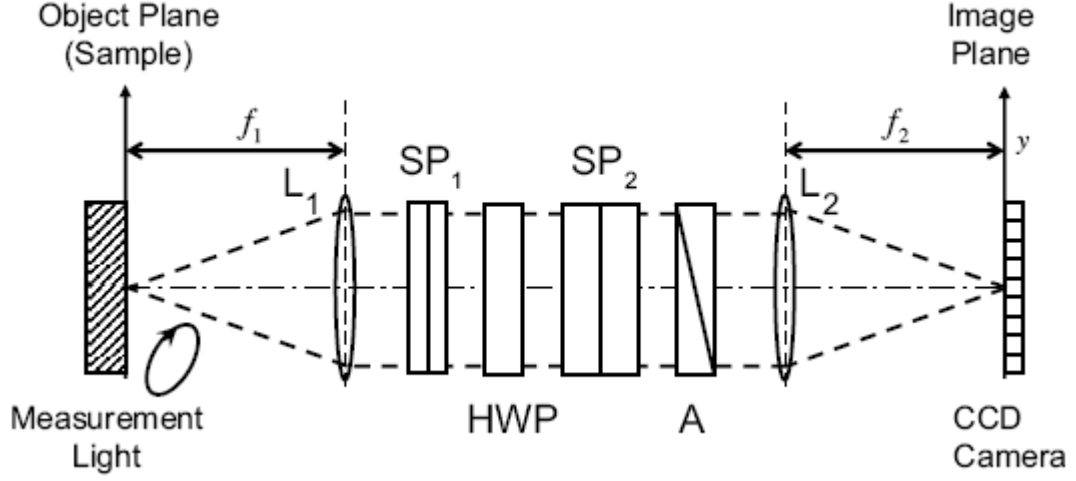


Figure 2.4: BCA using Savart plates (taken from [39]).

direction Oka's configuration is a modification of the spectroscopic polarimeter with a channeled spectrum [44] while Van Delden's configuration is the first of its kind. The fast axis orientations in the crystal wedges (prisms) in Van Delden's configuration were 30, 120, 150 and 60 degrees with respect to the x axis respectively while the prisms in Oka's configuration had 0, 90, 45 and -45 degree fast axis orientations with respect to the x axis. The crystal material used by Van Delden was Yttrium Vanadate while Oka used calcite.

The operating principle of these two configurations is the same - each incident

wave front or ray splits into four tertiary wave fronts or rays and the linear polarizer makes the wave fronts to have the same polarization thereby interfering them to produce an intensity modulated fringe pattern. However, the difference in choice of the wedge plane and fast axis orientations cause the fringe patterns to have different shapes for input beams of identical polarization.

The BCA configurations using birefringent prisms can be difficult to fabricate due to the small wedge angle and physical dimensions involved. Moreover, the beam splitting at the wedge planes causes problems in applications requiring high spatial resolution measurements. To overcome this limitation Oka, et.al [39] constructed a BCA configuration using Savart plates as shown in the Figure 2.4. Several researchers including Dereniak, et.al [38, 8, 39] have used BCA configurations involving Savart plates to reconstruct Stokes images from outdoor and retinal measurements. This assembly consists of two Savart plates of different thickness, a half wave plate and an analyzer (linear polarizer). Each Savart plate is made of two uniaxial crystals and the transmission axis of the analyzer is oriented at 0 degrees with respect to the x axis and the fast axis of the half wave plate is oriented at 22.5 degrees with respect to the x axis. In the assembly shown in Figure 2.4 lens L1 has been used to collimate the light from the measurement sample while the lens L2 images the light exiting the analyzer onto the detector.

A Savart plate splits the input light into ordinary (o) and extraordinary (e) components and provides a lateral shear for the extraordinary component at the output. Therefore, an input beam of light is sheared to two output beams of orthogonal polarizations travelling in the same direction. The amount of shear depends on the thickness of the Savart plate and the direction of shear makes an angle of 45 degrees with respect to the x axis. In the design developed by Oka, et.al [39] the fast axis birefringent crystal slices forming each Savart plate is oriented at ± 45 degrees with

respect to the x axis. The half wave plate with its fast axis oriented at 22.5 degrees with respect to x axis rotates the electric field vector by 45 degrees enabling the second Savart plate to shear the beams exiting the first Savart plate to form four output beams travelling in the same direction. The linear polarizer oriented at 0 degrees with respect to the x axis passes only the horizontal component of the four beams. The imaging lens focuses all four beams exiting the linear polarizer causing them to interfere at the detector plane to form intensity fringes.

The main draw back to both the birefringent and Savarte crystal assemblies is the dispersive nature of the crystal material which results in a loss of fringe visibility as the number of interfering wavelengths increases. Consequently the bandwidth over which light is collected has to be limited and a bandpass filter is used with the BCA and Savart plate crystal assembly configurations. Narrow bandwidth operations of these assemblies can result in low SNR in the measured Stokes parameters. To overcome this problem, Dereniak, et. al [37] have developed a configuration involving a dispersion corrected polarization Sagnac interferometer that can detect Stokes components either S_1 and S_2 or S_2 and S_3 .

\

CHAPTER 3

SIMULATION DESCRIPTION

Simulations in this work require accurate models of some of the components of the ISIP and the capability to include real effects similar to those that occur during practical imaging. A familiar software environment (IDL) is used to achieve these ends. Components of the ISIP that require modeling are the telescope, BCA, and detector while the effects that need inclusion are detector noise, and broad band effects. Detailed descriptions of the models and methods involved along with user inputs are presented in a logical fashion. The developed simulation model is then used to present an example where an object with defined SOP is imaged through the developed telescope and BCA models. The imaged object is presented as a fringe-modulated image with detector noise.

An important assumption of this simulation is that the entire BCA including the detector is assumed to be effectively at the focal plane. Hence, there is no need to model the Fresnel propagation of light between the elements of the BCA. For this assumption to be valid, BCA and the detector must be placed within the depth of focus of the telescope or equivalently, the BCA can be contained in the telescope depth of focus and relay optics can be used to image the interference plane onto a detector. The telescope used with the BCA must produce a beam slow enough to neglect the effects of diffraction.

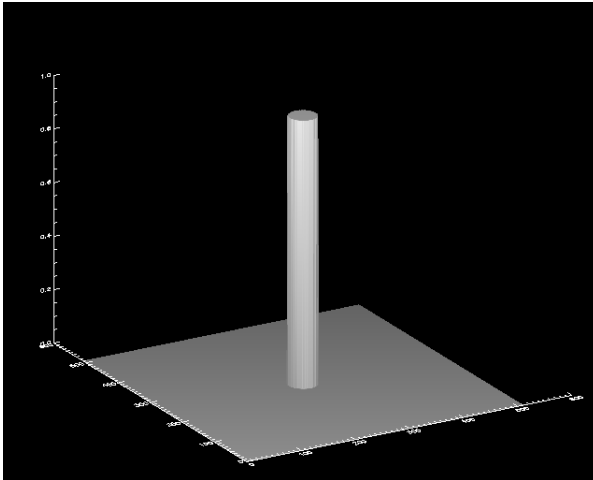
A clear idea of the methodology used in simulating various components and effects are presented in the following sections of this Chapter:

- A telescope model
- BCA models
- Modeling finite bandwidth
- A detector model with noise effects
- IDL implementation
- User inputs
- Simulation example

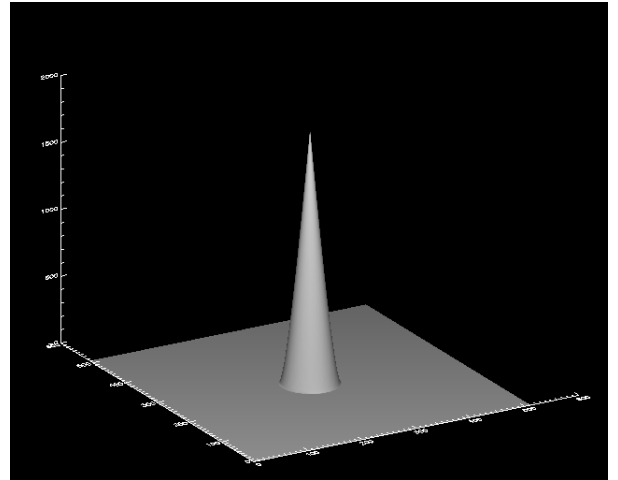
3.1 A telescope model - monochromatic illumination

The fore-optics used in the ISIP is a telescope that images a scene or object onto the BCA. The purpose of modeling the telescope is to generate a PSF that models diffraction and aberrations, if required. A narrow field of view of an ISIP is considered since the sampling requirements would make the fabrication of the wide field instruments expensive. The sampling requirements for the ISIP is discussed later in Chapter 5. For a narrow field of view the field dependent aberrations can be neglected and the imaging system can be treated as an linear shift invariant system also known as an isoplanatic system. The pupil function of the telescope is simple circle with no secondary obscuration.

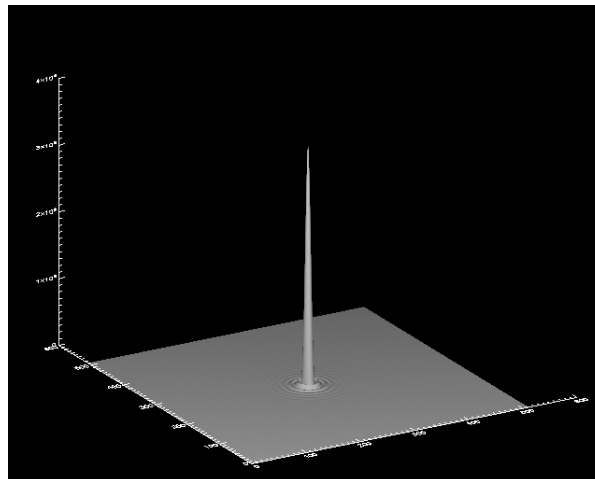
In case of linear shift-invariant incoherent imaging, the incoherent transfer function (P_{incoh}) is the scaled version of the complex auto-correlation of the pupil function and the optical transfer function (OTF) is the normalized version of the complex auto-correlation of the pupil function [40]:



(a) Coherent transfer function.



(b) Incoherent transfer function.



(c) Incoherent PSF.

Figure 3.1: Telescope model.

$$P_{incoh}(\rho) = \frac{A_c}{(\lambda p)^2} [t_{pupil} \star t_{pupil}^*](\lambda p q)$$

$$OTF(\rho) = \frac{P_{incoh}(\rho)}{P_{incoh}(0)} = \frac{[t_{pupil} \star t_{pupil}^*](\lambda p q)}{[t_{pupil} \star t_{pupil}^*](0)}$$

where t_{pupil} is the pupil function, ρ is the frequency domain variable, p is the distance of the object from the pupil [40], λ is the wavelength of the light used, A_c is a constant with units of area, \star represents auto-correlation, $*$ represents complex conjugate, and q is the distance of the image plane from the pupil [40]. The support of the optical transfer function (OTF) is twice as large as the coherent transfer function (P_{coh}) due to the auto-correlation operation. Hence, to create a correct OTF , the pupil function must be embedded in an array of size greater than or equal to twice the size of the pupil function before the auto-correlation can be computed. The incoherent PSF (p_{incoh}) is computed by the inverse Fourier transform of P_{incoh} :

$$p_{incoh}(\vec{r}) = \frac{A_c}{(\lambda p)^4} \left| T_{pupil}\left(-\frac{\vec{r}}{\lambda p}\right) \right|^2.$$

Modified forms of the IDL FFT routines to include checker boarding are used to compute the forward and inverse Fourier transforms. Checker boarding is done to move the zero-frequency component to the center of the array. This provides an easy way of visualizing a Fourier transform with the zero-frequency component in the middle of the spectrum. In case of matrices the quadrants one and three and quadrants two and four are swapped. Figures 3.1a, 3.1b, and 3.1c show a coherent transfer function (20 pixel radius), incoherent transfer function, and incoherent PSF of a telescope model on a 512 X 512 pixel array. These figures represent an oversampled array - the PSF

has been sampled by an array that has more number of pixels than it needs since the circumference of OTF does not touch the edges of the array. This is actually an requirement for the ISIP and reason for this the additional pixel requirement can be explained as follows:

The image formed by the ISIP can be written as

$$im(x, y) = (ob(x, y) * p_{incoh}(x, y)) \times \sum_{n=1}^6 a_n(x, y) C_n(x, y)$$

where $ob(x, y)$ is the intensity distribution of the object, $p_{incoh}(x, y)$ is the incoherent PSF, $n = 1, 2, 3, 4, 5, 6$ represent horizontal, vertical, 45, 135, RHC, and LHC polarizations and $C_n(x, y)$ are the associated calibration fringes.

Taking Fourier transform on both sides :

$$F \{im(x, y)\} = F \{(ob(x, y) * p_{incoh}(x, y))\} * F \left\{ \sum_{n=1}^6 a_n(x, y) C_n(x, y) \right\}$$

$$F \{im(x, y)\} = (\{F(ob(x, y))\} \times OTF) * F \left\{ \sum_{n=1}^6 a_n(x, y) C_n(x, y) \right\} \quad (3.1)$$

The Fourier transform of the calibration fringes have delta functions (approximately) at spatial frequencies that encode the polarization information and at each position of the delta function there will be a scaled copy of $(\{F(ob(x, y))\} \times OTF)$. The spatial frequencies encoding the polarization information must be sufficiently high to avoid aliasing the side lobes into the main lobe. When the OTF is spread till the edges of the array, the energy from the the side lobes is artificially folded into the lower frequencies of the unmodulated image and aliasing occurs as a result. The sampling requirements for the ISIP will be discussed in detail in Chapter 5.

3.2 BCA models

The BCA can be modeled with a matrix using either Jones or Mueller calculus depending on the requirements of the simulation. The Mueller matrix and Jones matrix representing the BCA map the Stokes vectors and Jones vectors of the input light to the corresponding Stokes vector and Jones vector of output light. Stokes vectors represent the polarization of incoherent light by intensity vector elements while the Jones vectors represent polarization of coherent light through electric field vector elements. A Mueller model is useful when the input light is incoherent, partially polarized or a combination of both. However, when the input light is spatially coherent a Mueller model cannot carry phase information associated with the fields as it maps Stokes vectors whose components are scalar values of intensities and hence cannot be used to study the associated interference effects. On the other hand, a Jones model is suitable for studying the effects of complete and partial coherence but cannot be used in simulations where the input light is partially polarized or incoherent. When the light from the scene is partially coherent the overlapping energies from different portions of the object interfere to produce fringes apart from the ones from the same portion of the object. Hence a need for both models arises based on the DOP and coherency of input light.

The development of both Mueller and Jones models are presented in this section and proper use of the models should be made based on effects that need to be observed. The Jones model presented in this section is not a comprehensive one and would require further work to include effects of spatial coherence in imaging objects that have complete or partial spatial coherency. In this work, objects and scenes imaged through the BCA are assumed to be spatially incoherent and the light from it can be partially and arbitrarily polarized. Hence the Mueller model is preferred over

Jones model for the simulation purposes of this work. The choice of Mueller model also presents a convenient framework for reconstruction in the form of a set of linear equations since the detector measurements are directly in intensities. The linear equations and reconstruction procedure based on the Mueller model is presented in Chapter 4.

3.2.1 Mueller Model

The Mueller model provides a direct intensity to intensity mapping and uses the following retarder matrix [41] for modeling the SVRs

$$\mathbf{M}(\phi, 2\theta) = \begin{bmatrix} 1 & 0 & 0 & 0 \\ 0 & \cos^2 2\theta + \cos \phi \sin^2 2\theta & (1 - \cos \phi) \sin 2\theta \cos 2\theta & -\sin \phi \sin 2\theta \\ 0 & (1 - \cos \phi) \sin 2\theta \cos 2\theta & \sin^2 2\theta + \cos \phi \cos^2 2\theta & \sin \phi \cos 2\theta \\ 0 & \sin \phi \sin 2\theta & -\sin \phi \cos 2\theta & \cos \phi \end{bmatrix}$$

Where ϕ is the phase shift offered by the retarder and θ is orientation of fast axis of the retarder with respect to the horizontal axis (x axis) and $\phi = (2\pi/\lambda) * \text{OPD}$. In case of SVRs, the phase shift ϕ is not a constant and depends on value of OPD at the transverse location (x, y). The transverse position dependence of OPD is due to the wedge shape in each retarder that causes retarder thickness to vary as function of the transverse coordinates and orientation of the crystal axis in each wedge forming the SVRs. Therefore both ϕ and OPD are now written as functions of the transverse coordinates i.e. $\phi(x, y)$ and $\text{OPD}(x, y)$. The 2θ dependence of \mathbf{M} indicates that the spatially varying retarder is the same when rotated by angles that are integer multiples of 180 degrees and this idea is generally true for Mueller matrices representing optical elements. The Mueller matrix for the ISIP or crystal assembly is written as product

of the individual Mueller matrices of the SVRs and linear polarizer

$$\mathbf{M}_{ISIP}(x, y) = \mathbf{M}_{LP}(2\theta_{TA}) \mathbf{M}_{SVR2}(\phi_2(x, y), 2\theta_2) \mathbf{M}_{SVR1}(\phi_1(x, y), 2\theta_1) \quad (3.2)$$

$$\mathbf{M}_{LP}(2\theta_{TA}) = (1/2) * \begin{bmatrix} 1 & \cos 2\theta_{TA} & \sin 2\theta_{TA} & 0 \\ \cos 2\theta_{TA} & \cos^2 2\theta_{TA} & \sin 2\theta_{TA} \cos 2\theta_{TA} & 0 \\ \sin 2\theta_{TA} & \sin 2\theta_{TA} \cos 2\theta_{TA} & \sin^2 2\theta_{TA} & 0 \\ 0 & 0 & 0 & 0 \end{bmatrix} \quad (3.3)$$

Where θ_{TA} is the orientation of transmission axis of linear polarizer with respect to horizontal axis (x axis).

$$\mathbf{M}_{SVR1}(\phi_1, 2\theta_1) =$$

$$\begin{bmatrix} 1 & 0 & 0 & 0 \\ 0 & \cos^2 2\theta_1 + \cos \phi_1 \sin^2 2\theta_1 & (1 - \cos \phi_1) \sin 2\theta_1 \cos 2\theta_1 & -\sin \phi_1 \sin 2\theta_1 \\ 0 & (1 - \cos \phi_1) \sin 2\theta_1 \cos 2\theta_1 & \sin^2 2\theta_1 + \cos \phi_1 \cos^2 2\theta_1 & \sin \phi_1 \cos 2\theta_1 \\ 0 & \sin \phi_1 \sin 2\theta_1 & -\sin \phi_1 \cos 2\theta_1 & \cos \phi_1 \end{bmatrix} \quad (3.4)$$

θ_1 is the orientation of fast axis of SVR 1 with respect to horizontal axis (x axis) and ϕ_1 is the phase difference offered by SVR 1 and is dependent on transverse coordinates (x, y):

$$\phi_1(x, y) = (2\pi/\lambda) \text{OPD1}(x, y)$$

The transverse coordinate dependence of ϕ_1 and ϕ_2 is not explicitly shown in Equations 3.4 and 3.5 due to space constraints.

$$\mathbf{M}_{SVR2}(\phi_2, 2\theta_2) = \begin{bmatrix} 1 & 0 & 0 & 0 \\ 0 & \cos^2 2\theta_2 + \cos \phi_2 \sin^2 2\theta_2 & (1 - \cos \phi_2) \sin 2\theta_2 \cos 2\theta_2 & -\sin \phi_2 \sin 2\theta_2 \\ 0 & (1 - \cos \phi_2) \sin 2\theta_2 \cos 2\theta_2 & \sin^2 2\theta_2 + \cos \phi_2 \cos^2 2\theta_2 & \sin \phi_2 \cos 2\theta_2 \\ 0 & \sin \phi_2 \sin 2\theta_2 & -\sin \phi_2 \cos 2\theta_2 & \cos \phi_2 \end{bmatrix} \quad (3.5)$$

θ_2 is the orientation of fast axis of SVR 2 with respect to horizontal axis (x axis) and ϕ_2 is the phase difference offered by SVR 2 and is transverse position dependent $\phi_2(x, y)$

$$\phi_2(x, y) = (2\pi/\lambda) \text{OPD2}(x, y)$$

Inserting Equations 3.5 , 3.4 , and 3.3 in Equation 3.2 and using $\theta_{TA} = 0$ degrees , we obtain

$$\mathbf{M}_{ISIP}(x, y) = (1/2) \begin{bmatrix} F_0(x, y) & F_1(x, y) & F_2(x, y) & F_3(x, y) \\ F_4(x, y) & F_5(x, y) & F_6(x, y) & F_7(x, y) \\ F_8(x, y) & F_9(x, y) & F_{10}(x, y) & F_{11}(x, y) \\ F_{12}(x, y) & F_{13}(x, y) & F_{14}(x, y) & F_{15}(x, y) \end{bmatrix} \quad (3.6)$$

where

$$F_0(x, y) = 1 \quad (3.7)$$

$$\begin{aligned} F_1(x, y) = & (\cos^2 2\theta_1 + \cos \phi_1(x, y) \sin^2 2\theta_1)(\cos^2 2\theta_2 + \cos \phi_2(x, y) \sin^2 2\theta_2) \\ & + ((1 - \cos \phi_2(x, y)) \sin 2\theta_2 \cos 2\theta_2)((1 - \cos \phi_1(x, y)) \sin 2\theta_1 \cos 2\theta_1)) \\ & - (\sin \phi_2(x, y) \sin 2\theta_2)(\sin \phi_1(x, y) \sin 2\theta_1) \quad (3.8) \end{aligned}$$

$$\begin{aligned} F_2(x, y) = & (\cos^2 2\theta_2 + \cos \phi_2(x, y) \sin^2 2\theta_2)((1 - \cos \phi_1(x, y)) \sin 2\theta_1 \cos 2\theta_1)) \\ & + ((1 - \cos \phi_2(x, y)) \sin 2\theta_2 \cos 2\theta_2)(\sin^2 2\theta_1 + \cos \phi_1(x, y) \cos^2 2\theta_1) \\ & + (\sin 2\theta_1 \cos 2\theta_1)(\sin \phi_2(x, y) \sin 2\theta_2) \quad (3.9) \end{aligned}$$

$$\begin{aligned} F_3(x, y) = & -(\cos^2 2\theta_2 + \cos \phi_2(x, y) \sin^2 2\theta_2)(\sin \phi_1(x, y) \sin 2\theta_1) \\ & + ((1 - \cos \phi_2(x, y)) \sin 2\theta_2 \cos 2\theta_2)(\sin 2\theta_1 \cos 2\theta_1) \\ & - (\sin \phi_2(x, y) \sin 2\theta_2)(\cos \phi_1(x, y)) \quad (3.10) \end{aligned}$$

$$F_4(x, y) = F_0(x, y), \quad (3.11)$$

$$F_5(x, y) = F_1(x, y), \quad (3.12)$$

$$F_6(x, y) = F_2(x, y), \quad (3.13)$$

$$F_7(x, y) = F_3(x, y). \quad (3.14)$$

and

$$F_8(x, y) = F_9(x, y) = 0$$

$$F_{10}(x, y) = F_{11}(x, y) = 0$$

$$F_{12}(x, y) = F_{13}(x, y) = 0$$

$$F_{14}(x, y) = F_{15}(x, y) = 0 \quad (3.15)$$

It can be seen from Equations 3.11, 3.12, 3.13, 3.14, and 3.15 that the horizontal orientation of linear polarizer transmission axis with respect to the x axis in the BCA makes the first two rows in the $\mathbf{M}_{ISIP}(x, y)$ matrix the same and rest of the rows zeros. Similarly, a 45 degree orientation of the linear polarizer with respect to the x axis would make the first and third rows the same and rest of the rows zeros. But a linear polarizer oriented at 22.5 with respect to the x axis would make only the fourth row zero. The rest of rows will not be zeros. However, the last row will always remain zero irrespective of the transmission axis orientation with respect to the x axis since the light exiting the BCA is always linearly polarized.

A linear polarizer transmission axis orientation of θ degrees with respect to the

x axis does not imply that the BCA is opaque to incident light polarized at $\theta + 90$ degrees (with respect to x axis) since the light rays exiting the second SVR 2 will always be polarized either along the direction of the crystal axis of the second wedge in SVR 2 or in a direction orthogonal to it. Though the polarization of the incident light does not determine the exiting polarization orientation of light rays from SVR 2, it does determine the electric field amplitude and associated intensity of each exiting light ray.

The polarization of the input light and light exiting the crystal assembly are modeled by Stokes vectors $\vec{\mathbf{S}}_{in}$ and $\vec{\mathbf{S}}_{out}$ respectively. If the SOP is changing across the input beam of light then the Stokes vectors $\vec{\mathbf{S}}_{in}$ and $\vec{\mathbf{S}}_{out}$ have to include spatial dependence in their representations, i.e $\vec{\mathbf{S}}_{in}(x, y)$ and $\vec{\mathbf{S}}_{out}(x, y)$ The input $\vec{\mathbf{S}}_{in}(x, y)$ is mapped to $\vec{\mathbf{S}}_{out}(x, y)$ by the relation

$$\vec{\mathbf{S}}_{out}(x, y) = \mathbf{M}_{ISIP}(x, y) \vec{\mathbf{S}}_{in}(x, y) \quad (3.16)$$

where

$$\vec{\mathbf{S}}_{in}(x, y) = \begin{pmatrix} S_0(x, y) \\ S_1(x, y) \\ S_2(x, y) \\ S_3(x, y) \end{pmatrix}, \vec{\mathbf{S}}_{out}(x, y) = \begin{pmatrix} S'_0(x, y) \\ S'_1(x, y) \\ S'_2(x, y) \\ S'_3(x, y) \end{pmatrix} \quad (3.17)$$

and $M_{ISIP}(x, y)$ is given by Equation 3.2. When the matrix multiplication in Equation 3.16 is performed, the analytical form of the output light intensity $\mathbf{O}(x, y)$ or $S'_0(x, y)$ which is first element of the vector $\vec{\mathbf{S}}_{out}(x, y)$ in Equation 3.17 is obtained as :

$$\begin{aligned} \mathbf{O}(x, y) = S'_0(x, y) = (1/2)[S_0(x, y) F_0(x, y) + S_1(x, y) F_1(x, y) \\ + S_2(x, y) F_2(x, y) + S_3(x, y) F_3(x, y)] \end{aligned} \quad (3.18)$$

This is also the expression for the intensity of the light as seen by the detector.

3.2.2 Jones Model

The Jones model provides a mapping from the input electric field to the output electric field and uses the following retarder matrix when the fast-axis of the retarder is at θ degrees with respect to the horizontal axis:

$$\mathbf{J}_{Ret}(\theta) = \mathbf{J}_{Rot}(-\theta) \mathbf{J}_{Ret}(0) \mathbf{J}_{Rot}(\theta) \quad (3.19)$$

Where $\mathbf{J}_{Ret}(0)$, $\mathbf{J}_{Ret}(\theta)$ are the Jones matrices of the retarders when the fast-axis of the retarder is at 0 and θ degrees with respect to the horizontal axis, $\mathbf{J}_{Rot}(\theta)$ is the Jones matrix of a rotator and

$$\mathbf{J}_{Rot}(\theta) = \begin{pmatrix} \cos \theta & \sin \theta \\ -\sin \theta & \cos \theta \end{pmatrix}, \quad \mathbf{J}_{Ret}(0) = \begin{pmatrix} e^{i\phi} & 0 \\ 0 & 1 \end{pmatrix} \quad (3.20)$$

where ϕ is the phase difference offered by the retarder. Evaluating Equation 3.19, the general form of a retarder at θ degrees with respect to horizontal axis is obtained as:

$$\mathbf{J}_{Ret}(\theta) = \begin{pmatrix} e^{i\phi} \cos^2 \theta + \sin^2 \theta & e^{i\phi} \cos \theta \sin \theta + \sin \theta \cos \theta \\ e^{i\phi} \cos \theta \sin \theta + \sin \theta \cos \theta & e^{i\phi} \sin^2 \theta + \cos^2 \theta \end{pmatrix} \quad (3.21)$$

The Jones matrix for the ISIP can be written as the product of the individual Jones matrices of the SVRs and linear Polarizer:

$$\mathbf{J}_{ISIP}(x, y) = \mathbf{J}_{LP}(\theta_{TA}) \mathbf{J}_{SVR1}(\phi_2(x, y), \theta_2) \mathbf{J}_{SVR1}(\phi_1(x, y), \theta_1) \quad (3.22)$$

where

$$\mathbf{J}_{SVR1}(\phi_1(x, y), \theta_1) = \quad (3.23)$$

$$\begin{pmatrix} e^{i\phi_1(x,y)} \cos^2 \theta_1 + \sin^2 \theta_1 & e^{i\phi_1(x,y)} \cos \theta_1 \sin \theta_1 + \sin \theta_1 \cos \theta_1 \\ e^{i\phi_1(x,y)} \cos \theta_1 \sin \theta_1 + \sin \theta_1 \cos \theta_1 & e^{i\phi_1(x,y)} \sin^2 \theta_1 + \cos^2 \theta_1 \end{pmatrix} \quad (3.24)$$

$$\mathbf{J}_{SVR2}(\phi_2(x, y), \theta_2) = \quad (3.25)$$

$$\begin{pmatrix} e^{i\phi_2(x,y)} \cos^2 \theta_2 + \sin^2 \theta_2 & e^{i\phi_2(x,y)} \cos \theta_2 \sin \theta_2 + \sin \theta_2 \cos \theta_2 \\ e^{i\phi_2(x,y)} \cos \theta_2 \sin \theta_2 + \sin \theta_2 \cos \theta_2 & e^{i\phi_2(x,y)} \sin^2 \theta_2 + \cos^2 \theta_2 \end{pmatrix} \quad (3.26)$$

$$\mathbf{J}_{LP}(\theta_{TA}) = \begin{pmatrix} \cos^2 \theta & \sin \theta \cos \theta \\ \sin \theta \cos \theta & \sin^2 \theta \end{pmatrix} \quad (3.27)$$

Evaluating Equation 3.22 using Equations 3.24, 3.26, and 3.27 with $\theta_{TA} = 0$ we obtain

$$\mathbf{J}_{ISIP}(x, y) = \begin{pmatrix} J_1 & J_2 \\ J_3 & J_4 \end{pmatrix} \quad (3.28)$$

where

$$\begin{aligned} \mathbf{J}_1 = & (e^{i\phi_1(x,y)} \cos^2 \theta_1 + \sin^2 \theta_1)(e^{i\phi_2(x,y)} \cos^2 \theta_2 + \sin^2 \theta_2) \\ & + (e^{i\phi_2(x,y)} \cos \theta_2 \sin \theta_2 - \sin \theta_2 \cos \theta_2)(e^{i\phi_1(x,y)} \cos \theta_1 \sin \theta_1 - \sin \theta_1 \cos \theta_1) \end{aligned} \quad (3.29)$$

$$\begin{aligned} \mathbf{J}_2 = & (e^{i\phi_2(x,y)} \cos^2 \theta_2 + \sin^2 \theta_2)(e^{i\phi_1(x,y)} \cos \theta_1 \sin \theta_1 - \sin \theta_1 \cos \theta_1) \\ & + (e^{i\phi_2(x,y)} \cos \theta_2 \sin \theta_2 - \sin \theta_2 \cos \theta_2)(e^{i\phi_2(x,y)} \cos^2 \theta_2 + \sin^2 \theta_2) \end{aligned} \quad (3.30)$$

$$\mathbf{J}_3 = 0 \quad (3.31)$$

$$\mathbf{J}_4 = 0 \quad (3.32)$$

The incident field is represented by $\vec{\mathbf{E}}_{in} = \begin{pmatrix} E_x \\ E_y \end{pmatrix}$. When the SOP varies across the incident beam, $\vec{\mathbf{E}}_{in}$ becomes space dependent i.e $\vec{\mathbf{E}}_{in}(x, y) = \begin{pmatrix} E_x(x, y) \\ E_y(x, y) \end{pmatrix}$ and corresponding output field is given by $\vec{\mathbf{E}}_{out}(x, y) = \begin{pmatrix} E'_x(x, y) \\ E'_y(x, y) \end{pmatrix}$. The mapping from $\vec{\mathbf{E}}_{in}(x, y)$ to $\vec{\mathbf{E}}_{out}(x, y)$ is given by the relation:

$$\begin{pmatrix} E'_x(x, y) \\ E'_y(x, y) \end{pmatrix} = \mathbf{J}_{ISIP}(x, y) \begin{pmatrix} E_x(x, y) \\ E_y(x, y) \end{pmatrix} \quad (3.33)$$

and output intensity as seen by the detector is given by:

$$\mathbf{O}(x, y) = \left| E'_x(x, y) \right|^2 + \left| E'_y(x, y) \right|^2. \quad (3.34)$$

The Mueller matrix modeling followed in section 3.2.1 is based on Van Delden's work [35]. However, the retarder model used in this work are adopted from [41], while the model followed by Van Delden is taken from [42].

3.2.3 Comparison of Mueller and Jones BCA models

To validate the BCA models, outputs from both Mueller and Jones calculus are compared. For this purpose, fringe patterns from individual models for input beams with uniform intensity and fixed polarization are created. These beams are assumed to be collimated and illuminate the entire entrance face of the BCA. Three uniform beams are used for illumination (one at a time) and the polarization of these beams are fixed to be horizontal, 45 and Right Hand Circular (RHC) respectively. The reason for the choice of polarization and number of beams will be evident from the discussion of the reconstruction algorithm in Chapter 4

Fringe patterns created with collimated beams of uniform intensity and polarization (horizontal, 45, and RHC) are the calibration fringes. These patterns can be viewed as basis fringes or eigen fringes where a fringe pattern produced by the BCA for an arbitrary input polarization state can be expressed as a linear combination of the calibration fringes. The depth of modulation (visibility) of the fringe patterns including the calibration fringes produced by the BCA depend on DOP of input light with the maximum depth (visibility = 1) and minimum depth (visibility = 0) occurring for input light with DOP = 1 and DOP = 0 respectively. To create the calibration fringes from both Jones and Mueller models, input light beams of DOP = 1 are used. Figure 3.2 shows calibration fringes from the Mueller (left column)

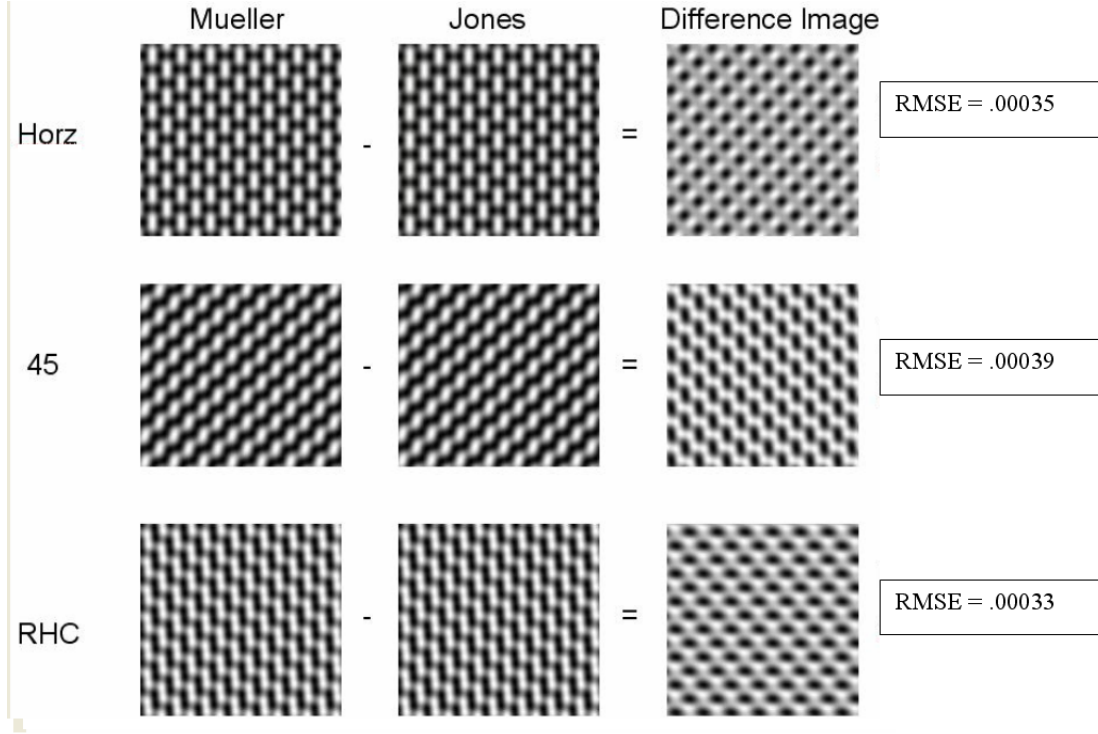


Figure 3.2: Calibration fringes and difference images.

and Jones (center column) models of the BCA generated using the dispersion relation of Yttrium Vanadate (uniaxial crystal material in the BCA), their corresponding difference images (right column), and root mean square error values (RMSE). The maximum fringe intensity value in both Mueller and Jones calibration images is unity and the minimum value is zero. The small magnitude of RMSE values of the difference images indicate that the calibration fringes are identical and hence both models are similar.

3.3 Modeling finite spectral bandwidth

In most practical applications the objects and scenes imaged by ISIP emit light in a wide range of wavelengths. A near monochromatic operation of the ISIP is almost impossible even with a narrow bandpass filter as it causes a significant decrease in the system throughput and poses a challenge when imaging objects of low illumination

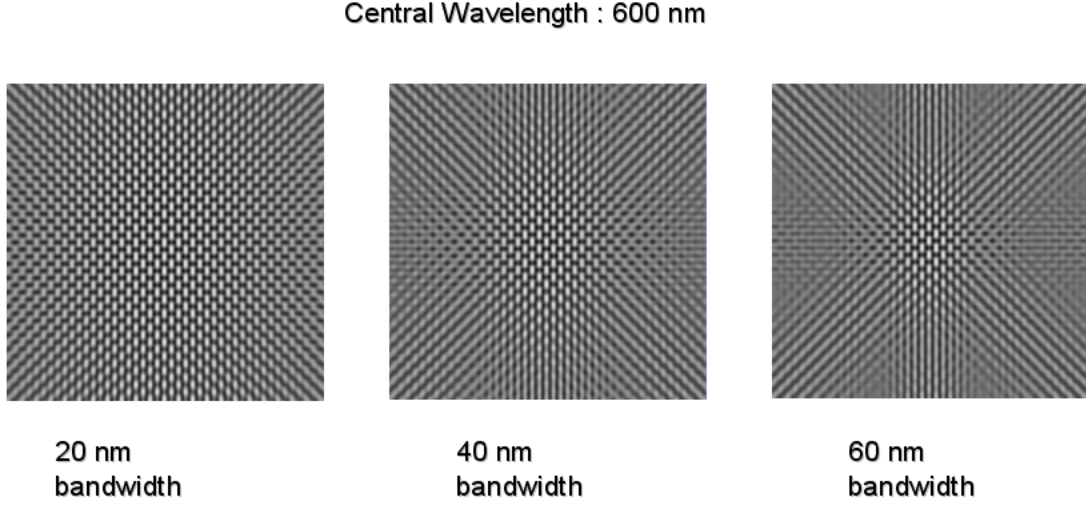


Figure 3.3: Broad band imaging effects on the horizontal calibration fringes.

levels. The two effects that have to be taken into account during broad band imaging are the fore-optics effect and dispersion effect of the uniaxial crystal wedges used in the BCA. The angular resolution of the telescope is given by:

$$\theta_r = 1.22 (\lambda/D)$$

where λ is the wavelength of the light and D is the diameter of the telescope pupil. The rate of change of angular resolution with wavelength and pupil diameter changes are given by

$$d\theta_r/d\lambda = 1.22/D$$

and

$$d\theta_r/dD = (-1.22\lambda)/D^2$$

.Using the condition that the rate of change in angular resolution $d\theta_r$ with respect

to wavelength and diameter should be the same, a relation between the change in pupil diameter, change in wavelength, initial wavelength, and initial pupil diameter is obtained as:

$$dD = -D_0 (d\lambda/\lambda_0)$$

where D_0 , λ_0 are the initial pupil diameter and wavelength. λ_0 is the central wavelength when a bandpass filter is used and D_0 is the user defined pupil diameter corresponding to λ_0 . Therefore a PSF due to broad band imaging can be modeled as a summation of individual PSFs obtained with scaled pupil diameters. The number of summations over a wavelength range in the simulation is a user input and reasonable increments in wavelength gives accurate results with less computational time compared cases with small increments in wavelength. For example, PSF computations for every 5nm increment is reasonable in imaging applications over a wavelength range of 400nm - 700 nm.

The wedges forming SVRs of the BCA are made from the same uniaxial crystal and hence have the same dispersion relation which formulates the variation of the refractive indices - both ordinary and extraordinary, as a function of wavelength of incident light. This variation causes multiple fringe patterns (one for each wavelength) with varying periods to interfere at the image plane causing a washout in fringe visibility at the outer edges of the fringe-modulated image. The washout effect gets increasingly pronounced and begins to affect the inner regions of the image as the number of interfering fringe patterns with different periods (due to difference in wavelengths) increases. Figure 3.3 shows the effects of broad band imaging on the horizontal calibration fringes with Yttrium Vanadate crystal wedges for the BCA and a central wavelength of 600 nm for the bandpass filter.

3.4 A detector model with noise effects

The images of objects and scenes from the ISIP or calibration fringe images from the BCA are detected and digitized by a CCD detector. During the process of detection and digitization of an analog image, a detector and the electronic circuitry associated with it introduces noise that is a combination of both signal dependent noise and signal independent noise. An example of signal dependent noise is the shot noise while dark noise is an example of signal independent noise. The noise from the detector and its electronic circuitry can be divided into three main categories [61]:

Photon noise and shot noise: These terms are frequently used interchangeably when the sources of noise in detectors are discussed. Photon noise usually refers to the random arrival of discrete photons while shot noise is the noise associated with the random generation of electrons in the photo-detector material. The quantum nature of the light reaching the detector is not considered in most cases and hence the photon noise may be safely neglected by assuming a constant flux incident on the detector. However, the photo-electrons produced due to the discrete light-matter interaction results in shot noise which is modeled by a Poisson distribution that obeys the discrete probability law:

$$P_n = e^{-a} * a^n / n!$$

where a is the mean and variance of the distribution and P_n is the probability of receiving n photon-electrons over a time interval T .

Dark noise: This signal independent noise occurs due to the random variation in thermal generated electrons (dark current) by the silicon material of the CCD detector and depends on the temperature of the device. There are two types of noise associated with the dark current - dark current shot noise and dark current

non-uniformity noise. The shot noise component follows Poisson statistics similar to the shot noise created by the photo-electrons. Dark current non-uniformity is the variation of the dark current from pixel to pixel in the detector due to differences in dark signal generation rates. This non-uniformity is either not random or varies very slowly relative to other random effects. The bias due to thermal current buildup can be removed by subtracting an appropriate dark current averaged frame acquired under identical conditions of temperature and integration time as the image with the shutter of the camera closed. However, the noise fluctuations due to dark current cannot be removed from the image.

Read noise: The process of reading out the accumulated charge, conversion into a voltage for quantification (analog to digital (A/D) conversion), and subsequent processing adds noise at every stage but the entire system noise is combined into one term - read noise. The major source of read noise in a CCD is due to the random amount of charge left behind at each pixel during the charge transfer of the read out process. Other major sources of read noise include reset noise, Johnson or white noise and flicker noise.

Reset noise occurs when the charge accumulated by the detector is converted to a voltage by means of a sense capacitor and a source-follower amplifier. The uncertainty of reference voltage set at the sense capacitor due to thermal variations in the channel resistance of the reset transistor (usually a metal-oxide semiconductor field effect transistor (MOSFET)) generates noise. Hence the reference level of the sense capacitor is different for each pixel and the reset noise can be modeled as:

$$N_{reset} = \sqrt{4 * k * T * B * R}$$

where N_{reset} is the noise voltage on the sense node, k is Boltzmann's constant

(joules/kelvin), T is temperature (kelvin), B refers to noise power bandwidth (hertz), and R is the effective channel resistance (ohms).

Johnson noise occurs due to the thermal noise generated by the resistance of the output amplifier MOSFET and is governed by the Johnson white noise equation. This noise is independent of frequency and when the effective resistance is the output impedance of the source-follower amplifier, the following equation models the white noise:

$$N_{white} = \sqrt{4 * k * T * B * R_{out}}$$

where N_{reset} is the noise voltage on the sense node, R_{out} is the output impedance of the amplifier (ohms), k is Boltzmann's constant (joules/kelvin), T is temperature (kelvin), and B refers to noise power bandwidth (hertz).

Flicker noise is commonly referred to as $(\frac{1}{f})$ noise because of its inverse dependence on frequency and the pixel read-out rate of the CCD determines the significant frequency variable. This noise is generally accepted as occurring due to the interface states in the image sensor silicon which turns on and off randomly according to different time constants and the noise magnitude decreases with an increase in frequency. Beyond a certain frequency known as the $(\frac{1}{f})$ corner frequency this noise levels off and a white noise floor is reached. The power spectrum of flicker noise has been empirically modeled as:

$$S_{\Delta V}(\nu) = \frac{\alpha_H * \bar{V}^2}{\bar{N} * |\nu|}$$

where \bar{V} is the mean voltage, \bar{N} is the mean number of free carriers α_H is called Hooge constant and ν is the frequency variable.

Other noise sources that can be included under the read noise category

are generation-recombination noise, electronic interference and clock-jitter noise. Generation-recombination (GR) noise is a thermal effect where the conductivity of a semi-conductor varies due to changes in carrier density concentrations and can be viewed as fluctuations in resistance of the specimen. When an electric field is applied the resistance fluctuations lead to conductivity fluctuations which is the source of this noise and must be considered. The power spectral density of the GR current fluctuations is written as:

$$S_{\Delta i}(\nu) = \frac{V_o^2}{\bar{N} * \bar{R}} * \frac{(2 * \tau)}{(1 + (2 * \pi * \nu * \tau)^2)}$$

where V_0 is the applied voltage, \bar{N} is the mean density of free electrons, \bar{R} is the mean resistance, and τ is the lifetime of the electron in the free state. The CCD detector has electronic circuitry including the CCD preamplifier, CDS signal processor, and ADC which operate at a micro-volt level and are highly sensitive to electronic interference. Additional electronics include digital electronics for camera operations and a switching power supply for providing internal voltages for other necessary operations. The switching operations produce electronic noise which can interfere with low-level CCD signals either through radiation or conduction introducing significant noise in images. This noise is uncorrelated in the frequency domain and is the main source of structured noise in the CCD bias frame. GR noise can be minimized by careful circuit board layout and isolation, shielding and grounding, signal rise-time control, filtering, and carefully considered timing.

The processing and transfer of the accumulated charge to the output of the CCD requires a number of clocking circuits, which is controlled by a master clock. Clocking noise or clock-jitter noise can result from operation of these circuits if the clock signal is fed through to the output waveform. This noise increases with signal and follows

a square-root relation to clocking frequency.

Apart from these sources of noise an additional effect that needs consideration is the Photo Response Non-Uniformity (PRNU) of the pixels in the detector. This can be viewed as a variation in the sensitivity or quantum efficiency of the pixels to convert light into electrons. Hence an image of a uniformly illuminated flat-field will reflect a faint checker board pattern at the individual pixel level. An image processing technique of flat-fielding can be utilized to remove the pattern caused due to pixel quantum efficiency variation. This technique involves the subtraction of a separately acquired flat-field image from the image frames and is used depending on application as it can increase shot noise by a factor of 1.414.

The detector model used in this work assumes the following:

1. The pixels of the detector have the same sensitivity and quantum efficiency.
2. The pixel read-out occurs at high frequency. Hence the effect of $\frac{1}{f}$ noise is negligible.
3. The flux of light incident on the detector is constant over the integration time and hence the photon noise may be neglected.
4. The charge stored in each pixel is read through the same circuitry hence the amplifier bias effects are the same for each individual pixel.
5. The additive noise at the pixels are uncorrelated, independent, and identically distributed while the shot noise mean varies from pixel to pixel.
6. The detector is linear in the wavelength region of operation and all higher order effects are neglected.

For the purpose of this work, noise sources discussed until now may be considered in one of two categories - shot noise and read noise. At every pixel in the detector shot noise from the photo-electrons created from the light-matter interactions is modeled through a Poisson distributed random variable when the number of Photon Detection Events (PDE) collected is less than a certain threshold value. The mean and variance of the Poisson distributed random variable is the number of PDE value at each pixel. In IDL the Poisson distributed random variable can be created with the `randomn` function (with keyword `Poisson` set and equal to the number of PDE). When the energy at a pixel exceeds a certain threshold intensity value, the noise can be modeled through a normally distributed random variable with mean and standard deviation equal to the number of PDE and its square root respectively. In IDL this is achieved by scaling the `randomn` function (with a `/normal` keyword) by the standard deviation and adding the mean value (number of PDE) to the scaled function. A threshold value of 20 PDE per pixel is used to separate the Poisson and Normal distribution. All noise effects apart from the photo-electron shot noise can be combined as read noise and is modeled as an additive normally distributed random variable with a specified mean and variance. In IDL this noise is modeled by scaling the `randomn` function (`/normal` keyword set) with user specified standard deviation and adding a user specified mean to it.

3.5 User inputs

The simulation used in this work is intended to provide the user with the capability to image an object or scene of user-defined resolution and SOP onto a noisy detector of specified dimensions through telescopes and BCAs of varying pupil sizes

and configurations respectively. The user is able to include a band-pass filter in the imaging assembly by specifying a wavelength range over which light is collected by the telescope, model brightness of the object to be imaged, and background intensity by specifying the number of Photon Detection Events from each source at the detector per exposure time of the camera.

The user inputs for this simulation that model the telescope, BCA, object, and detector are as follows:

1. **Telescope diameter, focal length, Field Of View (FOV):** The diameter of the telescope pupil used in the simulation is modeled as a circle of user-defined telescope diameter. This circle is also the the coherent transfer function (P_{coh}) of the telescope used. If a bandpass filter is used, this diameter is defined with respect to the central wavelength of operation. Both field of view of the telescope and its focal length determine the transverse dimensions of the BCA and detector which are the same for the purposes of this work. The magnitude of the FOV must be small enough to neglect the field dependent aberrations and choice of focal length should reflect a slow system so as to neglect diffraction effects.
2. **Wavelength:** This input specifies a wavelength or band of wavelengths over which light is collected. The energy of light collected at each specified wavelength remains the same for the bulk of this work.
3. **Crystal refractive indices and Crystal axis orientation:** The ordinary and extraordinary refractive indices in each wedge of the uniaxial crystal wedges used in the BCA is computed from the dispersion relation provided by the user. The orientation of the crystal axis with respect to the x axis in each wedge (also

provided by the user) along with the dispersion relation and wedge angle, are used to compute the magnitude and direction of the OPD offered by each SVR.

4. **Crystal wedge angle and SVR thickness:** The crystal wedge angle determines the magnitude of the deviation angles of the interfering wave fronts at the output of the BCA. Increasing the wedge angle causes faster deviation of wave fronts resulting in interference fringes of higher frequency and increased dispersion effects at relatively narrow bandwidths. The magnitude of the thickness of each SVR along with the refractive indices and wedge angle determine the optical path length seen by the eigen rays and hence the OPD between them.
5. **Object definition and SOP distribution:** This user input defines the resolution of the input object or scene, and SOP distribution across it. The number of pixels used to represent the input and its SOP is required to be greater than the number of pixels used to represent detector array.
6. **Number of pixels to represent detector array:** Once the detector dimension has been fixed by choice of FOV and focal length for the telescope, the changes in number of pixels in the detector changes the size of individual pixel sampling the image since the detector is assumed to be an array of pixels of identical size and shape.
7. **Number of Photon Detection Events (PDE) from background, foreground and source:** With these inputs the user can control the amount of energy (polarized and unpolarized) collected from the source as well as the energy from the background and foreground of the source combined into one term, to model the effects of imaging objects of varying intensities.
8. **RMS read noise in electrons:** The strength of read noise (models all noise ef-

fects apart from shot noise) can be modeled by an additive normally distributed random variable of user specified mean and standard deviation.

3.6 IDL implementation

The IDL implementation of the simulation procedure is based on Equations 3.18 and 3.34. These equations have spatial-dependence and for evaluation purposes would require a definition of a grid along the direction transverse to the propagation direction. The discrete points of the grid are defined as the transverse coordinates on the entrance face of the BCA. The distance between two adjacent points of the grid is the physical distance between two light rays traced through the BCA. The dimension of the grid is a user input to the simulation and the user chooses the number of rays that need to be traced through the BCA. The dimension of the grid is normally the same as the one used for representing the transverse Stokes variation of the object and doesn't have to be the same as the number of pixels in the detector.

Ray tracing can be viewed as an mapping of the input polarization definition at these discrete points of the grid to output intensity values. In case of models using Mueller calculus, polarization of an input ray at a transverse location defined by a Stokes vector is mapped to an output intensity value by Equation 3.18. In Jones calculus the polarization of the input ray defined by an input electric field vector is mapped to an output electric field vector which is then converted to an intensity value by Equation 3.34

The array of output intensity values in both Stokes and Jones simulation models have the same dimensions as the grid and is downsampled to the required dimensions by averaging neighboring intensities. The number of intensity values to be averaged

depends on the size of pixel used in the detector model and can be varied based on requirement. The averaging process desired is achieved using the rebin function in IDL.

Equations 3.34 and 3.18 have a built-in functional dependence on the phase difference of SVR 1 (ϕ_1) and SVR 2 (ϕ_2) evaluated at these points. The analytical forms for the phase differences are from Van Delden's work ([35]). The phase differences at the transverse coordinates of the entrance face are calculated based on BCA design values (inputs) determined by the user.

The simulation process is now simplified into a few well-defined steps:

1. Define the transverse positions on the entrance face of the crystal assembly for ray tracing.
2. Define the polarization of the light rays (Stokes or Jones vector) at these transverse locations.
3. Compute ϕ_1 and ϕ_2 at the transverse locations based on user inputs of wavelength of the light used, dispersion relation for the uniaxial birefringent crystal, thickness of the SVR, and the wedge angle.
4. Using the user input for the orientation of the transmission axis of the linear polarizer compute the output intensity array corresponding to the polarization states defined on the entrance face of the BCA.
5. Downsample the output intensity array to appropriate dimensions by averaging neighboring intensity values.

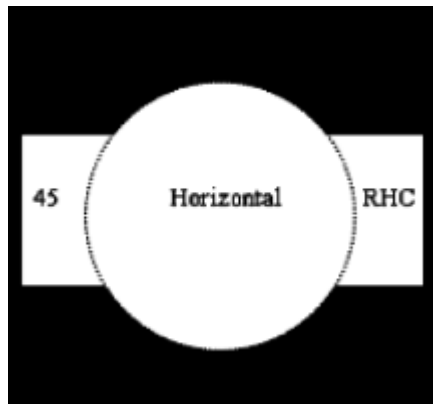
Polarization of input light	Intensity transmission of the BCA
Horizontal	0.44
Forty five (45)	0.40
RHC	0.50

Table 3.1: Transmission of the BCA.

3.7 Simulation example

An example demonstrating use of the developed simulation methodology to image an object through a telescope model and BCA onto the detector is presented in this section. A “satellite” object with SOP distribution as in Figure 3.4a is defined on a 512 X 512 array and is used as an input object for this simulation. The DOP of light exiting from all parts of the satellite object is chosen to be unity and hence the exiting light is completely polarized. A telescope (pupil radius = 20 pixels, FOV = 0.28 degrees, and focal length = 2 meters) images the input object onto the entrance face of the BCA. The uniaxial crystal wedges in the BCA is chosen to be made out of Yttrium Vanadate. The wedge angle used is 0.825264 degrees, and the crystal axes in the wedges of SVR 1 are oriented at 30 (left wedge) and 120 (right wedge) degrees with respect to the x axis while in SVR 2, the crystal axes are oriented at 150 (left wedge), and 60 (right wedge) degrees with respect to the x axis. The thickness of each SVR is 10mm, wavelength used for imaging is 600 nm and orientation of transmission axis of the linear polarizer is chosen to be 0 degrees with respect to the x axis.

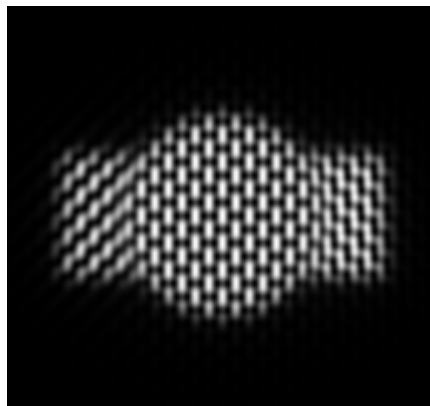
The image (Figure 3.4b) formed on entrance face of the BCA is of same dimensions (512 X 512 array) as the object and is normalized to have 50,000 photo detection events from the completely polarized object (DOP = 1). The normalized image is now propagated through the BCA assembly onto the detector. This propagation in a mathematical sense is using the input design values, Stokes vectors, and dispersion relations to compute intensity (Equation 3.18) in the output plane (immediately after



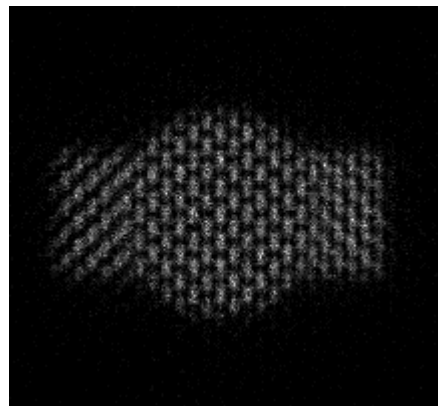
(a) Satellite object (input).



(b) Image on the entrance face of the BCA.



(c) Noise free fringe modulated output image.



(d) Noisy fringe modulated output image.

Figure 3.4: Simulation object and images at various stages.

the linear polarizer) and at the same transverse location as that of the image on the entrance face of the BCA. The image at the output plane has PDE less than 50,000 since the intensity transmittance of the BCA depends on the incident polarization state and is always less than 1 for any incident polarization state. The number of PDE at the image plane for a polarized input beam is a product of the number of photons incident on the entrance face of the BCA and intensity transmittance corresponding to the input polarization. The intensity transmission of the BCA design used in this work is shown in Table 3.1.

The image after propagation through the BCA is discretized to dimensions 256 X 256 to simulate a detector array with a pixel size of 19.4 micron. Figure 3.4c shows the discretized detector image before noise is added and detector image after corrupted with shot noise and read noise (normal distribution with mean =0 and standard deviation = 15) is shown in Figure 6.2.

CHAPTER 4

RECONSTRUCTOR ALGORITHM

A single image formed with the light that has passed through the BCA, either in a telescope configuration or a uniform beam configuration, contains complete polarization information encoded in the form of modulation of fringes. Stokes images are estimated from this fringe modulated image to present the polarization information. The modulated image to Stokes images conversion is done by a reconstructor algorithm. Reconstruction algorithms can be developed to use frequency domain or spatial domain measurements. In frequency domain algorithms [36], the fringe coded image is Fourier transformed and the amplitudes at specific spatial frequencies are used to compute the Stokes images. For algorithms based on spatial domain, the intensity values of the detector pixels are used to obtain the Stokes images. Several researchers including Oka, et al. [43, 44, 4, 5], Dereniak. et al.[45] have used the polarization information in the frequency domain for: the reconstruction of Stokes images; spatio-temporal stress analysis; characterizing spatio-temporal birefringent properties; and spectroscopic measurement of SOP. However, Van Delden [34] used a spatial approach to compute the Stokes images.

The reconstruction algorithm proposed and developed in this work is an extension of Van Delden's work [34] and hence based on the spatial domain approach. The concepts of a unit cell, polarization domain, pixel and detector geometry are addressed before the actual reconstruction algorithm is developed. The assumptions behind the algorithm, its step-wise development, and validity in terms of ability to reconstruct Stokes images under different SOP of input light are presented in a methodical fashion.

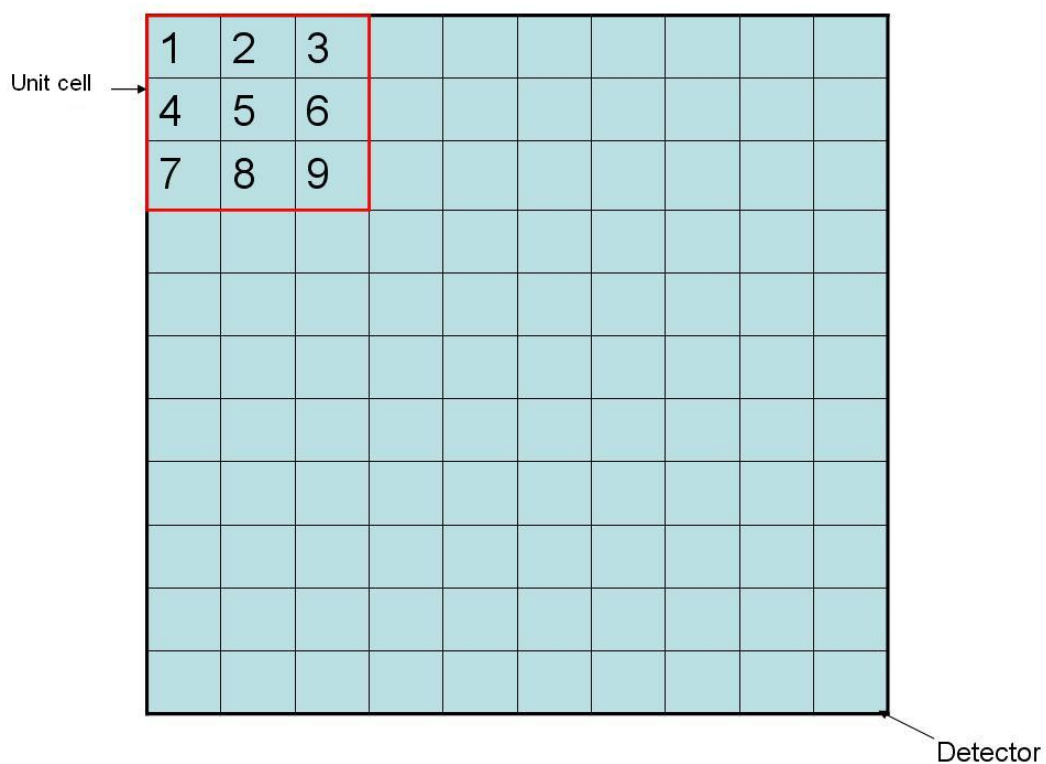
In this work the words reconstruction and estimation have been interchangeably, and essentially mean the same. This Chapter consists of the following topics :

- Unit cell, polarization domains, pixel and detector geometry.
- Reconstruction algorithm based on the Mueller approach.
- Reconstruction of calibration fringes.

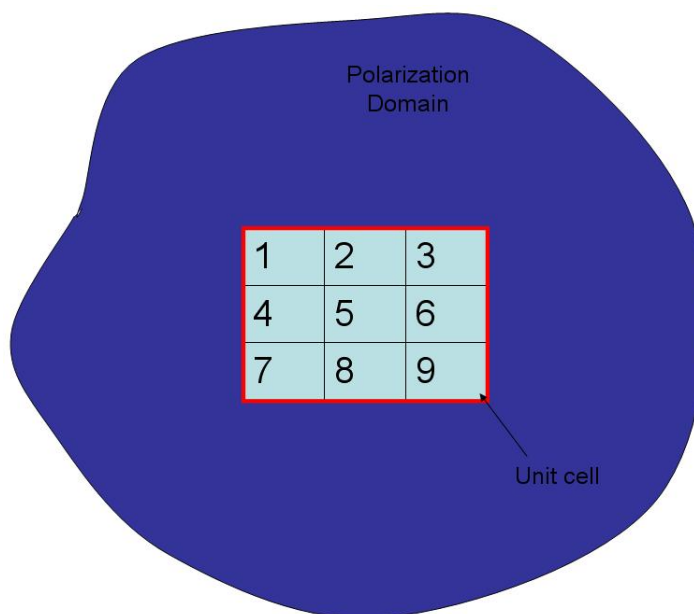
4.1 Unit cell, polarization domain, pixel and detector geometry

Understanding the sampling requirement for the detector and its pixels is essential for the development of the reconstruction algorithm. The detector is an array of pixels, which can be of different shapes and sizes. However, in this work the detector and its pixels are of rectangular and square shapes respectively as shown in Figure 4.1a. For simulation purposes, the physical dimensions of the detector and useful aperture of the crystal assembly are the same. In other words, it is assumed that the light beam diverges little after it passes through the crystal assembly before incident onto the detector. Equivalently, the electric field leaving the BCA can be relayed with some magnification to the plane of the detector array. The relayed and magnified beam is assumed to have the same extent as the exposed area of the detector.

Adjacent pixels of the detector combine to form a unit cell. The concept of a unit cell is important since it forms the basic unit over which Stokes reconstructions are performed. The physical dimensions of a unit cell depends on the size of the individual pixels making the unit cell and total number of the pixels in the unit cell. Figure 4.1a depicts a unit cell, which contain 9 pixels, as a part of the detector. In



(a) Detector and unit cell model.



(b) Sampling the polarization domain with a unit cell.

Figure 4.1: Geometry of the detector, unit cell and idea of a polarization domain.

this work, the unit cell chosen will have equal number of rows and columns i.e. square shaped unit cells.

The unit cell size for reconstruction is chosen based on the size of the polarization domains in the image. Polarization domains are regions within the image where the polarization and intensity of light varies little. For the derivation of the algorithm, the size of the unit cell is assumed to be less than the minimum polarization domain (Figure 4.1b). A quantitative discussion of the size of the unit cell with respect to the polarization domain will need the introduction of fore-optics and hence delayed till Chapter 5. Since polarization domains are regions within the fringe coded image incident on the detector, the physical size of the polarization domain is measured in units of pixels at the detector plane and an appropriate choice of unit cell size has to be made.

The concept of polarization domain and assumption of unit cell size compared to the polarization domain leads to a very important inference in this work: the polarization and intensity of incident light varies slowly over a unit cell. The choice of unit cell size does not affect the derivation of reconstruction algorithm as long it is smaller than the polarization domain.

In his work, Van Delden [34] limited the size of unit cell to 2×2 and reconstructions were performed in the absence of shot noise and read noise. Since information theory allows the reconstruction of the 4-element Stokes vector from four pixel measurements, a 2×2 unit cell can infact be used to reconstruct the polarization state over a unit cell. However in this work, the problems of using 2×2 unit cells and advantages of larger unit cells for Stokes reconstruction under presence of shot noise and read noise will be addressed. The issues of sampling, choosing pixel sizes, size of unit cells, and reconstruction errors in the presence of noise are important and are the focus of Chapters 5 and 6.

The reconstruction algorithm presented in the next section is essentially an extension of Van Delden's approach [34] to larger unit cells. However, with the retarder model Van Delden [42] used, the simulation method used in this work produced calibration fringes with either negative values or visibility < 1 for input light of DOP = 1 which does not accurately model the working principle of the BCA. Hence, in this work, a different retarder model [41] is used in the modeling the BCA. Moreover, the small angle approximation used by Van Delden [35] - the angle of refraction of the secondary and tertiary rays in the SVRs are assumed to be small due to the limit imposed on the value of the wedge angle i.e. wedge angle < 0.2 radians is not considered in this work.

4.2 Reconstruction based on Mueller approach

The reconstruction algorithm developed in this part of the work is based on the Mueller matrix model in section 3.2.1. The intensity of light exiting the crystal assembly is given by Equation 3.18:

$$O(x, y) = S'_o(x, y) = (1/2)[S_0(x, y)F_0(x, y) + S_1(x, y)F_1(x, y) + S_2(x, y)F_2(x, y) + S_3(x, y)F_3(x, y)]$$

where $O(x, y)$ represents the intensity of exiting light,

$S_0(x, y), S_1(x, y), S_2(x, y), S_3(x, y)$ are the Stokes components of the light incident on the entrance face of the BCA,

$F_0(x, y), F_1(x, y), F_2(x, y), F_3(x, y)$ are the first row Mueller matrix entries (see Equation 3.6) and given by Equations 3.7, 3.8, 3.9, and 3.10. Given that $F_0(x, y)$ is a constant (Equation 3.7), it is seen from Equation 3.18 that $F_1(x, y)$ for an actual instrument can be computed with the knowledge of $S_0(x, y), S_1(x, y), O(x, y)$ when the parameters $S_2(x, y), S_3(x, y)$ are made zeros. In fact, the horizontal calibration fringe output from the instrument can be readily used to compute $F_1(x, y)$ since $S_0(x, y)$ is a

known quantity, $S_2(x, y) = S_3(x, y) = 0$, $S_1(x, y) = S_0(x, y)$ and $O(x, y)$ is the output intensity. Similarly, $F_2(x, y)$ and $F_3(x, y)$ for an actual instrument can be computed from the 45 and RHC calibration fringe patterns respectively. This leads to an important inference, to compute the Stokes images from the fringe modulated image, only three calibration fringe patterns (horizontal, 45 and RHC) are needed. This inference is validated when it is noted that the orthogonal fringe patterns (horizontal and vertical, 45 and 135, RHC and LHC) are complementary to each other and add up to the same constant value when beams used to create them have the same intensity. In general, the BCA does not produce any fringe pattern (zero visibility) when the incident light, a uniform beam or an image from the telescope, on the entrance face of the BCA is unpolarized. In fact the BCA produces an output image with same constant value across it when a uniform intensity beam (unpolarized) illuminates its entrance face. Hence a constant (zero visibility) across the image implies that the light in the image is unpolarized. So two complementary fringe patterns with the same amplitude adding together to form a constant value, for example:

$$\begin{bmatrix} A \\ A \\ 0 \\ 0 \end{bmatrix} + \begin{bmatrix} A \\ -A \\ 0 \\ 0 \end{bmatrix} = \begin{bmatrix} 2A \\ 0 \\ 0 \\ 0 \end{bmatrix}$$

as required. A is the intensity of the individual input beams.

Consider the unit cell shown in Figure 4.2. This unit cell with 9 pixels is used to present the development of the algorithm. The detector is made of several such unit cells and the reconstruction algorithm has to be run over each unit cell in order to compute the Stokes images over the complete field of view of the detector. Each pixel in the unit cell sees an intensity of incident light given by Equation 3.18. A modified

1	2	3
4	5	6
7	8	9

Figure 4.2: Pixel representation in a unit cell.

version of Equation 3.18 for a unit cell is introduced as:

$$O_n = (1/2)[S_0 + S_1F_{n1} + S_2F_{n2} + S_3F_{n3}] \quad (4.1)$$

where n stands for the pixel number within the unit cell. $F_0(x, y)$ is dropped from the equation since its value is unity. The spatial dependence of S_0, S_1, S_2, S_3 has also been dropped since the light over a unit cell varies little in intensity and polarization (based on the inference made in section 4.1). The continuous spatial variation of O, F_1, F_2 , and F_3 is discretized by adding n as an additional subscript to them i.e. O_n, F_{n1}, F_{n2} , and F_{n3} . In essence, Equation 4.1 models the detector's digitization effect on incident light.

For the unit cell shown in Figure 4.2, the intensity of light as seen by each pixel based on Equation 4.1, is written as follows:

$$\begin{aligned}
O_1 &= (1/2)[S_0 + S_1 F_{11} + S_2 F_{12} + S_3 F_{13}] \\
O_2 &= (1/2)[S_0 + S_1 F_{21} + S_2 F_{22} + S_3 F_{23}] \\
&\vdots \\
O_9 &= (1/2)[S_0 + S_1 F_{91} + S_2 F_{92} + S_3 F_{93}]
\end{aligned} \tag{4.2}$$

Thus a set of linear equations that map the input Stokes vector to the output pixel intensities is created. The set of Equations 4.2 is now written in the following matrix form:

$$\begin{bmatrix} O_1 \\ O_2 \\ \vdots \\ O_9 \end{bmatrix} = (1/2) \begin{bmatrix} 1 & F_{11} & F_{12} & F_{13} \\ 1 & F_{21} & F_{22} & F_{23} \\ \vdots & \vdots & \vdots & \vdots \\ 1 & F_{91} & F_{92} & F_{93} \end{bmatrix} \begin{bmatrix} S_0 \\ S_1 \\ S_2 \\ S_3 \end{bmatrix} \tag{4.3}$$

or

$$\vec{\mathbf{O}} = \mathbf{F} \vec{\mathbf{S}}$$

and

$$\vec{\mathbf{S}} = ((\mathbf{F}^T \mathbf{F})^{-1} \mathbf{F}^T) \vec{\mathbf{O}}$$

where

$$\mathbf{F} = (1/2) \begin{bmatrix} 1 & F_{11} & F_{12} & F_{13} \\ 1 & F_{21} & F_{22} & F_{23} \\ \vdots & \vdots & \vdots & \vdots \\ 1 & F_{91} & F_{92} & F_{93} \end{bmatrix}, \tag{4.4}$$

$$\mathbf{O} = \begin{bmatrix} O_1 \\ O_2 \\ \vdots \\ O_9 \end{bmatrix}, \quad \vec{\mathbf{S}} = \begin{bmatrix} S_0 \\ S_1 \\ S_2 \\ S_3 \end{bmatrix} \quad \text{and} \quad \vec{\tilde{\mathbf{S}}} = \begin{bmatrix} \tilde{S}_0 \\ \tilde{S}_1 \\ \tilde{S}_2 \\ \tilde{S}_3 \end{bmatrix}.$$

The matrix \mathbf{F} is of dimensions $(N_r^2) \times 4$, where N_r is the number of rows in the unit cell while \mathbf{O} is a matrix of dimensions $(N_r^2) \times 1$. The vectors $\vec{\mathbf{S}}$ and $\vec{\tilde{\mathbf{S}}}$ represent the input Stokes vector and estimated Stokes vectors respectively.

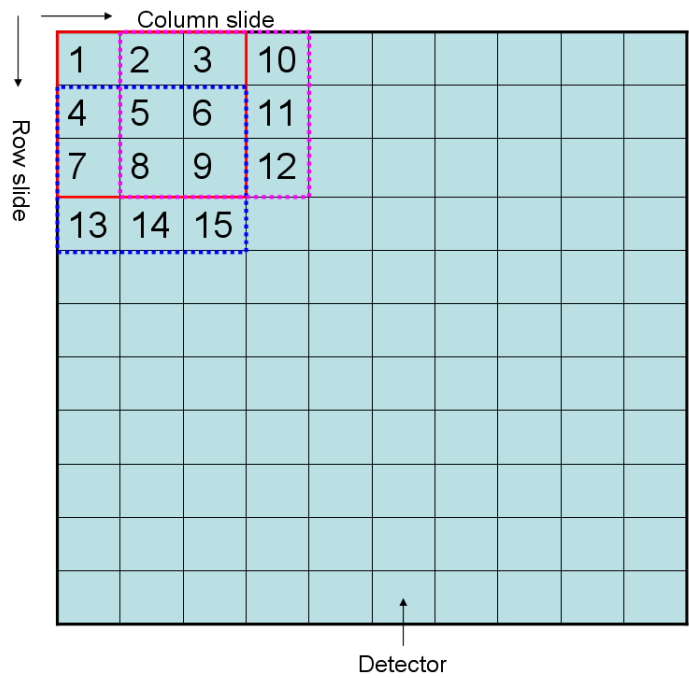
In order to compute the Stokes components in the unit cell, the inverse problem

$$\vec{\tilde{\mathbf{S}}} = ((\mathbf{F}^T \mathbf{F})^{-1} \mathbf{F}^T) \vec{\mathbf{O}}$$

is solved and each pixel in the unit cell has the same Stokes components \tilde{S}_0 , \tilde{S}_1 , \tilde{S}_2 , and \tilde{S}_3 . Since the matrix \mathbf{F} (dimensions $(N_r^2) \times 4$) is not a square matrix, $((\mathbf{F}^T \mathbf{F})^{-1} \mathbf{F}^T)$ is computed using the pseudo inverse and not the regular matrix inversion.

In theory, a 2×2 unit cell is the minimum sized unit cell needed to reconstruct the Stokes images from the single fringe coded detector image. This size would produce a set of four equations as in Equation set 4.2 and the size of the \mathbf{F} matrix would be 4×4 which is sufficient to reconstruct the four Stokes parameters \tilde{S}_0 , \tilde{S}_1 , \tilde{S}_2 , and \tilde{S}_3 in that unit cell. But there are some practical problems in using a 2×2 unit cell which are addressed in Chapter 5.

After the Stokes components are reconstructed for a particular unit cell, the next reconstruction can be performed on a completely new unit cell adjacent to the previous one and this process can be continued until the reconstruction is completed over the entire detector array. This kind of reconstruction method is termed as a discrete reconstruction method. However, in this work, a slide reconstruction method (slide

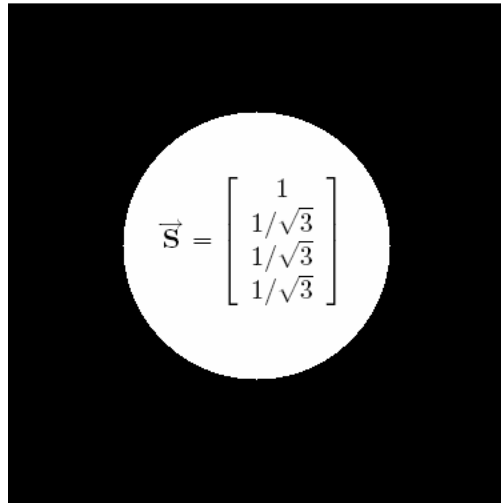


(a) Slide reconstruction.

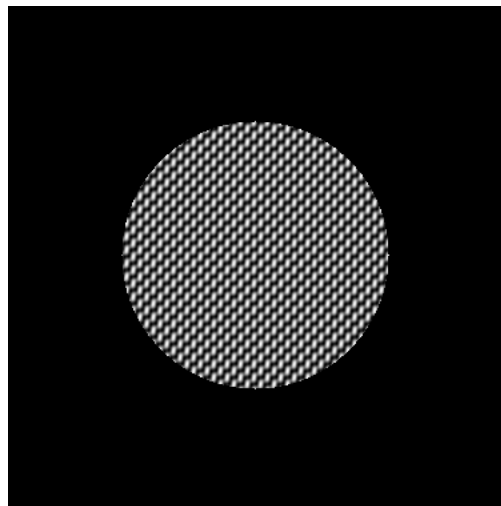
1	2	3	3	3	3	3	3	2	1
2	4	6	6	6	6	6	6	4	2
3	6	9	9	9	9	9	9	6	3
3	6	9	9	9	9	9	9	6	3
3	6	9	9	9	9	9	9	6	3
3	6	9	9	9	9	9	9	6	3
3	6	9	9	9	9	9	9	6	3
3	6	9	9	9	9	9	9	6	3
3	6	9	9	9	9	9	9	6	3
2	4	6	6	6	6	6	6	4	2
1	2	3	3	3	3	3	3	2	1

(b) Averaging array.

Figure 4.3: Reconstruction technique.



(a) Input object.



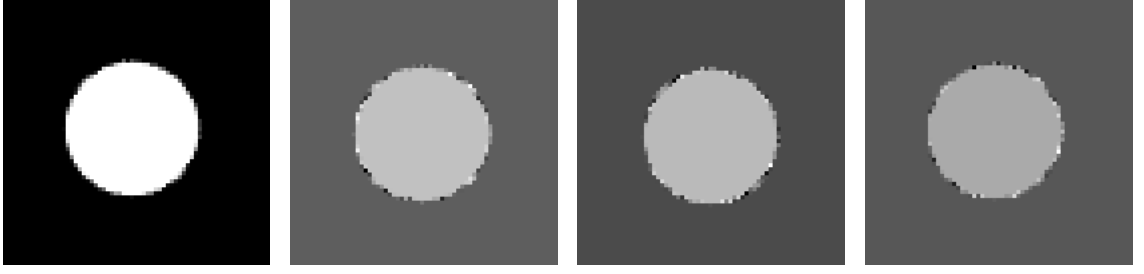
(b) Detector image.

Figure 4.4: Circular object and fringe modulated image.

approach or slide reconstructor) is employed for estimating the Stokes components over the entire detector array. This concept is illustrated in Figure 4.3a. Once the Stokes components in the red unit cell are estimated, the 3×3 kernel is slid by a pixel either along the column (pink unit cell) or row (blue unit cell), and Stokes components are estimated again. In the case of a column slide by a pixel, the Stokes components for pixels 2, 3, 5, 6, 8, and 9 are estimated twice: once in the red unit cell and a second time in the pink unit cell. Similarly, for a row slide by a pixel, the Stokes components for 4, 5, 6, 7, 8, and 9 are estimated twice: once in the red unit cell and a second time in the blue unit cell. The process of sliding the kernel and estimating the Stokes components continues until the entire detector is spanned. Based on the location in the detector array and size of the unit cell, each pixel gets multiple reconstructions for the same Stokes component. Whenever this situation arises, the average value of the multiple reconstructions of the Stokes component is taken.

The pixels at the corners of the detector are estimated once and pixels towards the center of the detector are estimated multiple times. When the size of the unit cell is 3×3 , the edge of the detector is estimated once and center of the detector is estimated 9 (3×3) times. To keep track of the number of estimations of each pixel in the detector array, an integer array is created. In this array, each pixel position is incremented by one each time the kernel uses the corresponding pixel for reconstruction. When the kernel spans the detector completely, this array contains a complete account of how many times each pixel is estimated, whereby an appropriate averaging can be applied to each pixel. Integer values by which each pixel is averaged is demonstrated in Figure 4.3b.

Slide approach is useful when larger unit cells are used for the reconstruction of images with significant noise. In addition to this benefit, the slide approach provides a



(a) S_0, S_1, S_2, S_3 images from discrete reconstructor method.



(b) S_0, S_1, S_2, S_3 images from slide reconstructor method.

Figure 4.5: Reconstructed Stokes images using a 3 X 3 unit cell.

smoothing effect on the edges in images (polarization changes occurs usually at edges) and greatly reduces the reconstruction errors associated with it. Reconstruction is performed over the entire detector and no pixels are left out. As an example, a horizontally polarized circular object (100 pixel radius defined on a 512 X 512 array) or beam with a diameter less than the physical dimensions of the entrance face of the BCA as shown in Figure 4.4a, is imaged through the BCA onto the detector and discretized to 256 X 256 to model the averaging effect of the pixels in the detector. Figure 4.4b shows the discretized fringe modulated image from the detector without any noise. The Stokes images are reconstructed using both discrete reconstruction method (Figure 4.5a) and slide reconstruction method (Figure 4.5b). An Error Metric (EM) of the following form:

$$EM = \sum_{S_0, S_1, S_2, \text{ and } S_3} Avg\left(\frac{abs(TSI - RSI)}{TSI}\right) \quad (4.5)$$

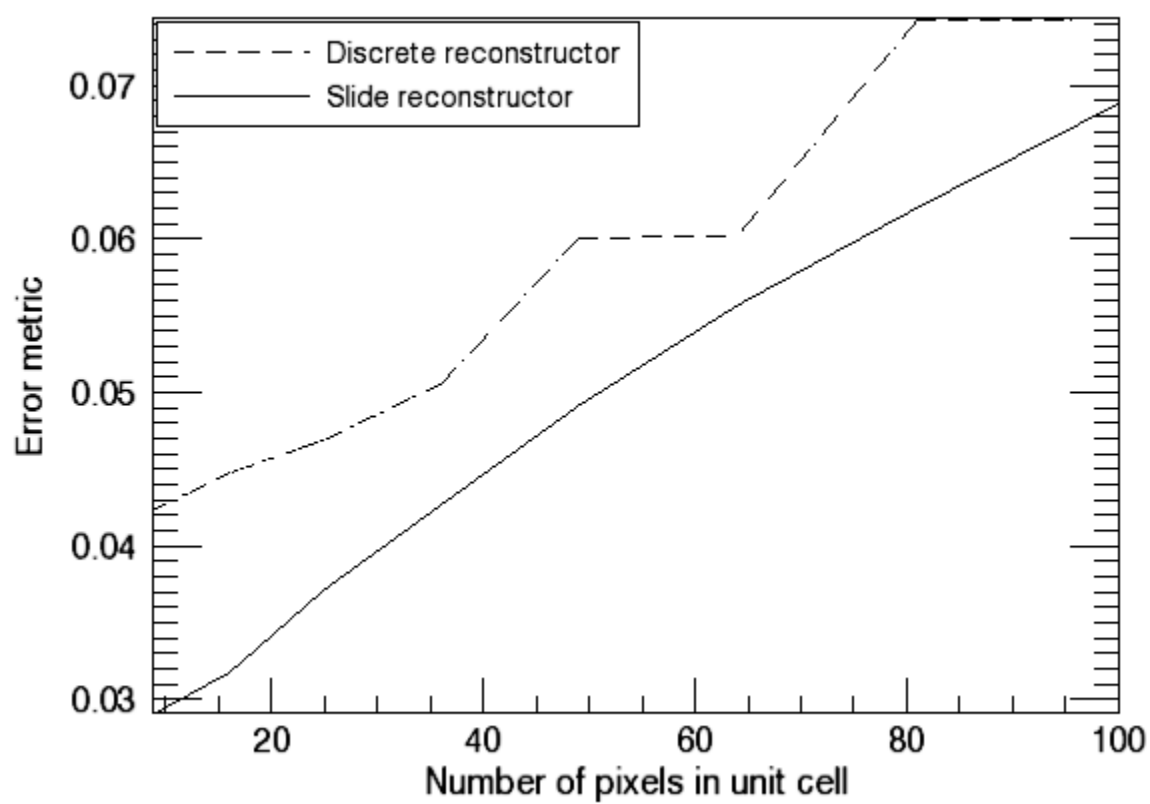


Figure 4.6: Comparison of reconstruction methods.

is evaluated for both cases. *TSI* and *RSI* refer to the True Stokes Image and Reconstructed Stokes Image respectively. *EM* is only evaluated for regions of the image for which the incident intensity value is greater than zero. Figure 4.6 shows the variation of the error metric as a function of the number of pixels in the unit cell and it is seen that the slide reconstruction method performs relatively better than the discrete method. The effectiveness of slide reconstruction method due to the built-in averaging will be much more evident in Chapters 5 and Chapter 6, where the Stokes images are reconstructed under various conditions (different illumination levels and noise).

4.3 Reconstruction of calibration fringes

Calibration fringes are created by directing beams of light (one at a time) into the crystal assembly at normal incidence. These beams are uniform in intensity and polarization (see section 3.2.3). In practical environments, a polarization state generator (PSG) or polarization calibration optics, along with a uniform source, can be used to generate such beams. The polarization calibration optics would be a linear polarizer and a quarter wave plate (designed to be efficient at the wavelength of interest) while the uniform sources could be an integrating sphere, a sheet of spectralon, the daylight sky, or even the defocused moon. The integrating sphere and spectralon is preferable compared to other sources as the light from them are unpolarized and the output intensity will not change as the linear polarizer in the calibration optics is rotated. However, if uniform polarized sources are used then total energy changes can be compensated by rescaling the calibration fringes to have the same total number of counts.

The calibration fringes obtained from the crystal assembly are imaged by the detector. In order to reconstruct these calibration fringes into meaningful Stokes images

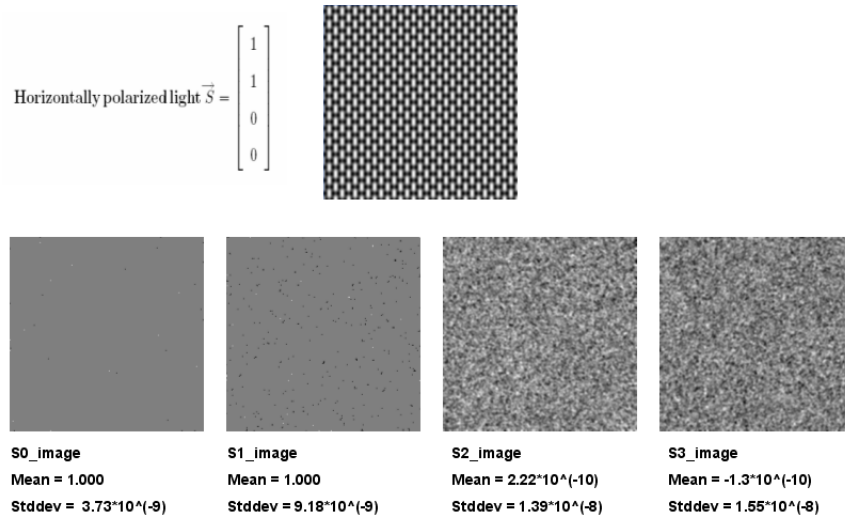


Figure 4.7: Reconstruction of horizontal calibration fringes.

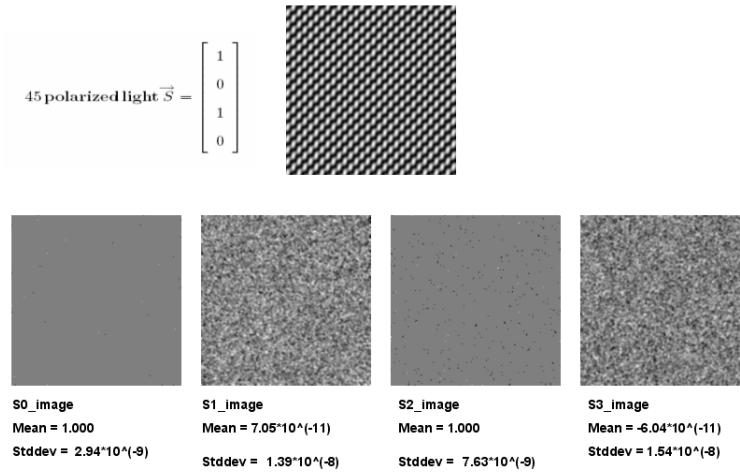


Figure 4.8: Reconstruction of 45 calibration fringes.

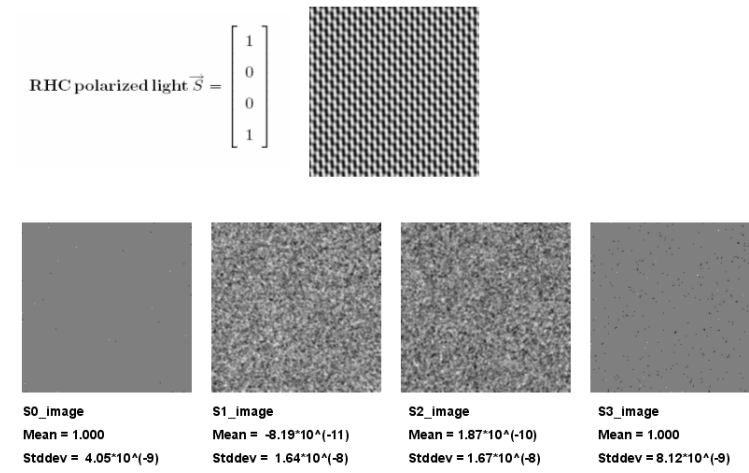


Figure 4.9: Reconstruction of RHC calibration fringes.

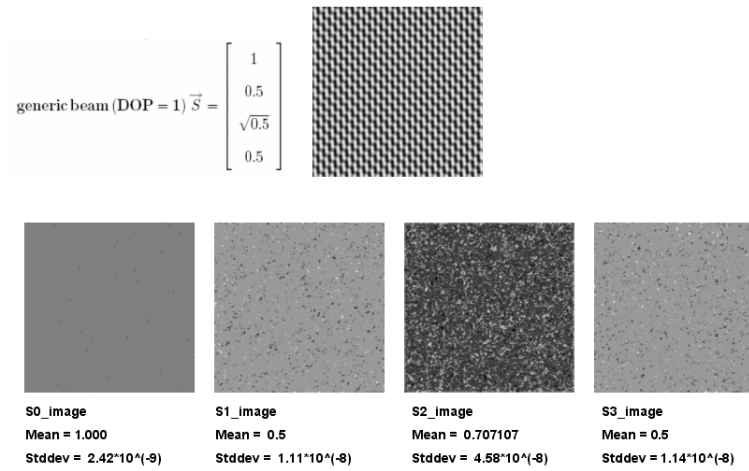


Figure 4.10: Reconstruction of a generic fringe pattern.

and test the developed algorithm, the slide reconstructor is applied on the calibration fringe images and the results are in Figures 4.7, 4.8, and 4.9. The maximum amplitude and minimum amplitude of the fringes in each of the calibration fringe images is equal to one and zero respectively. The mean and standard deviation are the metrics used to test the validity of the slide reconstructor. While the magnitude of the mean value of a particular reconstructed Stokes image gives an idea about the intensity of the incident light in that Stokes component, the sign shows its preferential direction. The standard deviation shows the variation of the incident light intensity over a particular Stokes image. Since the test cases use uniform beams, the mean value of the Stokes images should be close to the ones shown in the components of the input Stokes vector and the standard deviation should be negligible (Figures 4.7, 4.8, and 4.9). It is evident that the reconstructed images: S_0_images , S_1_images , S_2_images , and S_3_images are in excellent agreement with the polarization and intensity of the input light. Considering the values of the mean and standard deviation, the reconstruction error is negligible.

To test the algorithm further, the slide reconstructor is applied to a fringe pattern created by a generic beam. This fringe pattern is also produced by a beam of light whose intensity and polarization are uniform. The polarization in this case is not purely horizontal or 45 or RHC but a mixture of each as shown in Figure 4.10. The mean and standard deviation values of the reconstructed Stokes images compared to the Stokes parameters of the input beam, shown in Figure 4.10, reveal that the slide reconstructor estimates are accurate even when the input beam has a combination of polarizations. Thus, a reconstruction algorithm defined as a slide reconstructor is successfully created, tested and is now ready to be used for the reconstruction of fringe modulated images.

CHAPTER 5

SAMPLING REQUIREMENTS

Cameras or Imaging systems use detector arrays to convert analog images to discretized digital images. The images in the case of the ISIP, either calibration fringe images or object-images, contain fringes that carry polarization information. The modulation of these fringes has to be preserved during the discretization and digitization process of the detector by a careful choice of pixel size. The optimal pixel size is chosen based on the condition number variation of the measurement matrix with pixel size. If the polarization information is included in the image along with a projection of the object, basic information theory considerations mean the density of pixels per unit area must be higher than the density required for the image without polarization information. The effects of increased number of pixels (larger unit cells) on condition number of the measurement matrix is also investigated.

The presence of a upper limit on the size of the unit cell relative to the PSF will be shown in this Chapter. This limit relates the unit cell size to PSF of the optical system (telescope) used in imaging the object or scene. The validity of the proposed limit is tested by a simulation whereby a point source equally polarized in S_0, S_1, S_2 , and S_3 is imaged through an optical system (telescope) of fixed PSF size. The detected image (fringe coded) is then reconstructed into Stokes images using unit cells of increasing dimensions. An error metric is evaluated for each case and plotted as a function of the number of unit cells sampling the PSF. This Chapter consists of the following sections:

- Tracing rays, pixel size and detector model.
- Singular value decomposition and condition numbers.
- Choosing pixel sizes, wedge angles and unit cells based on condition number as a metric.
- Nyquist sampling the PSF.

5.1 Tracing rays, pixel size and detector model

The fundamental ideas of the Mueller model approach and polarization to fringe mapping have been developed in section 3.2.1. These ideas involve computations at various locations on the transverse spatial plane defined at the entrance face of the crystal assembly. Light rays are traced through the assembly at these locations. In the Mueller matrix model, tracing the light rays is equivalent to multiplying the Stokes vectors of the input light with the combined Mueller matrix of the crystal assembly to produce output Stokes vectors. The density of the traced light rays depends on the choice of locations (grid) on the transverse spatial plane.

In this work it is assumed that the light passing through the crystal assembly does not diverge significantly before it is incident on the detector or equivalently, the interference plane is relayed onto the detector with some magnification from the relay optics. Hence an image of the detector projected on the entrance face (or clear aperture) of the crystal assembly would have the same physical dimensions as the entrance face of the BCA. Relay optics with a given magnification can be used to project the field near the BCA onto the detector, but there is no loss of generality in assuming unit magnification. Such a projection would help in the visualization

of spatial locations of the light rays that correspond to each pixel of the detector array. Propagating these light rays through the crystal assembly and averaging their corresponding output intensities would produce a discretized intensity value which is the output from that pixel of the detector. Repeating the procedure over the entire spatial plane would give the complete intensity outputs for all the pixels in the detector array.

A bundle of light rays can be traced through the crystal assembly by appropriate choice of locations (grid dimensions) on the spatial plane. The number of rays to be averaged per pixel will depend on the ray spacing and size of each detector pixel. In the simulation model used in this work, a square grid is used to define the position of rays on the entrance face of the BCA and these rays are propagated through the crystal assembly to form an output array of intensity values. This array is downsampled by averaging neighboring intensity values to a lower dimensional array based on pixel sizes in the detector array. The ray spacing is chosen so the same number of rays (4 rays) is averaged in each detector pixel. This kind of an approach sufficiently models the actual detector with no noise.

The choice of pixel size is influenced by the highest frequency of the image content. For incoherent imaging the highest frequency is normally determined by the pupil diameter and wavelength. Detector pixel size is selected based on the Whitaker-Shannon sampling theorem: the sampling frequency, f_s (inverse of the pixel dimension) is selected to be at least twice the highest spatial frequency content, f_{max} contained in the image i.e $f_s \geq f_{max}$. Pixel sampling at spatial rates smaller than this minimum will result in energy at relatively high frequencies being aliased into lower frequencies, causing the sampled image to differ from an idealized or continuous representation. In images from the ISIP, the maximum spatial frequency are from the fringes encoding the polarization information as the scene variations would be slowed

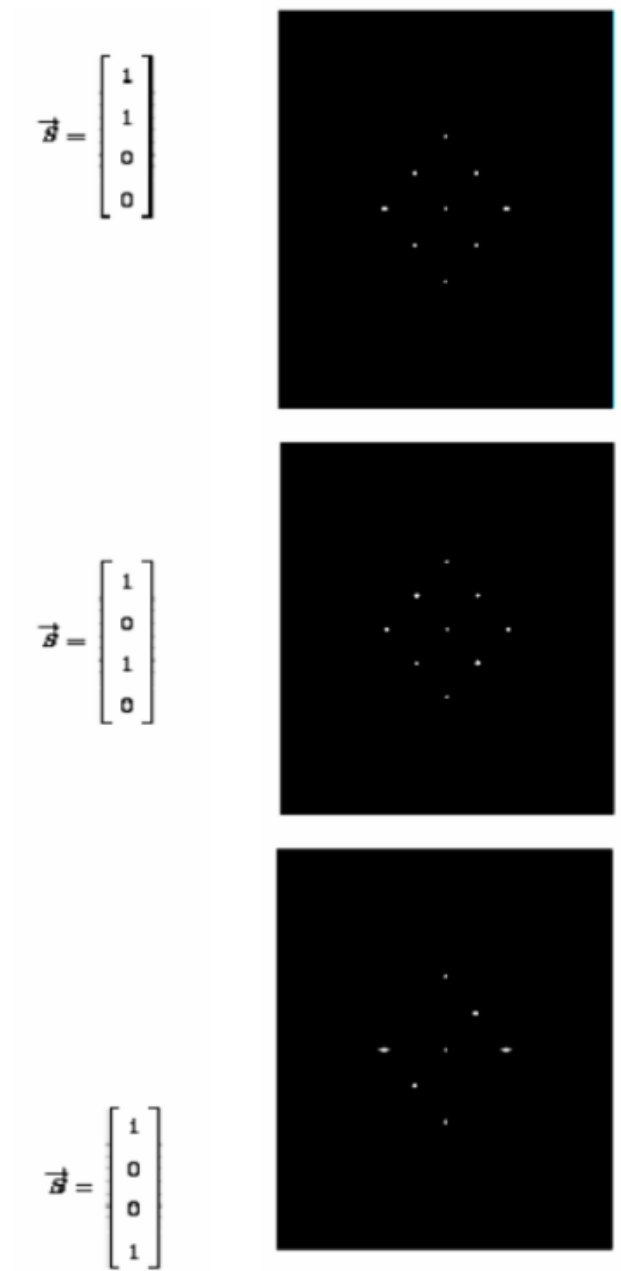


Figure 5.1: Magnitude of Fourier spectrum of the calibration fringes.

compared to the calibration fringes by a correct choice of PSF and unit cell size (section 5.4).

From the Fourier spectrum of the calibration fringes in Figure 5.1 it is seen that the highest spatial frequency in each of the calibration fringe image is the same. Hence, a pixel size chosen to Nyquist sample one calibration fringe pattern should sufficiently sample others. The process of decreasing the pixel sizes (where the size of clear aperture, physical size of the detector and wedge angle are fixed) that sample the calibration fringes results in an increased number of computations due to the increase in grid dimensions defined on the entrance face of the BCA. The number of required computations varies as a square of the factor by which the pixel size is reduced. For example, when the pixel size is reduced by a factor of two the required number of computations increases by a factor of four and the computation time for both simulation and reconstruction increase by a factor of 3 each. As the pixel size is further decreased the the grid dimensions will increase further and computation times will increase significantly. To avoid this problem, pixel size and number of pixels in the detector array is fixed at a desired value and changes to wedge angle are used to adjust the period of the calibration fringes until the chosen pixel size Nyquist samples the calibration fringes. There is no loss in generality in our conclusions.

In Figure 5.2 the side lobe corresponding to the highest frequency content and the central peak in the Fourier spectrum of the horizontal calibration fringes are shown. It is seen that the side lobes corresponding to the highest frequency component have a spread and the side lobes start moving away from the central peak as the wedge angle (with fixed pixel size) of the SVRs is increased.

The detector model used in this work can be analyzed using a frequency domain representation. In the Fourier domain each pixel represents a frequency band equal to the inverse of the total array size in the spatial domain. These frequency domain

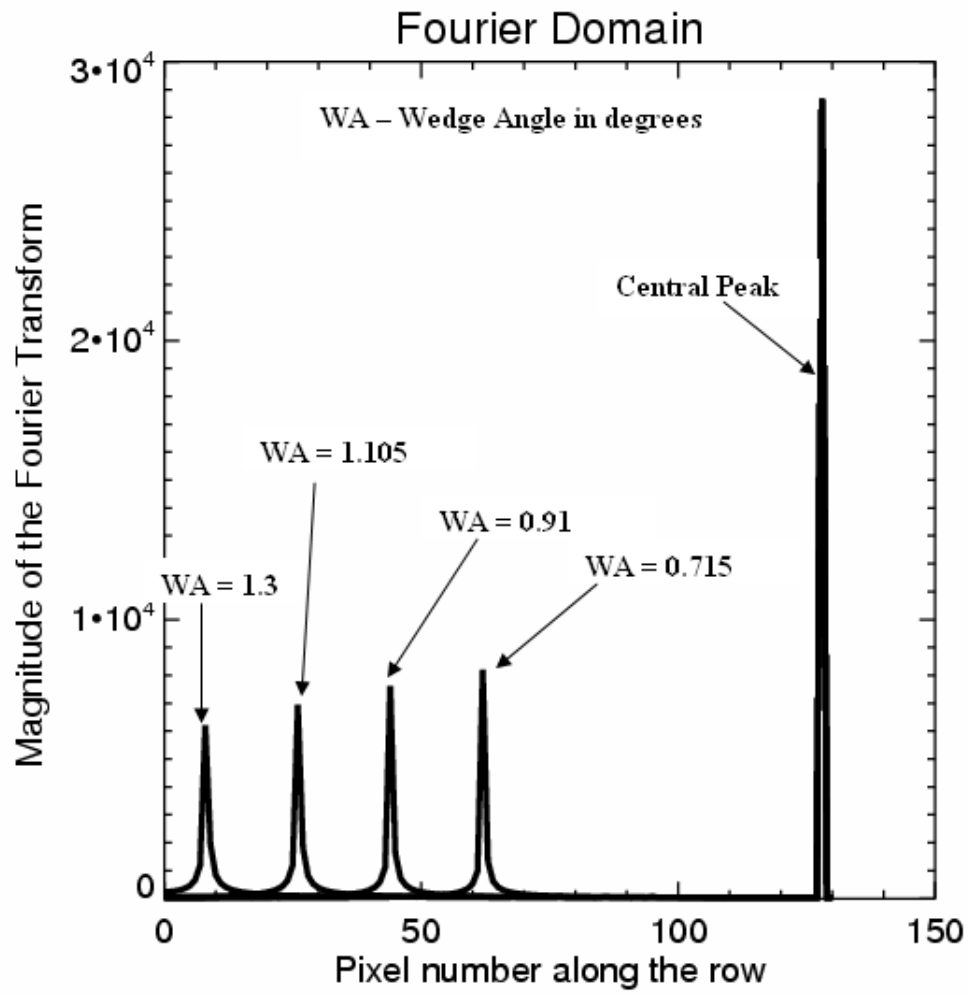


Figure 5.2: The changes in position of side lobe as function of the wedge angle.

pixels discretize the central and side lobes (Figure 5.2) to produce an array of complex values in the Fourier domain. The side lobes in Figure 5.2 move over these frequency domain pixels (away from the central lobe) as the wedge angle of the SVRs is increased and appear to have different spreads in the discretized array based on the position of its peak with respect to the frequency domain pixels. The varying spreads of the side lobes makes the definition of Nyquist sampling challenging.

A small initial wedge angle that positions the peak of the side lobe at the center of a frequency domain pixel and close to the central lobe was selected by trial and error. This was visually confirmed by noting the minimum spread and maximum amplitude of the side lobe. Moreover, it was noted that there is a linear relationship between the wedge angle and fringe frequency of the calibration fringes - doubling the wedge angle doubled the fringe frequency. New wedge angle increments are chosen as the positive integer multiples of the initial small wedge angle so that the peaks of the side lobes maintain their position with respect to a frequency domain pixel thereby keeping the spread of the side lobe equal. As the wedge angle is incremented, Nyquist sampling in this work is defined to occur when the outer-tail value of the side-lobe at the edge of the array reaches 0.2 % of the side lobe peak.

The Nyquist sampling of calibration fringes produced by a BCA of transverse dimensions 4.97 mm by 4.97 mm and thickness 10mm with a 256 X 256 detector array of pixel size 19.42 micron occurs at a wedge angle of 1.105 degrees. The Nyquist sampled calibration fringes are shown in Figure 5.3. In summary, the Nyquist sampling in this work is achieved by the following steps:

1. The physical dimensions of the detector (4.97 mm by 4.97 mm) is assumed to be the same as the entrance face of the BCA.

2. A detector array of chosen dimensions (256 X 256 pixels) samples the calibration fringes.
3. The physical dimensions of the BCA's clear aperture and the array dimensions detector determines the pixel size (19.42 micron).
4. The choice of the grid dimensions determines the ray trace locations on the front face of the BCA.
5. Light rays at the grid locations are propagated through the BCA to form output intensity array.
6. The output intensity array is downsampled from 512 X 512 to 256 X 256 (4 rays per pixel) by averaging neighboring intensities to form the discretized detector output array.
7. The wedge angle of the crystal assembly is adjusted until the determined pixel size Nyquist samples the calibration fringes.

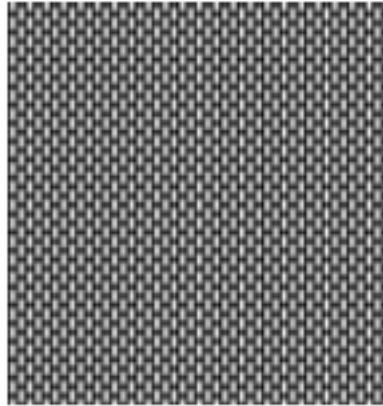
5.2 Singular value decomposition and condition numbers

The Linear System used in this work is of the form:

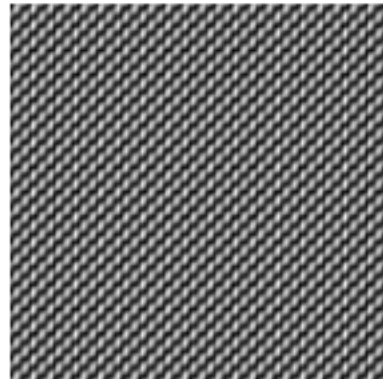
$$\vec{\mathbf{O}} = \mathbf{F} \vec{\mathbf{S}} \tag{5.1}$$

where

$$\vec{s} = \begin{bmatrix} 1 \\ 1 \\ 0 \\ 0 \end{bmatrix}$$



$$\vec{s} = \begin{bmatrix} 1 \\ 0 \\ 1 \\ 0 \end{bmatrix}$$



$$\vec{s} = \begin{bmatrix} 1 \\ 0 \\ 0 \\ 1 \end{bmatrix}$$

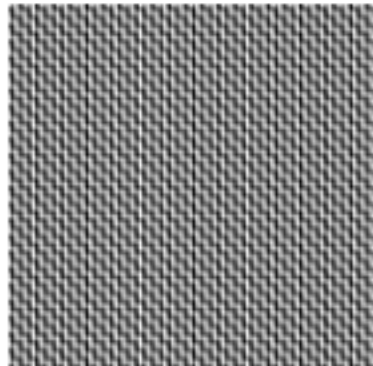


Figure 5.3: Nyquist sampled calibration fringes.

$$\mathbf{F} = (1/2) \begin{bmatrix} 1 & F_{11} & F_{12} & F_{13} \\ 1 & F_{21} & F_{22} & F_{23} \\ 1 & \vdots & \vdots & \vdots \\ 1 & F_{M1} & F_{M2} & F_{M3} \end{bmatrix}$$

$$\vec{\mathbf{O}} = \begin{bmatrix} o_1 \\ o_2 \\ \vdots \\ o_M \end{bmatrix}, \quad \vec{\mathbf{S}} = \begin{bmatrix} S_0 \\ S_1 \\ S_2 \\ S_3 \end{bmatrix}$$

and M represents total number of pixels in the unit cell. The meaning of each vector, matrix and their elements are explained in section 4.2. In Equation 5.1, \mathbf{F} (Measurement matrix) can be a non-square matrix and its size depends on the number of pixels in the unit cell. A decomposition of the matrix \mathbf{F} using singular value decomposition gives insight into the natural sensitivity of the problem described in Equation 5.1. The matrix \mathbf{F} can be written as:

$$\mathbf{F} = \mathbf{U} \boldsymbol{\sigma} \mathbf{V}^T \tag{5.2}$$

$$\mathbf{F} = \begin{pmatrix} & \mathbf{U} \end{pmatrix} \begin{pmatrix} \sigma_1 & 0 & 0 & 0 \\ 0 & \sigma_2 & 0 & 0 \\ 0 & 0 & \sigma_3 & 0 \\ 0 & 0 & 0 & \sigma_4 \\ \vdots & \vdots & \vdots & \vdots \end{pmatrix} \begin{pmatrix} \mathbf{V}^T \end{pmatrix}$$

where \mathbf{F} is a $M \times 4$ matrix, \mathbf{U} is a $M \times M$ real unitary matrix ($\mathbf{U}^T \mathbf{U} = \mathbf{1}$), \mathbf{V} is a

$M \times 4$ real unitary matrix ($\mathbf{V}^T \mathbf{V} = \mathbf{1}$) and σ is a $M \times 4$ diagonal matrix of singular values.

The rows of \mathbf{V}^T form an orthonormal basis for the row space of \mathbf{F} and are the eigen vectors of $\mathbf{F}^T \mathbf{F}$. The columns of \mathbf{U} form an orthonormal basis for the column space of \mathbf{F} and are the eigen vectors of $\mathbf{F} \mathbf{F}^T$. The singular values on the diagonal of σ are the square root of the non-zero eigen values of $\mathbf{F}^T \mathbf{F}$ and $\mathbf{F} \mathbf{F}^T$. Representation of \mathbf{F} based on Equation 5.2 and it's action on $\vec{\mathbf{S}}$ can be interpreted as follows:

1. $\mathbf{p} = \mathbf{V}^T \vec{\mathbf{S}}$. The input vector $\vec{\mathbf{S}}$ is projected onto an orthonormal basis for the row space of \mathbf{F} resulting in the vector \mathbf{p} of size 4×1 . The elements of \mathbf{p} are result of the inner product between the basis vectors (rows of \mathbf{V}^T) and $\vec{\mathbf{S}}$.
2. $\mathbf{g} = \sigma \mathbf{p}$. The elements of \mathbf{p} are weighted or amplified by their respective singular values to form the $M \times 1$ vector \mathbf{g} .
3. $\mathbf{d} = \mathbf{U} \mathbf{g}$. The gain weighted elements of \mathbf{g} now become the coefficients that multiply the respective columns of \mathbf{U} in the linear combination of the columns of \mathbf{U} that form the 4×1 vector \mathbf{d} .

A similar analysis can be applied to the inverse problem. In the case of the inverse problem where $\vec{\mathbf{S}}$ is estimated, Equation 5.1 becomes

$$\vec{\mathbf{S}} = ((\mathbf{F}^T \mathbf{F})^{-1} \mathbf{F}^T) \vec{\mathbf{O}} \quad (5.3)$$

where $((\mathbf{F}^T \mathbf{F})^{-1} \mathbf{F}^T)$ is the pseudo-inverse of \mathbf{F} , and

$$((\mathbf{F}^T \mathbf{F})^{-1} \mathbf{F}^T) = \mathbf{V} (1/\sigma) \mathbf{U}^T$$

$$((\mathbf{F}^T \mathbf{F})^{-1} \mathbf{F}^T) = \begin{pmatrix} & \\ & \mathbf{V} \\ & \end{pmatrix} \begin{pmatrix} 1/\sigma_1 & 0 & 0 & 0 & \cdots \\ 0 & 1/\sigma_2 & 0 & 0 & \cdots \\ 0 & 0 & 1/\sigma_3 & 0 & \cdots \\ 0 & 0 & 0 & 1/\sigma_4 & \cdots \end{pmatrix} \begin{pmatrix} \\ \\ \mathbf{U}^T \\ \end{pmatrix} \quad (5.4)$$

When noise is present Equation 5.3 can be written as:

$$\begin{aligned}\vec{\tilde{\mathbf{S}}} &= ((\mathbf{F}^T \mathbf{F})^{-1} \mathbf{F}^T)(\vec{\mathbf{O}} + \mathbf{n}) \\ \vec{\mathbf{S}} &= ((\mathbf{F}^T \mathbf{F})^{-1} \mathbf{F}^T) \vec{\mathbf{O}} + ((\mathbf{F}^T \mathbf{F})^{-1} \mathbf{F}^T) \mathbf{n}\end{aligned}\quad (5.5)$$

and

$$\mathbf{E} = ((\mathbf{F}^T \mathbf{F})^{-1} \mathbf{F}^T) \mathbf{n}.$$

Where \mathbf{n} is the noise and \mathbf{E} represents the error term due to noise. When one of the singular values σ_r , $r = 1, 2, 3$, or 4 is zero, the measurement matrix \mathbf{F} will not be full ranked and the corresponding inverse term in the central matrix of \mathbf{F}^{-1} i.e. $1/\sigma_r$ is replaced by zero. If a singular value is zero, there are Stokes vectors that will generate d vectors that are indistinguishable from noise or are identically zero. This implies that there will be polarization states that lie in the null space of the \mathbf{F} matrix and cannot be measured. In cases where the ratio of the largest to smallest singular value is large, significant errors in the reconstruction process can occur through the amplification of noise (error term) in Equation 5.5.

The matrices \mathbf{F} and $((\mathbf{F}^T \mathbf{F})^{-1} \mathbf{F}^T)$, generally are referred to as the measurement and synthesis matrix respectively. The measurement matrix condition number has

been used in the literature to quantify the stability of inverting measured data to Stokes parameters. Condition numbers are capable of providing configurations with measurement matrices that do not have zero or small singular values. The condition number κ (κ_2 condition number in this work) is based on the norm (L_2 norm) of a matrix A [46] and is defined as:

$$\kappa(A) = \|A\| * \|A^{-1}\|$$

where $\|\cdot\|$ stands for the norm

$$\|A\| = \max_{x \neq 0} \frac{\|A * x\|}{\|x\|} \quad (matrix \text{ norm})$$

where x is a vector and when A is not a square, A^{-1} is computed through pseudo-inverse. The norm of A measures the largest amount by which any vector is amplified by matrix multiplication. The norm of the identity matrix is 1. The different condition numbers that are used in general are the κ_1 , κ_∞ , and κ_2 condition numbers, which differ in the norms they use: κ_1 uses L_1 norm, κ_∞ uses L_∞ norm, and κ_2 uses L_2 norm. These condition numbers provide different measures of system conditioning. Although the values of κ_1 , κ_∞ , and κ_2 condition numbers are different for a given measurement matrix, they are bounded by the relations [47]:

$$\frac{1}{n} \kappa_1(A) \leq \kappa_1(A) \leq n \kappa_\infty(A),$$

$$\frac{1}{n} \kappa_\infty(A) \leq \kappa_2(A) \leq n \kappa_\infty(A),$$

$$\frac{1}{n^2} \kappa_1(A) \leq \kappa_\infty(A) \leq n^2 \kappa_1(A).$$

where n is the row size or the column size when the measurement matrix is square. In this work the κ_2 condition number or the L_2 condition number (L_2cn or cn) is used and evaluated as the ratio of the largest to the smallest singular value of the measurement matrix. Singular values are evaluated using the singular value decomposition shown in Equation 5.2. A clear relationship between cn and the singular values of the measurement matrix is now established and can be used.

5.3 Choosing pixel sizes, wedge angles and unit cells using condition number as a metric

Many researchers have used condition number as a metric to design optimal polarimeters. Ambirajan and Look [48, 49] derived the optimum rotation angles for a Stokes polarimeter consisting of a quarter-wave plate and a linear polarizer by maximizing the determinant and minimizing the condition number of the system measurement matrix. Azzam [50] showed that the instrument matrix is non-singular and all Stokes vectors can be determined when the input polarization states are linearly independent and lie on the vertices of the maximum volume tetrahedron inscribed inside a Poincare sphere. Twietmeyer and Chipman [51], Smith [53], Savenkov [52] have used condition numbers to design Optimal Mueller matrix polarimeters. Sabtake, et al [54, 55] used condition numbers, singular value decomposition, and related figures of merit to derive an optimal rotating retarder Stokes polarimeter. Tyo [56] used condition numbers for the optimal design of rotating compensator, variable retardance, and rotating analyzer Stokes vector polarimeters. Tyo [57] also used condition numbers to find the optimum retardances for an imaging variable retardance polarimeter that equalized the noise in the reconstructed Stokes parameter images. DeMartino,

et al. [58, 59] and Garcia-Caurel, et al. [60] used condition numbers for the design of spectroscopic polarimeters using photo elastic modulators and liquid crystal variable retarders.

For a conventional imaging polarimeter the measurement matrix is made of constants and terms that have a functional dependence on the parameters of the retarders and polarizers in the assembly. Most work involving design of optimal polarimeters in the past has been focused on deriving the optimal retardance, retarder, or polarizer orientation that minimizes the condition matrix of the measurement matrix. The choice of pixel size in the detector of a conventional imaging polarimeter is not a concern as long as the pixels capture the highest spatial frequency in the image of the scene. The highest possible frequency in the scene is set by the pupil diameter and wavelength. However in ISIP, the measurement matrix is made from the pixel measurements of calibration fringes. The pixels must Nyquist sample the calibration fringes that modulate the scene as well as the scene.

Minimizing the condition number reduces the noise sensitivity of the Stokes estimation problem. The task of making the measurement matrix least singular by minimizing the condition number can be seen as an optimization problem. Either the pixel size or wedge angle is altered (while fixing the other) and the resultant change in the condition number of the measurement matrix is evaluated. In this work, the detector parameters - array size & number of pixels, and physical dimensions are maintained constant while the wedge angle is changed in small increments. Measurement matrices for each wedge angle increment are constructed from corresponding F_1 , F_2 , and F_3 unit cell matrices using the slide procedure (refer to Section 4.2). Consequently an entire array of condition numbers for each wedge angle increment is generated as the unit cell is slid over the entire detector. The statistical measures (mean and standard deviation) of the resulting condition number array are computed

over the array for each wedge angle and stored.

From Equation 4.3, atleast 3 measurements are required to uniquely estimate S_1, S_2 and S_3 . The smallest square unit cell is 2 X 2 pixels and the analysis is started with this unit cell size. The mean and standard deviation of each condition number array is evaluated and plotted as a function of the wedge angle (Figure 5.4).

It can be seen that mean and standard deviation of condition numbers are large and there is not a wedge angle that minimizes the condition number everywhere on the array. Analysis of the condition number array corresponding to the wedge angle of 1.105 reveals that the maximum condition number in the array is 12027.655, and mean condition number is 111.838. Figure 5.5 and Figure 5.6 show regions of high condition number in the condition number array through white lines and peaks respectively. It is seen that these regions are periodic in nature and the measurement matrix \mathbf{F} corresponding to the maximum condition number is given by :

$$\mathbf{F} = \begin{bmatrix} 0.5 & 0.217402 & -0.410956 & 0.0110547 \\ 0.5 & 0.158836 & -0.360095 & 0.172931 \\ 0.5 & -0.200860 & -0.152217 & -0.348243 \\ 0.5 & -0.238476 & -0.398790 & -0.0191638 \end{bmatrix}$$

A singular value decomposition of this \mathbf{F} matrix according to Equation 5.2 yields the \mathbf{U} , σ , and \mathbf{V}^T matrices as follows :

$$\mathbf{U} = \begin{bmatrix} -0.546426 & 0.706072 & 0.448539 & 0.0411586 \\ -0.448835 & -0.0412970 & -0.546543 & 0.705785 \\ -0.448778 & 0.0408876 & -0.546294 & -0.706038 \\ -0.546411 & -0.705751 & 0.449074 & -0.0410260 \end{bmatrix} \quad (5.6)$$

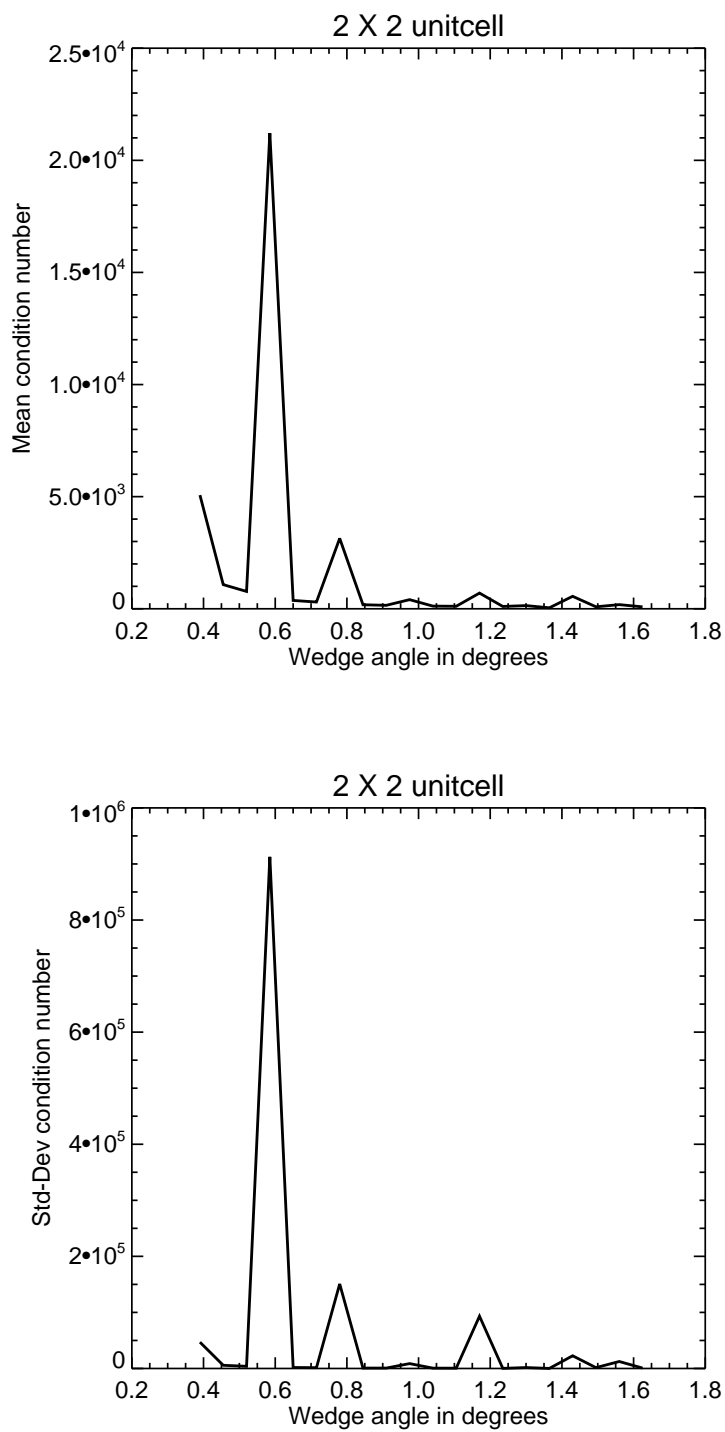


Figure 5.4: Mean and std-dev condition number for a unit cell size 2 X 2.

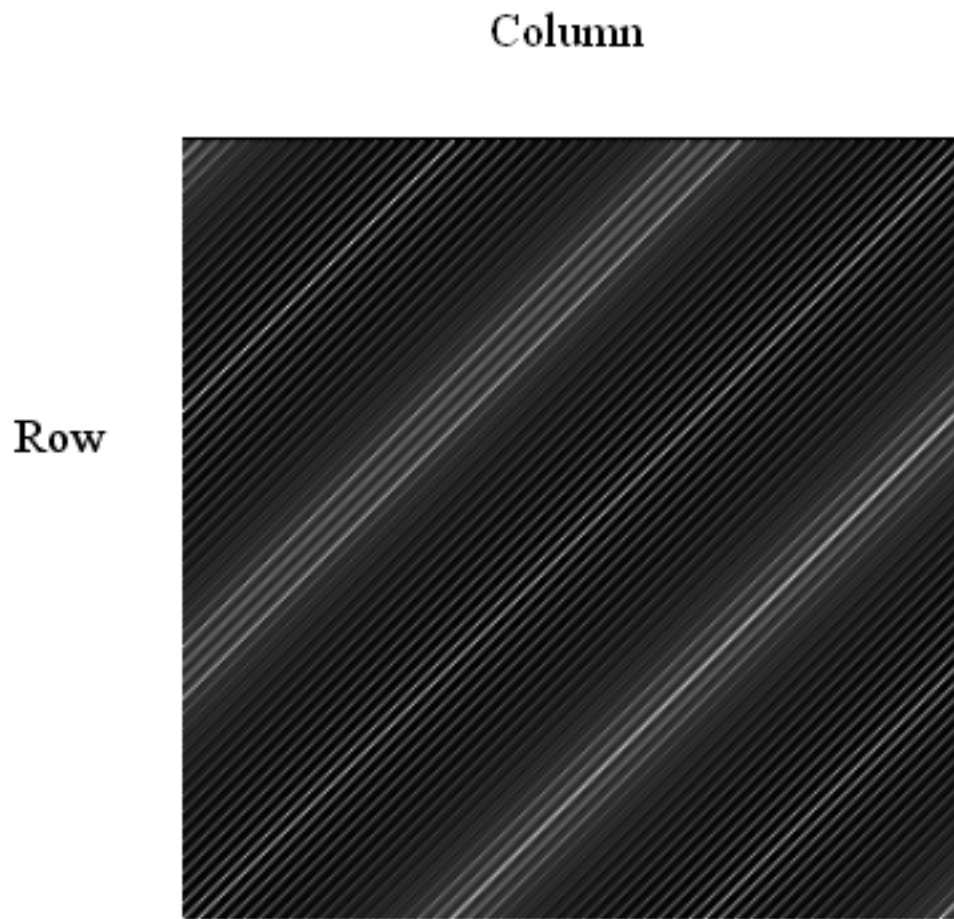


Figure 5.5: Natural log of condition number array surface (2D) for the 2 X 2 unit cell at Nyquist sampling.

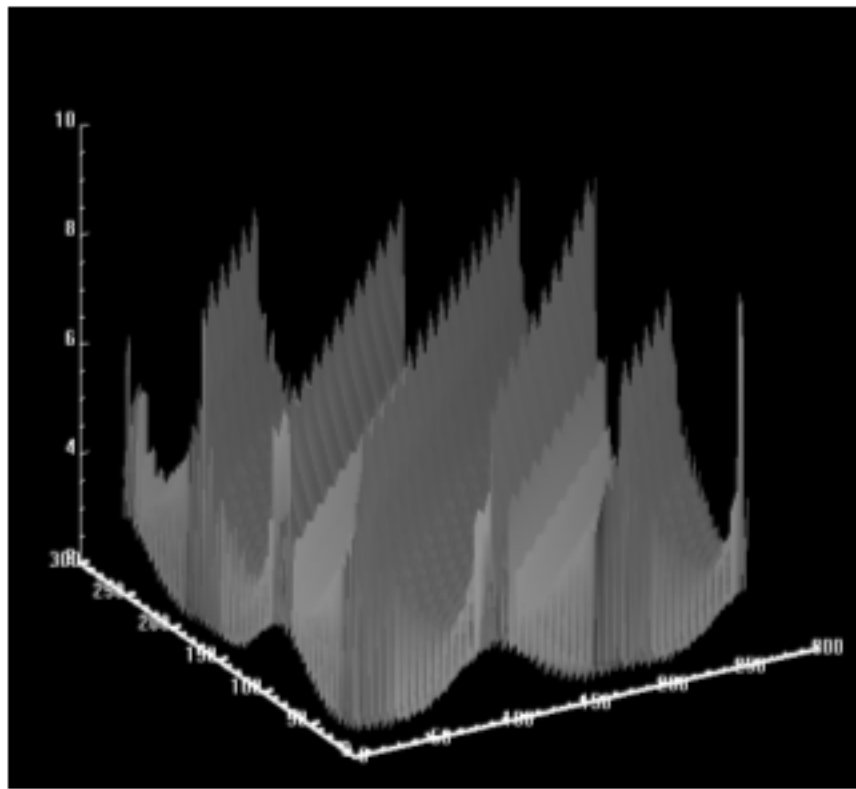


Figure 5.6: Natural log of condition number array surface (3D) for the 2 X 2 unit cell at Nyquist sampling.

$$\sigma = \begin{bmatrix} 1.23341 & 0 & 0 & 0 \\ 0 & 0.000102547 & 0 & 0 \\ 0 & 0 & 0.240795 & 0 \\ 0 & 0 & 0 & 0.472081 \end{bmatrix} \quad (5.7)$$

$$\mathbf{V}^T = \begin{bmatrix} -0.806892 & 0.217244 & 0.545153 & 0.0673716 \\ -0.429649 & 0.303754 & -0.696725 & -0.487555 \\ -0.405373 & -0.754537 & -0.346576 & 0.382403 \\ -0.000127816 & 0.539641 & -0.311878 & 0.781997 \end{bmatrix} \quad (5.8)$$

Looking at the singular values (along the diagonal) in σ matrix (Equation 5.7) it can be seen the second singular value is negligible compared to the largest condition number and can be approximated to zero. Hence the rank of the measurement matrix is effectively only 3. From a conventional Stokes polarimeter perspective, this measurement matrix is not capable of measuring the input Stokes vector which lies in the direction of the row vector of \mathbf{V}^T corresponding to the 0.000102547 singular value. In the case of ISIP there will be an input Stokes vector whose fringe pattern will not be observable by the system. Hence the polarization state (Stokes vector) cannot be measured in that particular unit cell. In order to show this, a calibration fringe pattern for the input Stokes vector

$$\vec{\mathbf{S}} = \begin{bmatrix} 1 \\ -0.33638462 \\ 0.77157029 \\ 0.53993025 \end{bmatrix}$$

is created with the Nyquist sampling wedge angle 1.105. The 2 X 2 matrix of the

calibration fringe output at the location corresponding to the maximum condition number is found to be :

$$\begin{bmatrix} 0.262018 & 0.262103 \\ 0.262093 & 0.262178 \end{bmatrix}.$$

The same procedure when repeated for the orthogonal input Stokes vector

$$\vec{\mathbf{S}} = \begin{bmatrix} 1 \\ 0.33638462 \\ -0.77157029 \\ -0.53993025 \end{bmatrix}$$

yields the following 2 X 2 calibration fringe matrix:

$$\begin{bmatrix} 0.73798230 & 0.73789747 \\ 0.73790679 & 0.73782198 \end{bmatrix}$$

The intensity variation in the unit cells for the input polarization states considered is of the order of 10^{-5} . Detector pixels are normally capable of 8-bit, 12-bit, or 16-bit digitized outputs. Hence a pixel can only detect intensity variations of the order of $\simeq 10^{-4}$ (assuming a 12-bit output). Thus the two polarization states (Stokes vectors) would effectively yield the same measurement on the order of 10^{-4} , constant energy in the unit cell. In practical experiments where detectors are used, the small variations in the fringe modulation in the unit cells would most likely not be detected under the presence of noise and stable reconstruction of these orthogonal polarization states

$$\text{Angle(degrees)} = \cos^{-1}\left(\frac{(\text{row } i) \cdot (\text{row } j)}{|\text{row } i| |\text{row } j|}\right) \text{ where } i \text{ and } j=1,2,3 \text{ or } 4 \text{ with } i \neq j.$$

	row 1	row 2	row 3	row 4
row 1	0	35.78 degrees	38.52 degrees	3.26 degrees
row 2	35.78 degrees	0	60.74 degrees	38.51 degrees
row 3	38.52 degrees	60.74 degrees	0	35.8 degrees
row 4	3.26 degrees	38.51 degrees	35.8 degrees	0

Table 5.1: Angle between the rows of the measurement matrix corresponding to the largest condition number: 12027.655 (2 X 2 unit cell case).

would not be possible.

A further analysis on the angles of the normalized vectors of each row of the measurement matrix with respect to others are shown in Table 5.1. It is seen that the angle between normalized vectors of rows 1 and 4 is 3.26 degrees, which means that these rows are highly dependent. Rows 1 and 4 of the measurement matrix are obtained from first and fourth pixel energies of the calibration fringe unit cells. A close look (Table 5.2) reveals that there is not much variation in intensity along the diagonal in each of these calibration unit cells. It would be difficult to tell these states apart by looking at pixels 1 and 4.

A unit cell, irrespective of size, would have a phase relative to the fringe pattern at its boundary when the number of pixels either along the row or column is not an integer multiple of the fringe periods. A 2 X 2 unit cell is capable of measuring only a single spatial frequency along its row and column. Any spatial period smaller or greater than 2 pixels is invisible to the 2 X 2 unit cell. When the spatial period is smaller than 2 pixels Nyquist sampling criteria is violated and a spatial period greater than 2 pixels causes the fringes to have a phase relative to the unit cell boundary. With unit cells greater than 2 x 2 when the spatial period becomes lesser than the number of pixels along the row or column reconstructions may still be possible.

Unit cell (Horz calibration fringe) =	Pixel 1	Pixel 2
	0.28599	0.658834
	Pixel 3	Pixel 4
	0.299141	0.261524
Unit cell (45 calibration fringe) =	Pixel 1	Pixel 2
	0.08904	0.139905
	Pixel 3	Pixel 4
	0.347784	0.101210
Unit cell (RHC calibration fringe) =	Pixel 1	Pixel 2
	0.511051	0.672935
	Pixel 3	Pixel 4
	0.15756	0.480835

Table 5.2: Unit cells of the calibration fringes corresponding to the largest condition number: 12027.655

Unit cell (Horz calibration fringe) =	Pixel 1	Pixel 2
	0.432254	0.489894
	Pixel 3	Pixel 4
	0.140293	0.177919
Unit cell (45 calibration fringe) =	Pixel 1	Pixel 2
	0.0475029.	0.424524
	Pixel 3	Pixel 4
	0.280777	0.194344.
Unit cell (RHC calibration fringe) =	Pixel 1	Pixel 2
	0.513325.	0.0880955
	Pixel 3	Pixel 4
	0.652929	0.388828

Table 5.3: Unit cells of the calibration fringes corresponding to the condition number: 10.6

	Pixel 1	Pixel 2
Unit cell (Horz calibration fringe) =	0.545471	0.316935
	Pixel 3	Pixel 4
	0.554863	0.0791612
	Pixel 1	Pixel 2
Unit cell (45 calibration fringe) =	0.151905	0.0735146
	Pixel 3	Pixel 4
	0.599612	0.421125
	Pixel 1	Pixel 2
Unit cell (RHC calibration fringe) =	0.242824	0.514003
	Pixel 3	Pixel 4
	0.0943990	0.577780

Table 5.4: Unit cells of the calibration fringes corresponding to the condition number: 66.46

The phasing of the unit cell (of any size) with respect to the calibration fringes causes a periodic variation in condition number over the detector array. The 2 X 2 unit cell reconstructions are sensitive to this phasing than unit cells of higher dimensions. The phasing of the 2 X 2 unit cells with respect to the calibration fringes creates regions in the detector image where adjacent pixel intensity variations are small. The overlap of such regions in all calibration fringe images- horizontal, 45 and RHC, with minimal intensity variation in the same direction produces measurement matrices with high condition number. Since the calibration fringes are periodic over the detector array, these regions will also be periodic as shown in Figure 5.5. However, for a monochromatic illumination for which the ISIP is designed there are 2 x 2 regions in the detector with condition numbers 10.6 and 66.46. The unit cells of the calibration fringes corresponding to these condition numbers are shown in Figures 5.3 and 5.4. In these regions the Stokes parameters can be estimated with a 12 bit detector.

If the 2 X 2 unit cell is exactly one calibration fringe period in both x and y

dimensions the condition number would be constant over the entire detector array. The value of the constant condition number would depend on the starting phase of the fringes and can be varied in every unit cell at the same time by shifting the fringes across the array. The condition number can be controlled by a shift achieved by the lateral movement of the detector or the BCA. Even a small tilt of the camera or BCA can be used to achieve this as long as the camera plane remained in focus. However, an accidental misalignment which is common in practical experiments can drive the condition number to a high value leading to the reconstructions being unstable. Hence a sensor alignment with the fringes is hard to achieve and maintain in a practical environment.

The calibration fringes of the ISIP have different periods in the x and y dimensions which implies that the 2×2 unit cell cannot be made exactly one fringe period in both directions. Hence the phasing problem will always exist. Moreover, when the ISIP is used in broad band illumination the fringe period is bound to change due to the dispersion effects of the BCA uniaxial crystals. Consequently the discussion of fringe period becomes meaningless in a broad band illumination situation. All the above factors suggests the 2×2 unit cell reconstructions can be sensitive to alignment, fabrication errors and bandpass operations making its application impractical though mathematically correct.

The utility of 2×2 unit cell reconstruction is explored in other sampling scenarios such as oversampled calibration fringes. Various wedge angle configurations that provide oversampling with the existing detector dimensions are used and the condition number array of each case is analyzed. The statistics of the condition number array for each of the wedge angle configuration are computed and tabulated (Table 5.6). At high wedge angles, the fringe periods are smaller and pixels undersample. At lower angles where the pixels are over sampling, the mean and standard deviation of the

Wedge angle (degrees)	Mean cn	Std-dev of cn	Max cn	Number of cn $> 10^4$
0.39	5068	46896	1053022	1155
0.455	1076	5620	88360	1170
0.52	772	3880	53524	1078
0.585	21212	912762	1.5×10^8	3281
0.65	372	1677	64171	524
0.715	301	1425	30886	283
0.78	3140	150756	19161688	423
0.845	178	702	8777	0
0.91	155	678	14056	113
0.975	407	8660	551306	84
1.04	119	571	11944	100

Table 5.6: Statistics on the condition number arrays in oversampled cases (2 X 2 unit cell).

condition number increase. This is due to the fact that the 2 X 2 unit cell can see only one frequency in each dimension and the phase of the fringes becomes increasingly important. At wedge angle of 0.585 which is almost half the Nyquist sampling rate, 2 pixels would see half a period and would have the same intensity when the fringes are in phase. Consequently there would be regions of high condition numbers which is reflected through the maximum, mean and standard deviation values in Table 5.6. Based on the presence of high condition numbers and previous analysis at Nyquist sampling, it may be inferred that there are regions on the detector where certain polarization states cannot be distinguished from others. In addition noise effects will be dominant and reconstructions with a 2 X 2 unit cell are not practical. The Stokes estimates with 2 X 2 unit cells are unstable due to its sensitivity to the presence of noise and round off errors. New condition number arrays are constructed using 3 X 3 unit cells with wedge angles maintained the same as in the 2 X 2 unit cell case and the analysis is repeated.

Figure 5.7 shows the variations of the mean and standard deviation condition num-

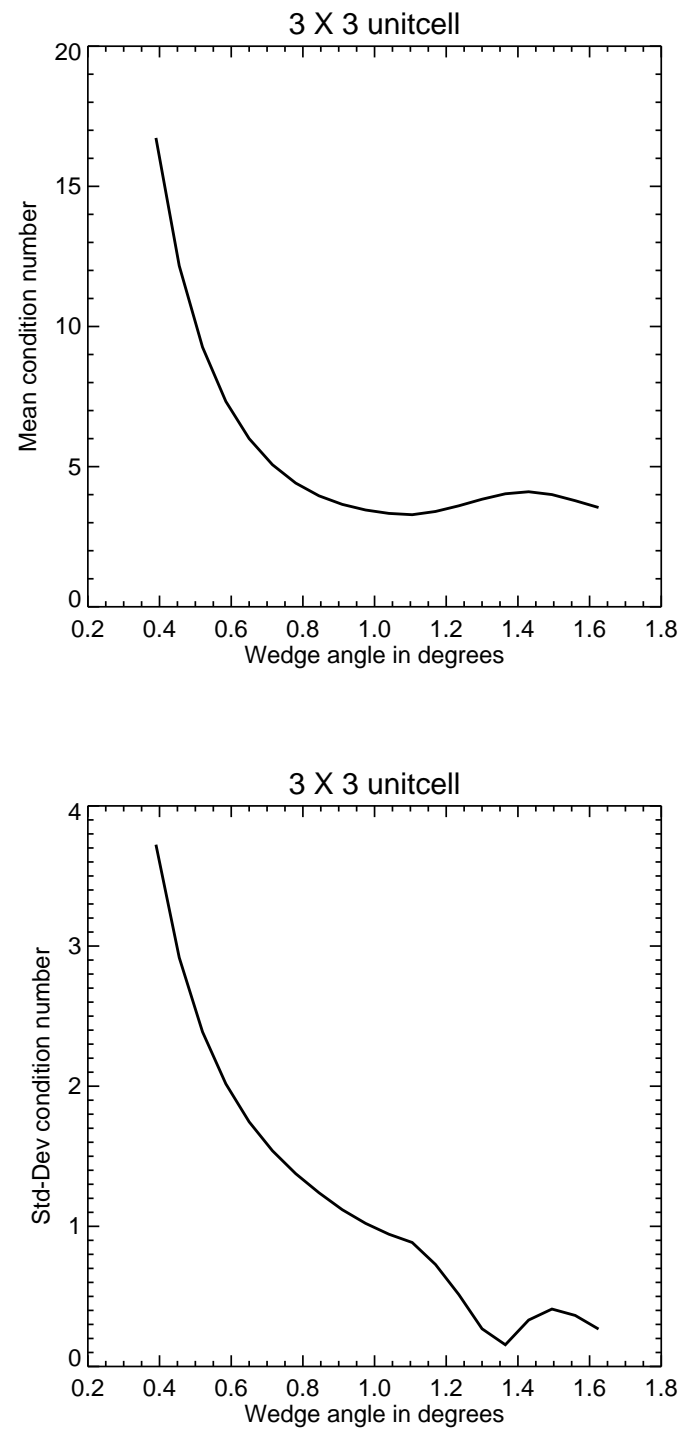


Figure 5.7: Metrics of condition number arrays for a unit cell size 3 X 3.

ber with increasing wedge angle. It can be seen that the minimum mean condition number 3.2846778 occurs at wedge angle: 1.105 degrees, when pixels Nyquist sample the calibration fringes. This is an important result as it indicates that the choice of pixel size that Nyquist sampling the calibration fringes and a unit cell size of 3 X 3 makes the reconstructor “well-conditioned” or less sensitive to the presence of noise in measurements which is quite often the case when imaging scenes of low illumination levels. The mean condition number curve in Figure 5.7 decreases with increase in wedge angle beyond 1.4 degrees. This is due to the aliasing effects which cause high frequency calibration fringe pattern to look like a lower frequency pattern. Though the condition number for this aliased fringe pattern seems low, the bias introduced into the reconstruction procedure causes significant errors in estimating the Stokes components. The issues of bias, variance, and root mean square error is addressed in Chapter 6.

The configuration - pixel size: 19.42 micron, wedge angle: 1.105 and a unit cell size: 3 X 3, can be considered to be optimal (for the wavelength (600nm) and the aperture size(5mm X 5mm)) when the signal levels are considerably higher than the noise levels. However, larger unit cells ($> 3 \times 3$) are needed for Stokes reconstruction when noise is significant as it provides more measurements. In addition, with larger unit cells, the slide reconstructor provides more estimations for the same Stokes component at most pixels. A higher averaging is possible as a result, reducing the noise in the reconstructed Stokes components. With larger unit cells the measurement matrix \mathbf{F} gets more rectangular (more rows added, number of columns fixed at 4) while the condition number may vary. This variation is analyzed from condition number arrays constructed for each larger unit cell case with the wedge angle maintained at 1.105 degrees. Figure 5.8 shows the variation of mean and standard deviations of condition number in the arrays as a function of number of pixels in the unit cell. It

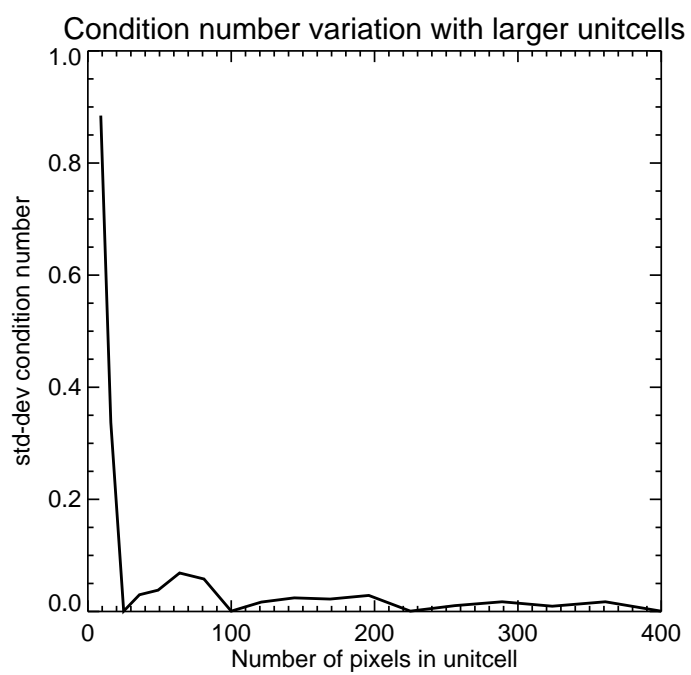
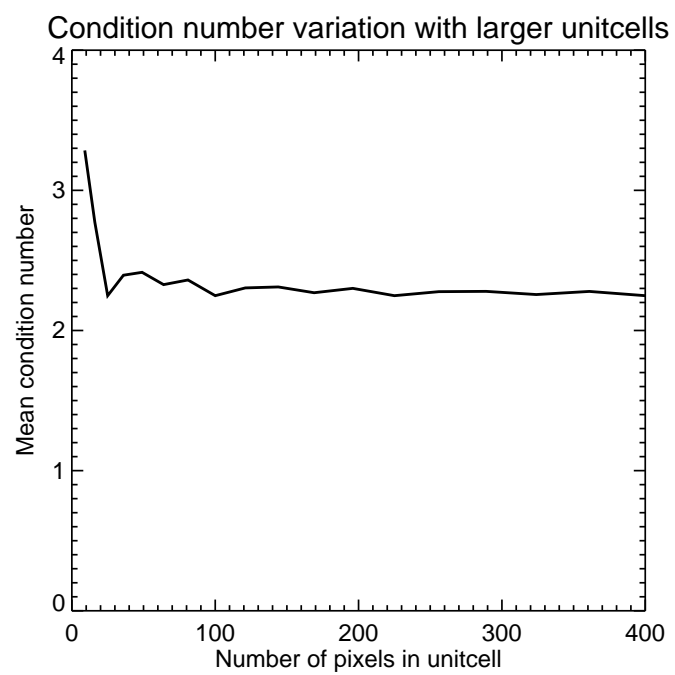


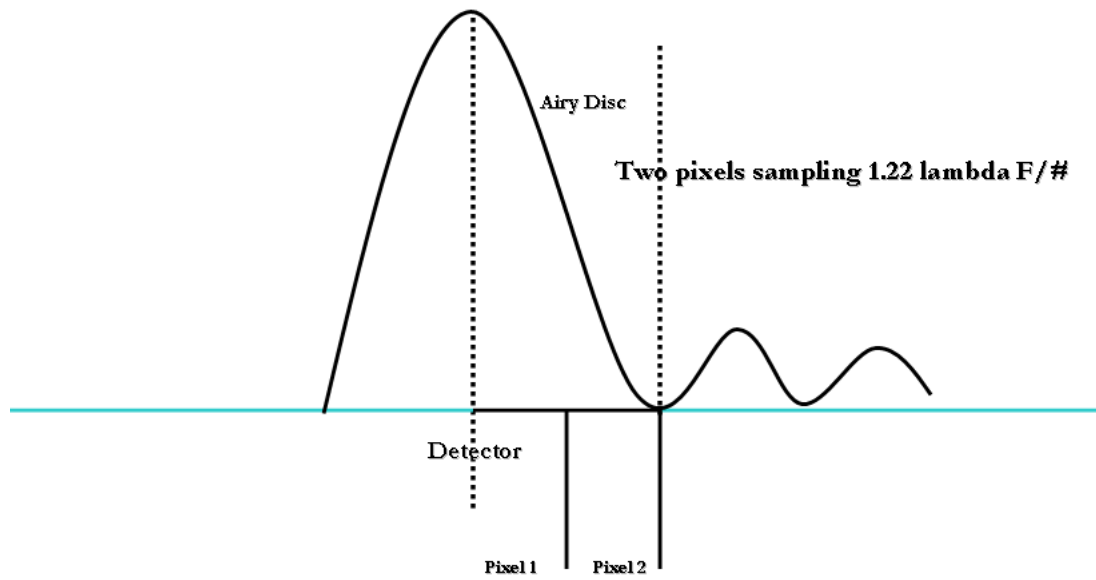
Figure 5.8: Condition numbers of larger unit cells.

can be seen that the mean condition number varies little beyond a 4 X 4 unit cell (16 pixels) and the values of the mean condition number are in agreement with the limit ($\sqrt{N-1} = \sqrt{3} = 1.732$, where N is the number of Stokes components estimated) proposed by Tyo [56]. A low condition number value constant over the detector array indicates that the noise amplification in the reconstruction process is minimum. The same holds true for unit cells greater than 3 X 3. Condition numbers do not reflect the effects of averaging or increased throughput (scenes with high illumination levels). These effects should be taken into consideration when the choice of a unit cell size is made based on condition numbers.

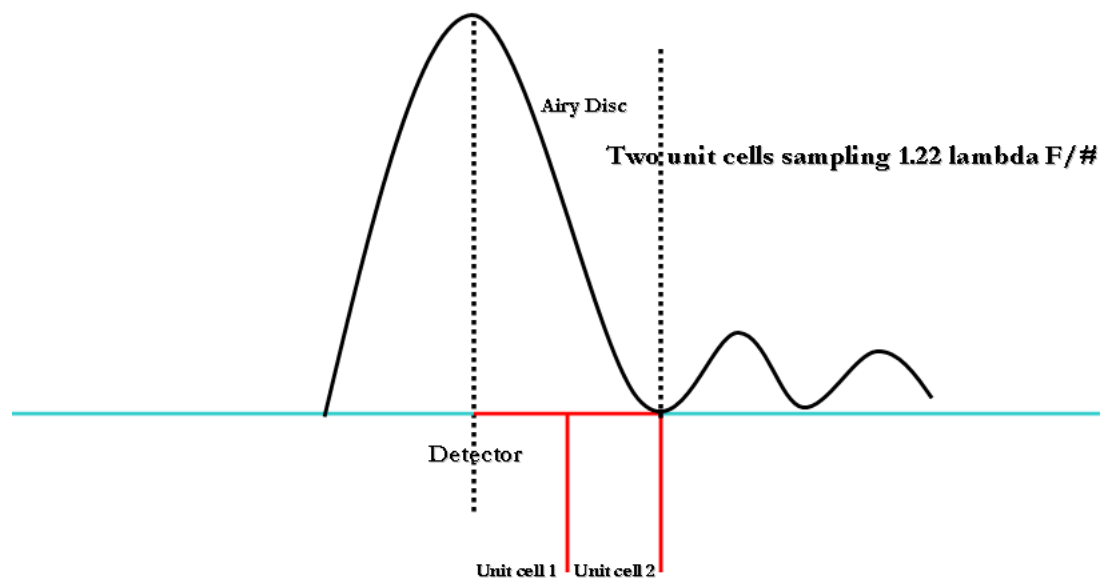
5.4 Nyquist Sampling the PSF

The imaging systems used with an ISIP that map the SOP of the input light from an object or a scene needs to be analyzed from a PSF perspective. There are two main reasons for an analysis based on this perspective. First, ISIPs encode polarization information of the light from the scene in the form of intensity fringes. A serious problem is likely to occur if the image of the scene has intensity variations similar to the calibration fringes. The reconstruction algorithm may generate false polarization signals in such situations as intensity modulations from the polarization signal and scene variations cannot be differentiated. As a result, an imaging system with a PSF that maps the scene variations slower than the calibration fringe variations at the detector plane is required for use with the ISIP.

A second reason for a PSF analysis is that the reconstructor algorithm developed in Section 4.2 is based on the assumption that the polarization and intensity of the incident light is uniform over a unit cell and the size of the unit cell is smaller than the polarization domain (Section 4.1). The polarization of regions in the image whose scale is smaller than the size of a unit cell cannot be resolved. PSFs play an important



(a) Nyquist sampling the PSF with pixels.



(b) Nyquist sampling the PSF with unit cells.

Figure 5.9: Nyquist sampling the PSF.



(a) True image (b) Fringe modulated image

Figure 5.10: Point source images: True image and Fringe modulated image.



S0 image

S1 image

S2 image

S3 image

Figure 5.11: Reconstructed Stokes images of the point source.

role in determining the size of these polarization domains as a PSF relates the object intensity distribution and image intensity distribution through a convolution. The PSF chosen will be required to produce an image such that the measurement of SOP of the smallest object (a point source) is possible.

Both requirements can be met by placing a limit on the size of unit cell used in the reconstruction procedure with respect to the PSF. This limit is the Nyquist sampling of the PSF - the physical length (either along the row or the column) of two unit cells should be less than or equal to PSF half width, $1.22 \times \lambda \times F/\#$ and such a limit is most likely to reduce the reconstruction errors in the Stokes images. In conventional imaging systems that record only intensity variations from the scene, the Nyquist sampling requirement is shown in Figure 5.9a. This requirement ensures the

slow variations of the image with respect to the pixels. The size of the pixels ensure all spatial frequencies out to the band set by the aperture are adequately sampled. However, in case of the ISIP the modified Nyquist sampling requirement is shown in Figure 5.9b. Two unit cells Nyquist sample the PSF and the pixels forming the unit cells Nyquist sample the calibration fringes as shown in section 5.3. The requirement of two unit cells per $1.22 \times \lambda \times F/\#$ ensures that the scene variations are not faster than the calibration fringe variations.

In order to show the effect of unit cell size Nyquist sampling the PSF, a point source equally polarized in S_1, S_2 and S_3 is imaged through a telescope model with PSF half width ($1.22 \times \lambda \times F/\#$) of 15 pixels - measured from the discretized PSF image from the detector. Stokes images are reconstructed with unit cells of increasing dimensions. The size of the pixels used in the detector is 19.42 microns which makes the PSF half width 210 microns. The size of the unit cells are increased from an initial dimension of 3 X 3 to a final dimension of 20 X 20 by integer increments. Figure 5.10 shows the true image (without crystal assembly) and fringe modulated image (with crystal assembly) obtained from a telescope with PSF of half width $1.22 \times \lambda \times F/\# = 15$ pixels (15×19.42 micron = 291 micron). And Figure 5.11 shows Stokes images reconstructed from the fringe modulated image using a 3 X 3 unit cell.

The Stokes images reconstructed in each PSF case are then used to form the Error Metric (EM):

$$EM = \sum_{S_0, S_1, S_2, S_3} Avg\left(\frac{abs(TSI - RSI)}{TSI}\right) \quad (5.9)$$

Where TSI is the True Stokes Image and RSI is the Reconstructed Stokes Image. The Error Metric is evaluated at regions where the value of the PSF is greater than 1% of its peak value. In Equation 5.9 both true image and reconstructed images are

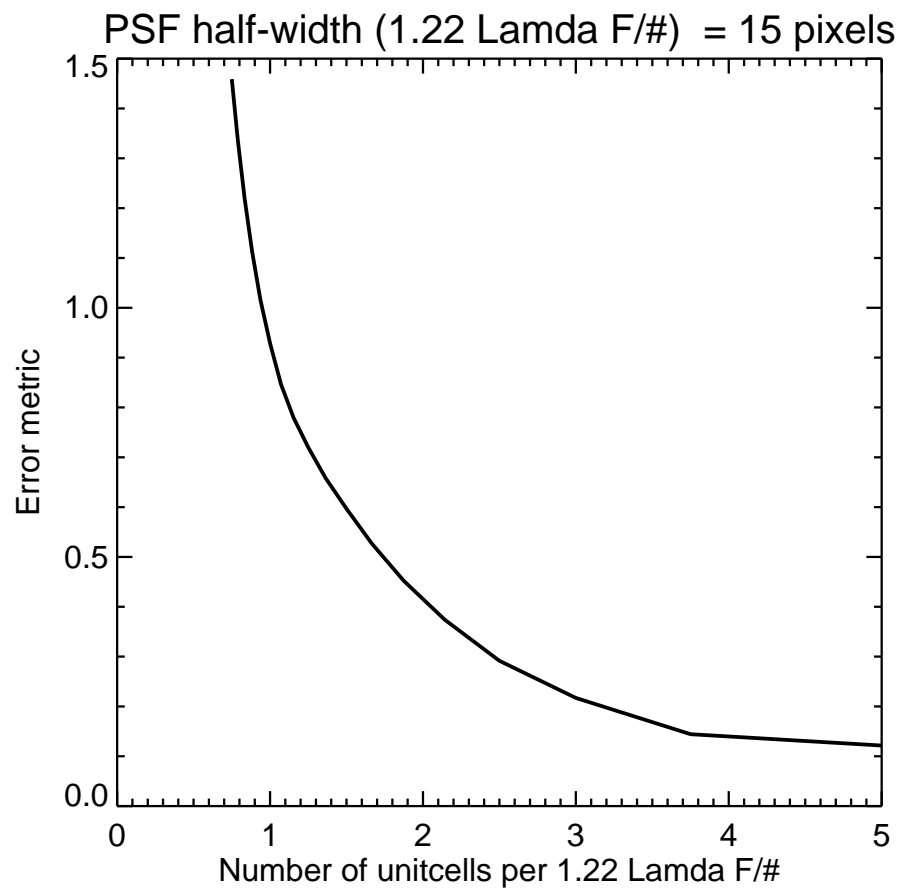
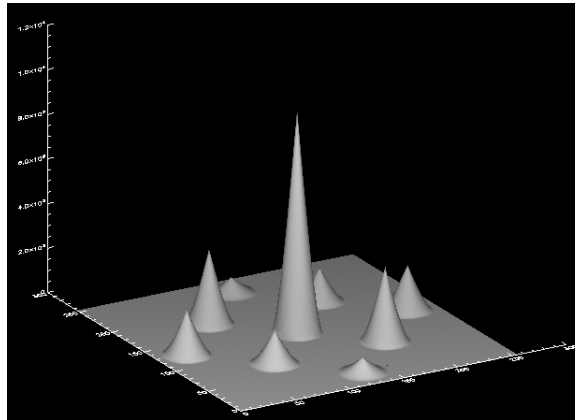


Figure 5.12: Error metric as a function of number of unit cells sampling $1.22 \text{ } \lambda F/\#$

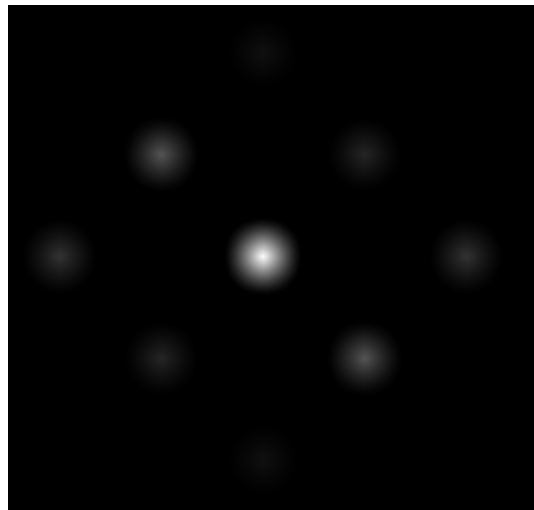
functions of S_0, S_1, S_2 , and S_3 . The error metric is evaluated each time the Stokes images with a different unit cell size are reconstructed. The evaluated error metric is plotted as a function of the number of unit cells per $1.22 \times \lambda \times F/\#$ (Figure 5.12). It is seen that when the unit cells sample the PSF at rates lesser than Nyquist the Error Metric curve becomes exponential. Hence, to keep the reconstruction errors to a minimum, it is important that the unit cells sample PSF at rates greater than or equal to Nyquist. The Nyquist sampling requirement of the PSF is not limited to ISIP class of polarimeters, this limit also applies to polarimeters that use micro-grid polarizers at the focal plane detector arrays.

A similar analysis of the PSF is done in the Fourier domain for the same point source imaging example. In section 3.1 of Chapter 3, the analytical form of the fringe modulated image in the Fourier representation is derived. When the object imaged through the BCA is a flat field, the magnitude of the Fourier transform of the fringe modulated image based on Equation 3.1 is identical to one of the patterns in Figure 5.1 where the spread of the side lobes are minimal. However, when the object imaged is of smaller size like a point source, the image, unlike the flat field, does not fill the detector field. This causes the spread of the central and side lobes in the Fourier domain to increase. The spread of the central and side lobes can be noticed in the magnitude image (Figure 5.13) of the Fourier transform of a point source.

The size of the entrance pupil of the fore-optics and pixels determine the size of the PSF in the discretized image from the detector. With the pixel size chosen to Nyquist sample the calibration fringes, the size of the PSF depends on the choice of the fore optics. An increase in the size of the entrance pupil from any initial value decreases the PSF half-width ($1.22 \times \lambda \times F/\#$) providing better spatial resolution. However, this decrease in PSF width is accompanied by increasing spread of the central and side lobes in the Fourier domain resulting in aliasing as shown in Figure 5.14. As

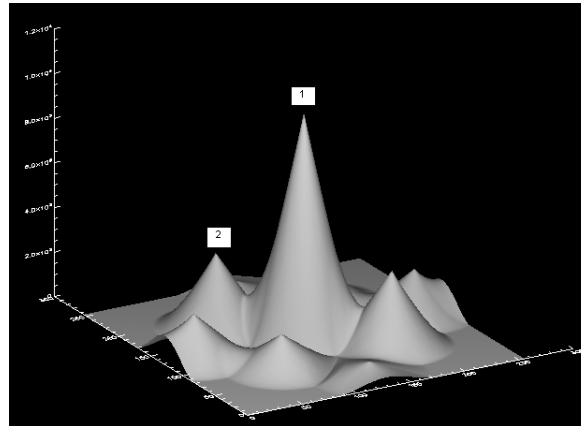


(a) A three dimensional perspective.

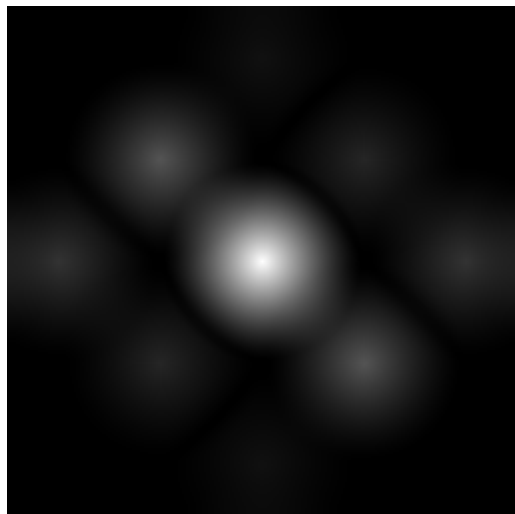


(b) A two dimensional perspective.

Figure 5.13: Magnitude of the Fourier transform of a point source (PSF width - $1.22 \times \lambda \times F/\# = 16$ pixels).



(a) A three dimensional perspective.



(b) A two dimensional perspective.

Figure 5.14: Magnitude of the Fourier transform of a point source (PSF width - $1.22 \times \lambda \times F/\# = 7$ pixels).

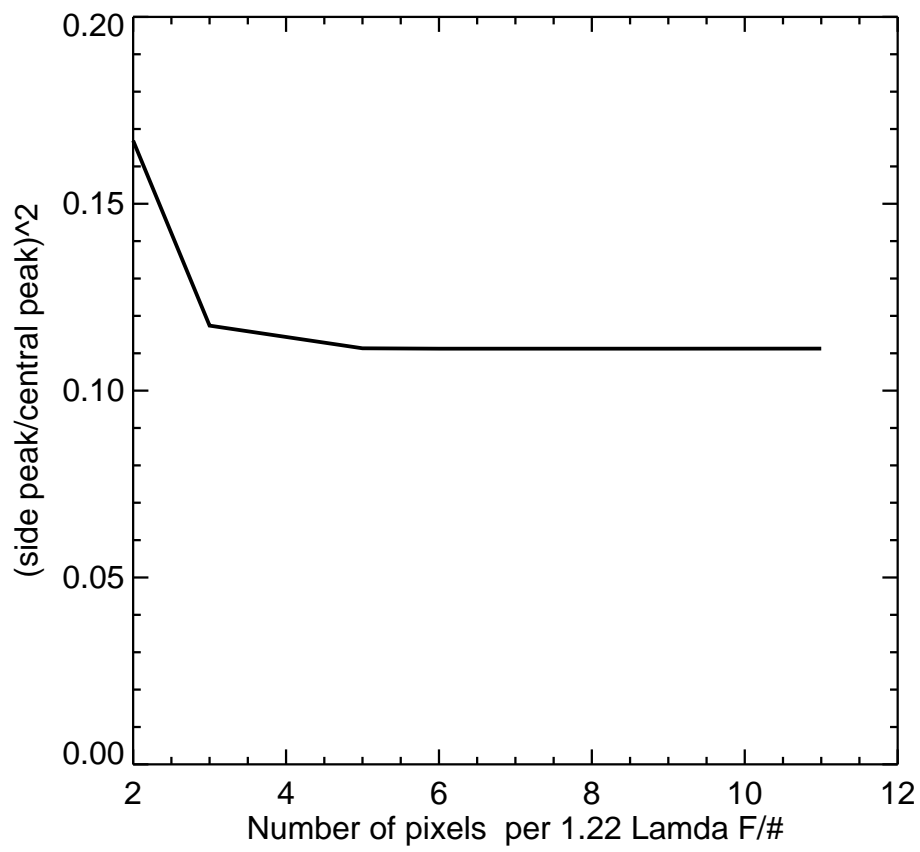


Figure 5.15: Effect of varying PSFs in the Fourier domain.

the PSF shrinks the peaks of the side lobes become harder to detect resulting in the inability of the reconstruction of Stokes images. The ratio of the side lobe peak (2) to the central peak (1) in Figure 5.14 is calculated from Fourier transforms of fringe modulated images obtained with PSFs of decreasing half-widths. In Figure 5.15 the variation of this ratio as function of the number of pixels per $1.22 \times \lambda \times F/\#$ of the PSF is shown. It is inferred that the side lobe peaks are not affected by the expanding central lobe as long as the PSF half-width is greater than or equal to 6 pixels. Any PSF half-width less than 4 pixels makes the side lobe peak indistinguishable from the expanding central lobe. The 6 pixel limit for a constant ratio between the side lobe and central lobe is in agreement with the minimum required unit cell (3 X 3) and proposed PSF Nyquist sampling requirement (Figure 5.9b). The concept of Nyquist sampling the PSF with regions over which the polarization will be assumed constant applies to both Fourier and spatial reconstructors.

CHAPTER 6

BIAS-VARIANCE TRADEOFF AND SENSITIVITY ANALYSIS

In problems involving estimation of parameters, an introduction of a bias may actually provide an improvement compared to unbiased estimator. The performance of an estimator \tilde{x} can be expressed by its Mean Squared Error (MSE) and is generally written as:

$$MSE = \langle (x - \tilde{x})^2 \rangle$$

$$MSE = \langle x^2 - 2x\tilde{x} + \tilde{x}^2 - \langle \tilde{x} \rangle^2 + \langle \tilde{x} \rangle^2 \rangle$$

$$MSE = x^2 - 2x \langle \tilde{x} \rangle + \langle \tilde{x} \rangle^2 + \langle \tilde{x}^2 \rangle - \langle \tilde{x} \rangle^2$$

$$MSE = (x - \langle \tilde{x} \rangle)^2 + \langle \tilde{x}^2 \rangle - \langle \tilde{x} \rangle^2$$

$$MSE = Bias(\tilde{x}) + Variance(\tilde{x}) \quad (6.1)$$

$$Bias(\tilde{x}) = (x - \langle \tilde{x} \rangle)^2 \quad (6.2)$$

$$Variance(\tilde{x}) = \langle \tilde{x}^2 \rangle - \langle \tilde{x} \rangle^2 \quad (6.3)$$

, where x and \tilde{x} represent the true value and estimated value respectively. The lack of bias does not imply a low MSE and often, a minimum value for the MSE is achieved when a proper tradeoff is found between the bias of the estimator and its variance.

The slide reconstruction is an estimator for the Stokes parameters S_0, S_1, S_2 , and S_3 from the pixel measurements of the detector array. For the purposes of slide reconstruction, \tilde{x} and x are the estimated Stokes image and true image corresponding to the estimated Stokes image respectively. Hence \tilde{x} and x are replaced by \tilde{S}_i and S_i where $i = 1, 2$, or 3 . The assumption of the slide reconstructor estimation is that the intensity and polarization of the light over a unit cell varies slowly. It is established in Chapter 5 that a 2×2 unit cell is not suitable for reconstruction and the minimum required unit cell size is 3×3 . Choice of unit cells with dimensions greater than 3×3 introduces higher bias when the unit cells sample the PSF at rates less than Nyquist. However the increased number of pixels measurements in the unit cell reduces the variance in Equation 6.1 when noise is present. The summation of the higher bias and reduced variance with a higher dimension ($> 3 \times 3$) unit cell can produce a lower MSE compared to a 3×3 unit cell case depending on the brightness of the object being imaged and its associated noise levels at the detector. The Mean Square Error (*MSE*), in Equation 6.1 compares the Stokes estimations obtained with unit cells of increasing dimensions and is written as follows:

$$MSE = Bias(\tilde{S}_i) + Var(\tilde{S}_i)$$

Where *Var* is the variance and S_i is the true value of the Stokes parameter with $i = 0, 1, 2$, and 3 .

For the case of the slide reconstructor, MSE is a two dimensional array computed for each of the Stokes estimations $\tilde{S}_0, \tilde{S}_1, \tilde{S}_2$, and \tilde{S}_3 . A scalar value representing the

MSE for each of the Stokes estimations can be calculated using a pixel average:

$$< MSE >_{\mathbf{P}} = \frac{\sum_{n=1}^N MSE}{N}$$

$$= PAB + PAV$$

where PAB is the Pixel Averaged Bias and PAV is the Pixel Averaged Variance.

$$PAB = \frac{\sum_{n=1}^N Bias}{N}$$

$$PAV = \frac{\sum_{n=1}^N Var}{N}.$$

The symbol $<>_{\mathbf{P}}$ indicates a pixel average within the same image, n represents the pixel number and N is the total number of pixels. In this work, $<>_{\mathbf{P}}$ is evaluated for regions in the estimated Stokes images that correspond to an energy greater than or equal to 1% of the peak energy in the true image. The detector image obtained without the BCA is the true image. The use of the term MSE will refer to the pixel averaged quantity $< MSE >_{\mathbf{P}}$ and the explicit use of the averaging operator is avoided in rest of this work.

The metric MSE is also used to study the bias-variance tradeoff issues when the light energy from the scene or object is distributed across a wide range of wavelengths. Under this circumstance the BCA produces a fringe pattern with a visibility that is periodically attenuated due to wavelength dispersion. In other words, it's the angular dispersion of the fringes as a function of wavelength that causes a spatial beat

phenomena in visibility. A bandpass filter is required to limit the band of wavelength over which energy is collected. A filter of bandwidth 50nm would increase the light energy collected compared to 10nm filter assuming that the energy at each nm of the incident light is the same. However, the modulation of the fringes starts decreasing at the outer regions of the image and continues inwards as the transmission width of the bandpass filter is increased. The loss of modulation of the fringes causes reconstruction errors in the estimated Stokes components \tilde{S}_1, \tilde{S}_2 , and \tilde{S}_3 thus affecting the *MSE* calculations. For a fixed object brightness, the choice of the reconstruction region in the image affects the bias and variance differently as the width of the bandpass filter is increased. The bias-variance tradeoff for different object brightness levels at various regions across the image is investigated by evaluating the metric, Normalized MSE (*NMSE*), as a function of the bandwidth.

In the final section the Signal to Noise Ratio (*SNR*) is evaluated for shot noise limited cases as the DOP of the incoming light is decreased. The modulation of the fringes encoding the polarization information depend on the DOP of input light with the maximum modulation (visibility = 1) occurring for input light of DOP = 1 and minimum modulation (visibility = 0) occurring for input light of DOP = 0. Unlike dispersion effects where the modulation of fringes is not the same for all illuminated regions of the detector, the decrease in DOP (< 1) of input light causes a uniform decrease in the modulation of fringes across all illuminated regions of the detector. Shot noise and read noise inhibit the detection of the fringes when either the noise level becomes comparable to the signal or the DOP of input light decreases or both. Shot noise limited flat field cases are chosen to study the *SNR* as a function of the DOP of input light. This Chapter consists of the following sections:

- Bias-variance tradeoff: Choosing unit cell size.
- Bias-variance tradeoff: Dispersion effects.
- Sensitivity analysis: Shot noise limited detection.

6.1 Bias-variance tradeoff : Choosing unit cell size

In the estimation of the Stokes parameters the slide reconstructor uses the equation

$$\vec{\tilde{\mathbf{S}}} = ((\mathbf{F}^T \mathbf{F})^{-1} \mathbf{F}^T) \vec{\mathbf{O}}$$

to reconstruct $\tilde{S}_0, \tilde{S}_1, \tilde{S}_2$, and \tilde{S}_3 images. \mathbf{F} is the measurement matrix constructed from the calibration fringes given by Equation 4.4 , $((\mathbf{F}^T \mathbf{F})^{-1} \mathbf{F}^T)$ is the synthesis matrix representing the least square inverse of the measurement matrix \mathbf{F} , $\vec{\mathbf{O}}$ is the vector of intensity values from the pixels of the unit cell and $\vec{\tilde{\mathbf{S}}}$ is the vector representing the estimated Stokes parameters. The size of the matrix $((\mathbf{F}^T \mathbf{F})^{-1} \mathbf{F}^T)$ and vector $\vec{\mathbf{O}}$ depends on the number of pixels in the unit cell. The measurement matrix \mathbf{F} and vector $\vec{\mathbf{O}}$ are of dimensions $M \times 4$ and $M \times 1$ respectively, where M is the number of pixels in the unit cell.

For a system with well-conditioned measurement matrix and high numerical precision, the bias term would be dominant compared to the variance in MSE (Equation 6.1) when the signal levels dominate noise levels. The magnitude of the bias term depends on the size of the unit cell used for the Stokes reconstruction - larger bias values for unit cells $> 3 \times 3$ that sample the PSF at rates lesser than Nyquist. In imaging of scenes with spatial features, an increase in size of the unit cell would cause the variance term to decrease, and bias term to increase. The decrease in the variance

is due to the increased number of measurements within a unit cell and a consequent increase in the number of rows in the measurement matrix \mathbf{F} . For example, a unit cell of size 3 X 3 would provide 9 measurements (9 rows in the measurement matrix) while a unit cell of size 4 X 4 would provide 16 measurements (16 rows in the measurement matrix). Moreover, with unit cells of higher dimensions, the slide reconstruction procedure offers averaging over a larger number of estimations for each of the Stokes components - a maximum of 9 estimations for unit cell size 3 X 3 and a maximum of 16 estimations for unit cell size 4 X 4 (see Section 4.2).

For cases where the incident light is of $DOP = 1$ and monochromatic, the MSE may or may not increase as the unit cell size is increased depending on the SNR in the detected image. The SNR is defined as follows:

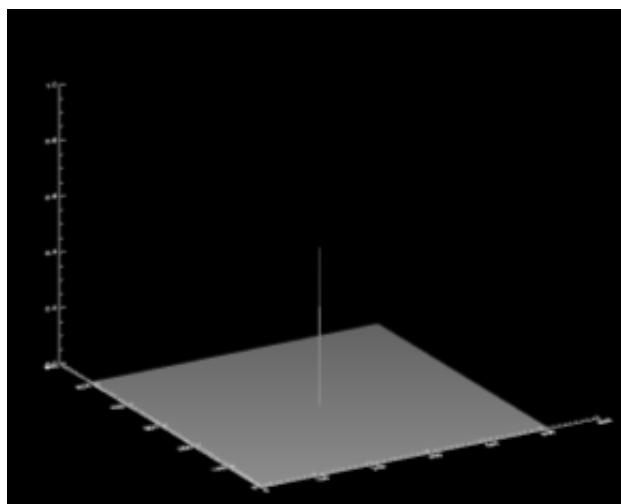
$$SNR = \frac{\text{Mean photon count}}{\text{Standard deviation}}$$

The noise levels are dominant than signal level when the energy of the light collected from the objects or scenes are lower than the energy due to noise of the detector and its associated electronic circuitry. The signal level at the detector can be less than the noise due to low brightness of the object or scene being imaged, transmission properties of components (filters) used along with the collection optics, and short exposure times of the camera.

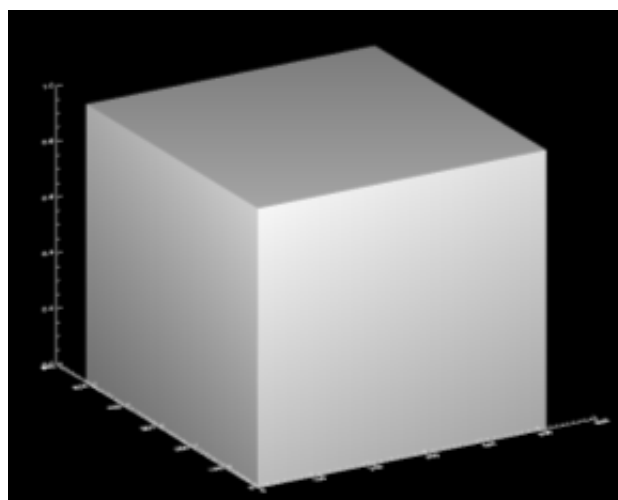
The objects and scenes imaged by the ISIP can be of different sizes and shapes at various brightness levels. The lateral spread of light incident on the BCA's entrance aperture can vary from a size of the PSF of the collection optics (when imaging a point source such as a star) to that of the entire physical extent of the entrance face of the BCA (when calibration fringes are generated). Hence the polarization domain can be of varying sizes and shapes based on the object or scene being imaged.

The bias-variance tradeoff study is done for three different objects - a point source, satellite object and a uniform flat field as shown in Figure 6.1a, 6.1c, and 6.1b. The point source and satellite object are imaged by the ISIP while the flat field is modeled as a beam of uniform intensity and polarization illuminating the entire entrance face of the BCA without any fore-optics in front of it. In both cases the images from the BCA are recorded by a detector model whose pixels Nyquist sample the calibration fringes. The telescope model used in the ISIP assembly has a PSF width ($1.22 \times \lambda \times F/\#$) of 15 pixels in the discretized detector image of the PSF. The point source and uniform flat field are modeled as completely polarized ($\text{DOP} = 1$) sources with equal amounts in energy in S_1 , S_2 , and S_3 Stokes components. However, the satellite object in Figure 6.1c has different polarizations across it - central circular region has horizontal polarization, left rectangular region has 45 polarization, and right rectangular region has RHC polarization. The total amount of energy in S_1 , S_2 , and S_3 Stokes components of the satellite object are approximately the same, though the intensity is less in the circular region compared to the rectangular regions. The wavelength of light from these different regions are same (monochromatic) and completely polarized ($\text{DOP} = 1$).

The number of PDE at the detector is varied during the imaging - 10^4 , 10^5 , 10^6 , and 10^7 PDE for point source, 10^5 , 10^6 , 10^7 , and 10^8 PDE for the satellite object and 10^6 , 10^7 , 10^8 , and 10^9 PDE for the flat field, to model different brightness levels of the objects. Both shot noise and read noise are included in the final image. The read noise for each pixel is identically distributed and has been modeled as an additive normally distributed random variable with a RMS value of 15 electrons



(a) Point source.



(b) Flat field.



(c) Satellite object.

Figure 6.1: Objects used in the imaging.

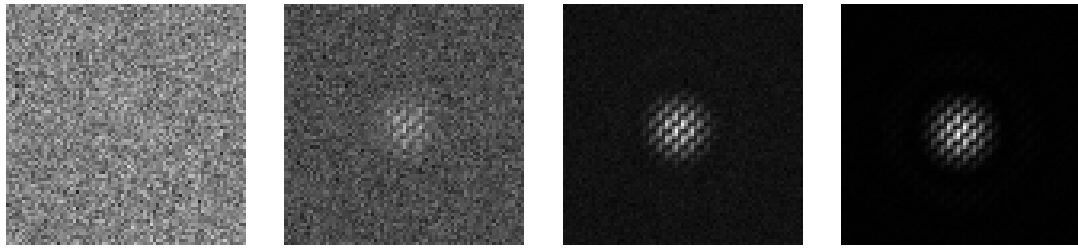


Figure 6.2: Noisy images: Point source Left to Right: 10^4 PDE, 10^5 PDE, 10^6 PDE, and 10^7 PDE.

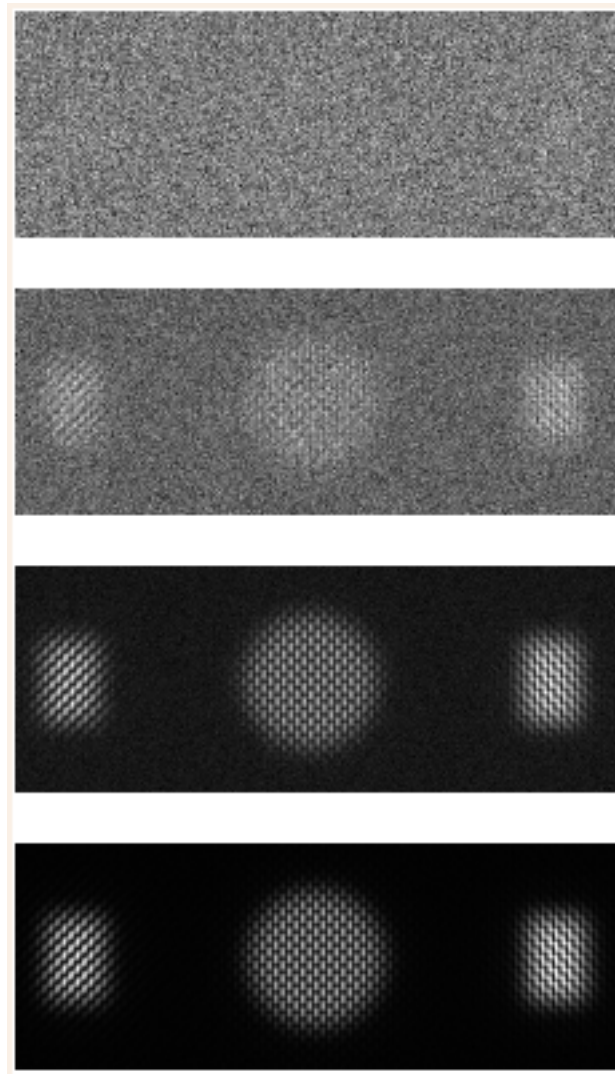


Figure 6.3: Noisy images: Satellite object Top to Bottom: 10^5 PDE, 10^6 PDE, 10^7 PDE, and 10^8 PDE.



Figure 6.4: Noisy images: Flat field Top to Bottom: 10^6 PDE, 10^7 PDE, 10^8 PDE, and 10^9 PDE.

Point Source	
Object brightness level	SNR
10^4 PDE	18
10^5 PDE	158
10^6 PDE	876
10^7 PDE	3115

Flat field	
Object brightness level	SNR
10^6 PDE	252
10^7 PDE	2010
10^8 PDE	9335
10^9 PDE	31392

Satellite object	
Object brightness level	SNR
10^5 PDE	56
10^6 PDE	497
10^7 PDE	2768
10^8 PDE	9850

Table 6.1: SNR values for detector images obtained at various object brightness levels.

per pixel and per read out operation. The *SNR* of the detector image of the objects - point source, flat field, and satellite object, at different brightness levels are shown in Table 6.1. The *SNR* has been calculated based on regions in image that have atleast 1% of the peak energy in the true image.

The averaging operation in Equations 6.2 and 6.3 requires multiple estimated frames of the same Stokes component. Hence a stack of 100 images with different realizations of shot noise and read noise are created from the noise free image of the objects. Figure 6.2 shows a realization of the noise corrupted image for each of the objects for increasing number of PDE at the detector. The number of PDE in each of the noise corrupted image have been defined at the entrance face of the BCA. The number of PDE per pixel in the detector image without the BCA for sources - point

Point Source	
Brightness level (PDE)	Average number of PDE per pixel
10^4	30
10^5	297
10^6	2970
10^7	19696

Flat field	
Brightness level (PDE)	Average number of PDE per pixel
10^6	61
10^7	610
10^8	6104
10^9	61035

Satellite object	
Brightness level (PDE)	Average number of PDE per pixel
10^5	30
10^6	295
10^7	2950
10^8	29507

Table 6.2: Average number of PDE per pixel at various brightness levels of point source, flat field, and satellite object.

source, flat field, and satellite object, at various brightness levels are defined in Table 6.2 and this number has to be multiplied by the appropriate intensity transmission values in Table 3.1 in order to calculate the PDE at the detector plane when the BCA is present. The slide reconstruction procedure with an initial unit cell size of 3 X 3 is used to produce 100 different estimations for each of the Stokes components S_0 , S_1 , S_2 , and S_3 . The procedure is repeated with higher dimension unit cells (up to 20 X 20) with 100 different estimations for the Stokes components every time the reconstruction is run with an incremented unit cell size.

The MSE metric along with the PAB and PAV for each of the Stokes components are evaluated and plotted as a function of number of unit cells per $1.22 \times \lambda \times F/\#$ for the point source and satellite object as in Figures 6.5, 6.6, 6.7, 6.8, 6.13, 6.14, 6.15, and 6.16 respectively. For the flat field (Figure 6.9, 6.10, 6.11, and 6.12) the

metrics are plotted as function of the number of pixels in the unit cell since there are no fore-optics in front of the BCA.

In the case of the point source and satellite object it is seen that a low brightness level where the noise levels are significant (10^4 PDE ($SNR = 18$) and 10^5 PDE ($SNR = 56$) in Figures 6.5 and 6.13), increasing the size of the unit cell used in the reconstruction results in a monotonic decrease in MSE. The decrease in the variance (PAV) is dominant than the increase in the bias (PAB) for each of the Stokes components. However, when the signal level becomes nominal in the point source case (10^5 PDE ($SNR = 158$) in Figure 6.6) the metric MSE decreases till the number of the unit cells sampling PSF half width ($1.22 \times \lambda \times F/\#$) is approximately two, a further increase in unit cell size causes increasing bias (PAB) effects to dominate the decreasing Variance (PAV). For the nominal signal level of the satellite object (10^6 PDE ($SNR = 497$) Figure 6.14) the number of unit cells sampling the PSF half width ($1.22 \times \lambda \times F/\#$) can be increased beyond two and the MSE would still decrease. The reason for this decrease is due to the fact that the intensity roll off from the center of the polarization domains is slow for the satellite object compared to the point source. Consequently the bias in the satellite object increases at a slow rate compared to the point source. Another important result to be noted in Figure 6.14 (satellite image) is the difference in the bias curves for S_1 , S_2 , and S_3 , the curve for S_1 rises at a slower rate compared to S_2 and S_3 . The S_1 curve corresponds to the circular central region (Figure 6.1c) which is larger compared to the rectangular region on either side. Consequently, the central circular region would have a large polarization domain and slow increase in bias compared to rectangular regions as seen in the bias plots Figure 6.14. As the signal level increases further (10^6 PDE ($SNR = 876$) and 10^7 PDE ($SNR = 3115$) for the point source in Figures 6.7 and 6.8; 10^7 PDE ($SNR = 2768$) and 10^8 PDE ($SNR = 9850$) for the satellite object in

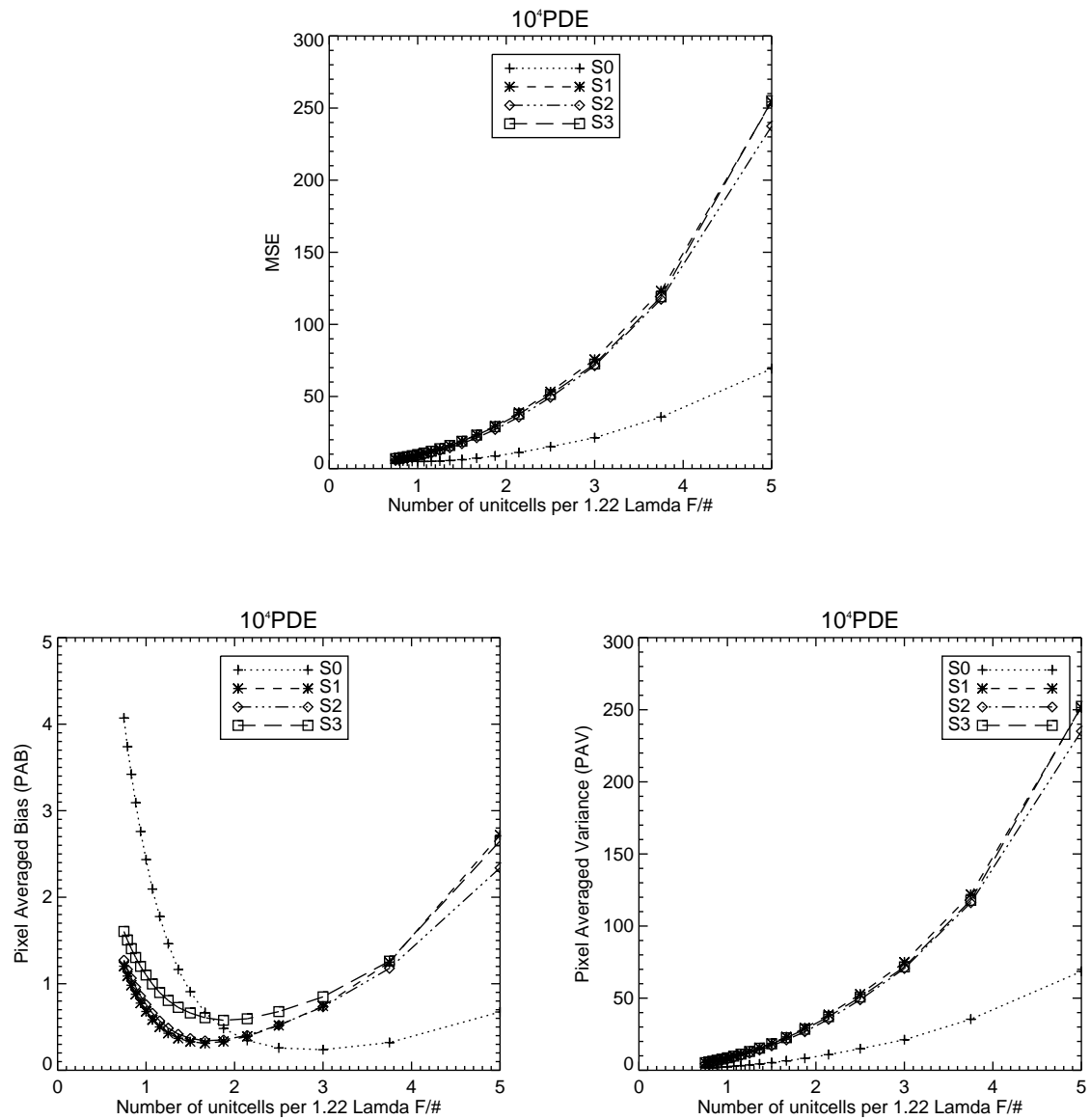


Figure 6.5: Point source: MSE, bias, and variance curves (10^4 PDE).

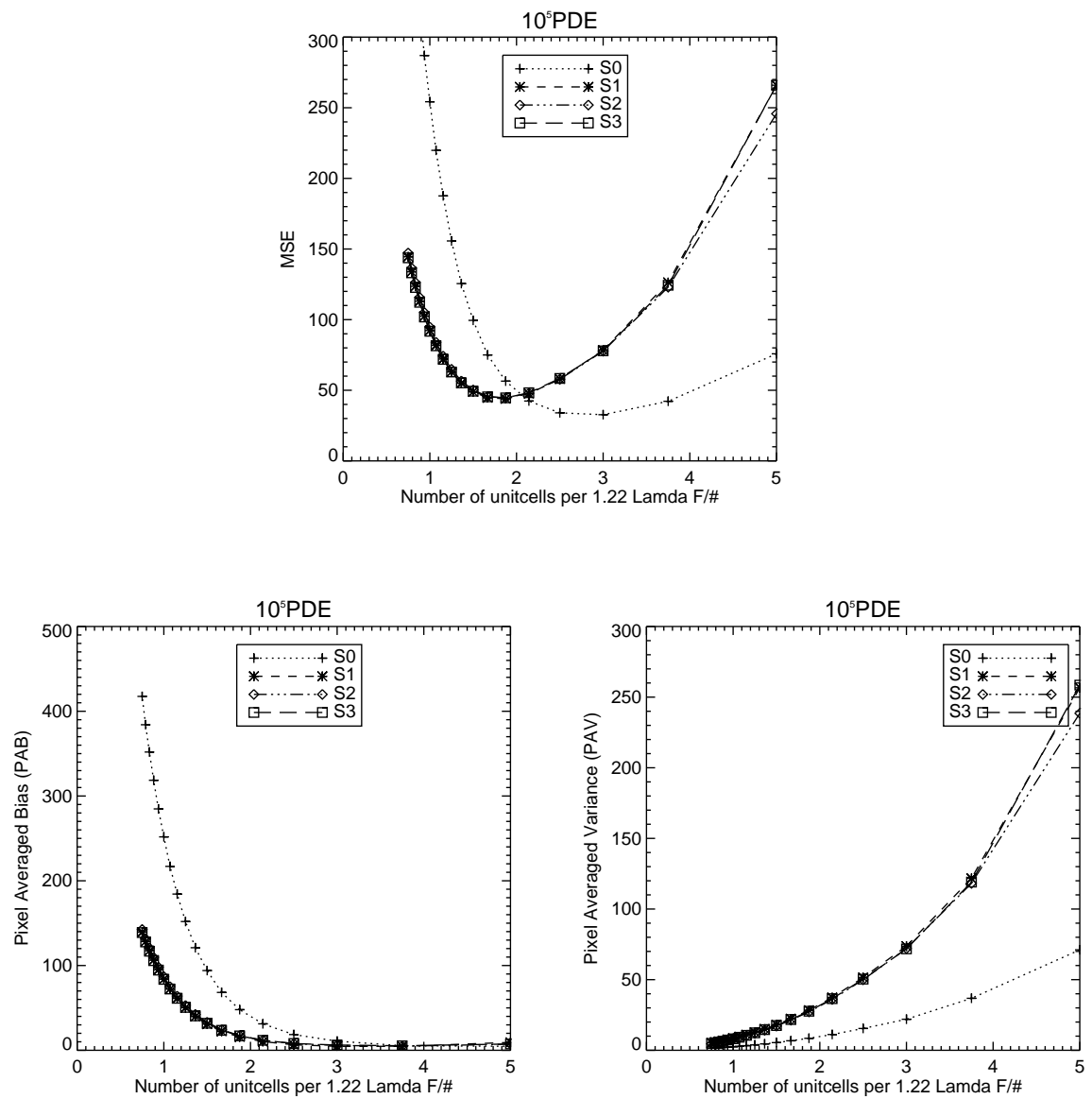


Figure 6.6: Point source: MSE, bias, and variance curves (10^5 PDE).

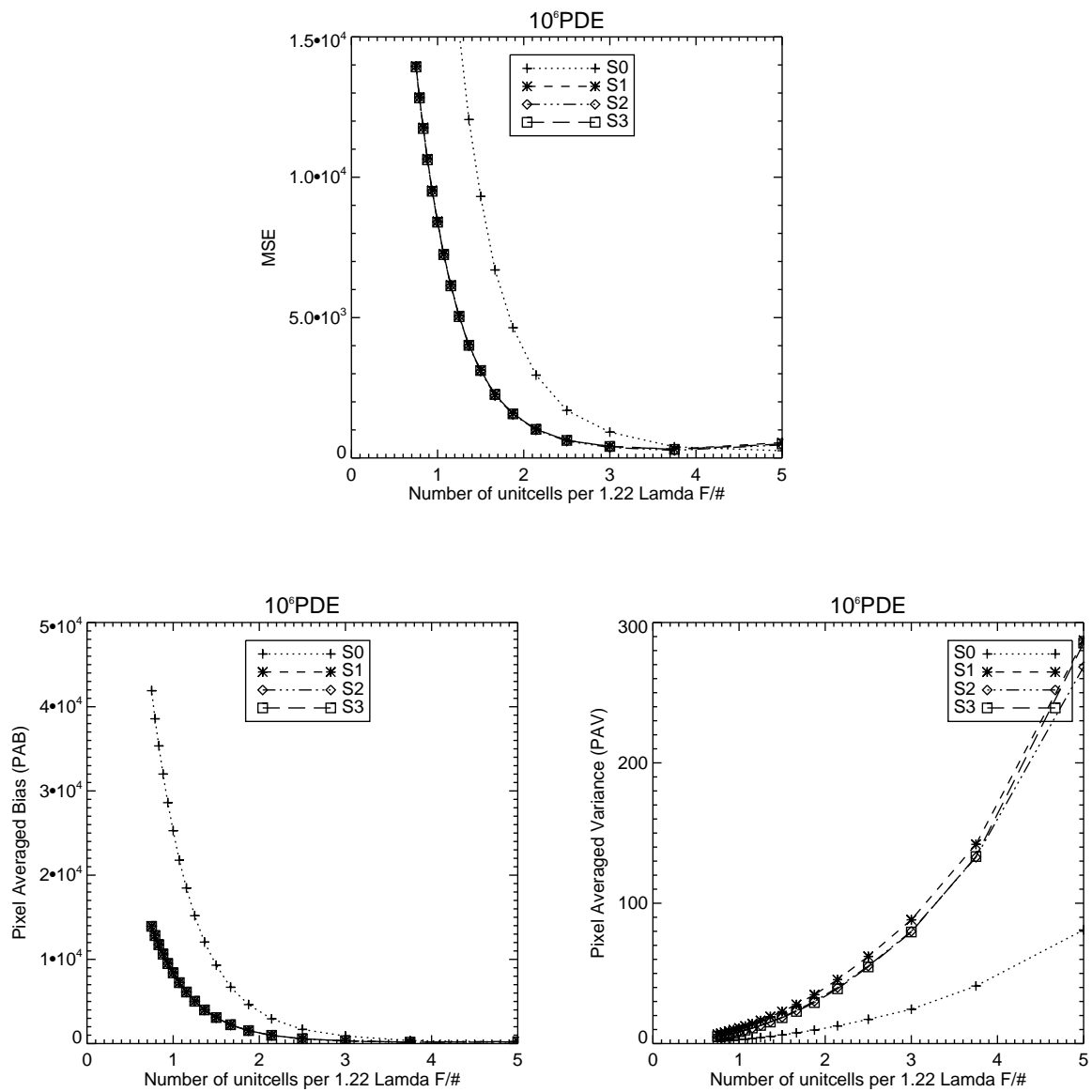


Figure 6.7: Point source: MSE, bias, and variance curves (10^6 PDE).

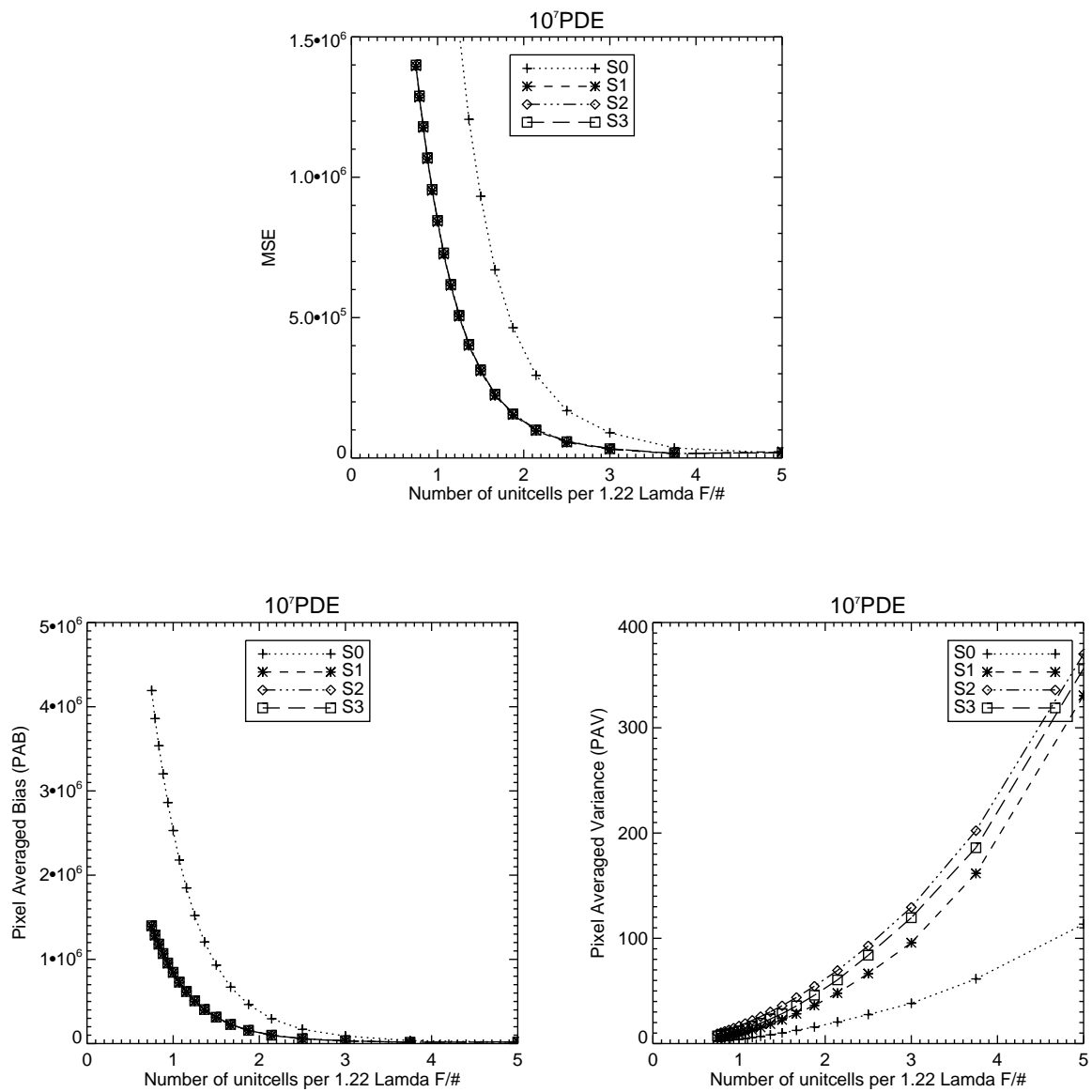


Figure 6.8: Point source: MSE, bias, and variance curves (10^7 PDE).

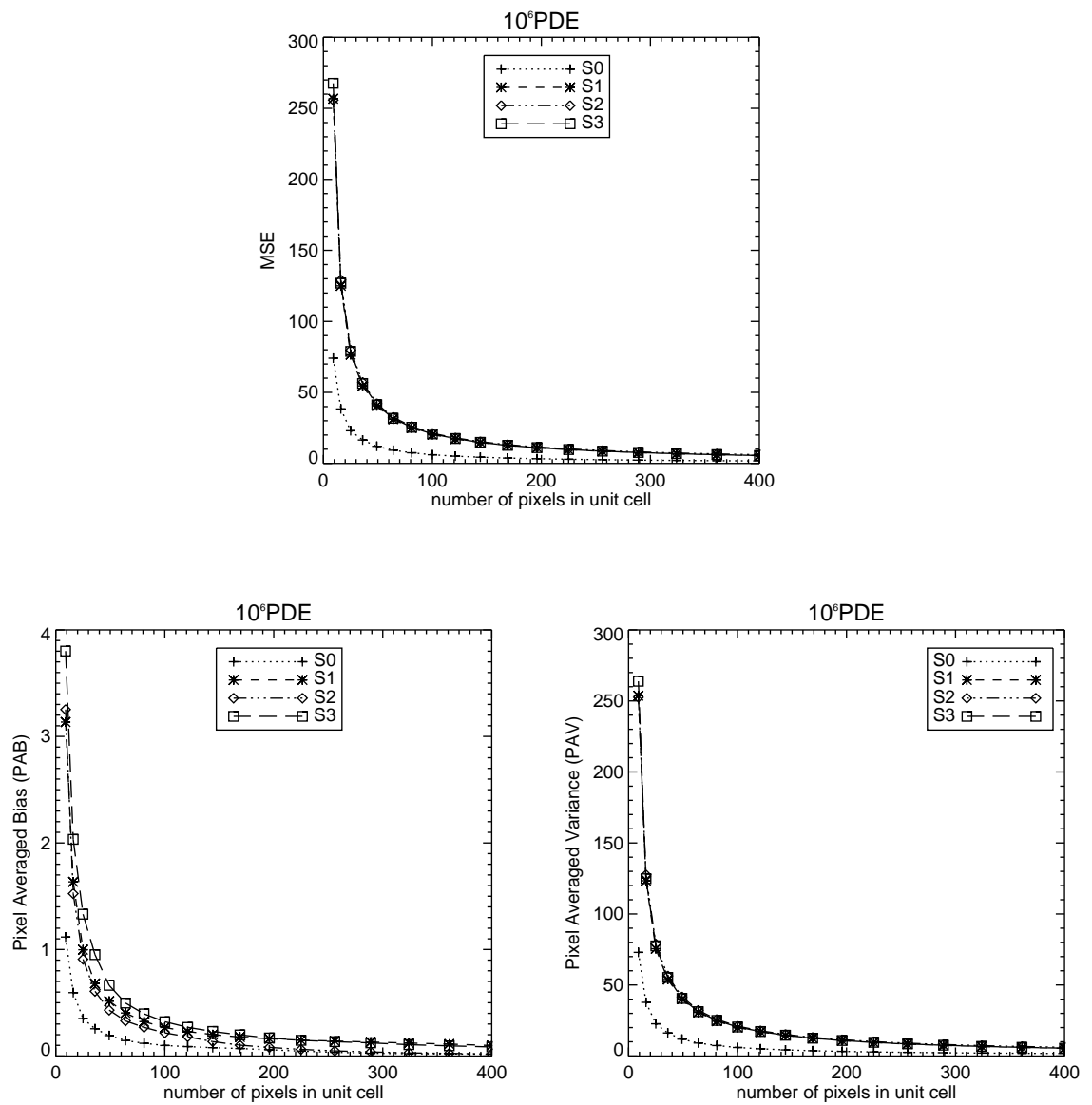


Figure 6.9: Flat field: MSE, bias, and variance curves (10^6 PDE).

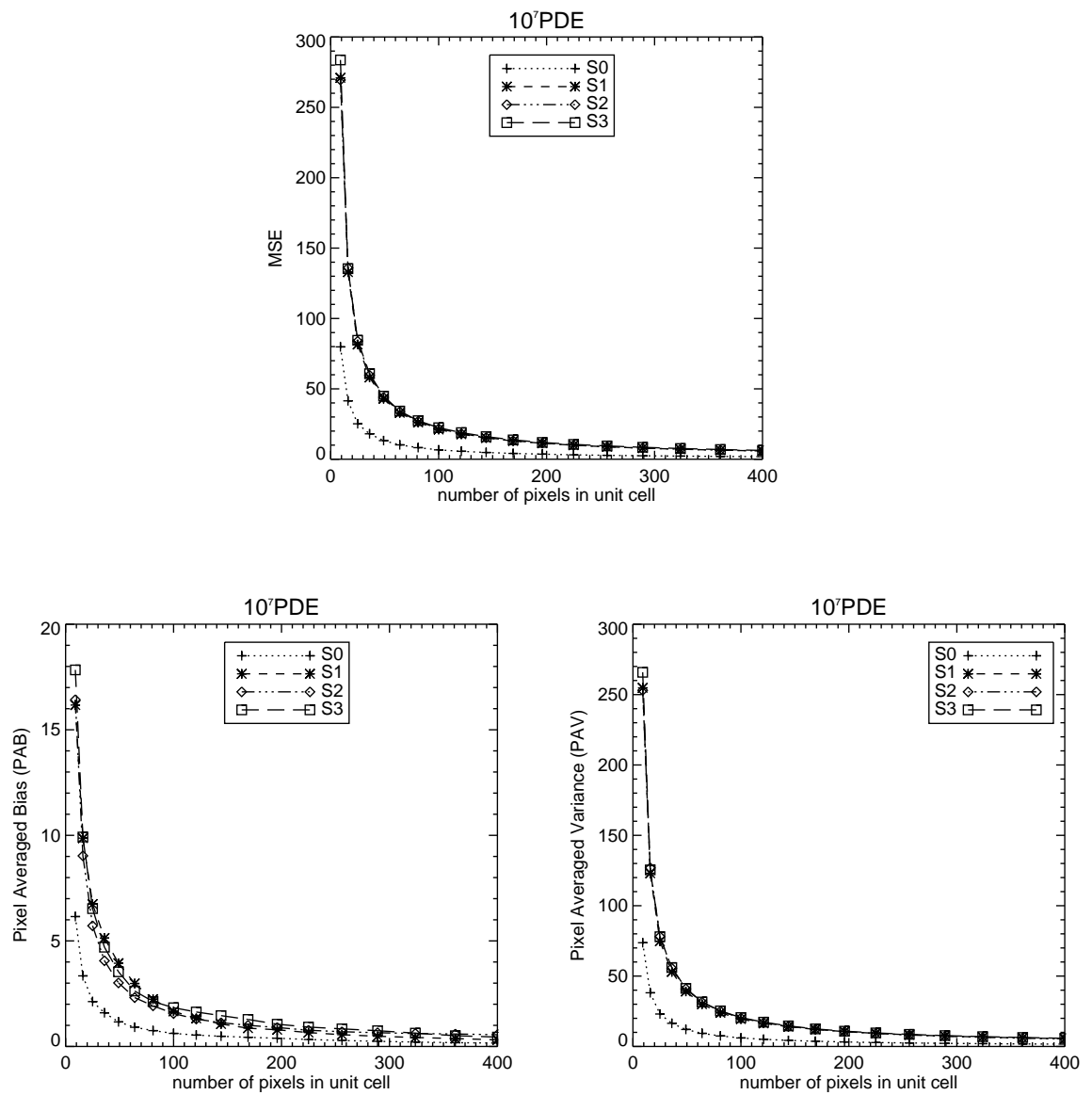


Figure 6.10: Flat field: MSE, bias, and variance curves (10^7 PDE).

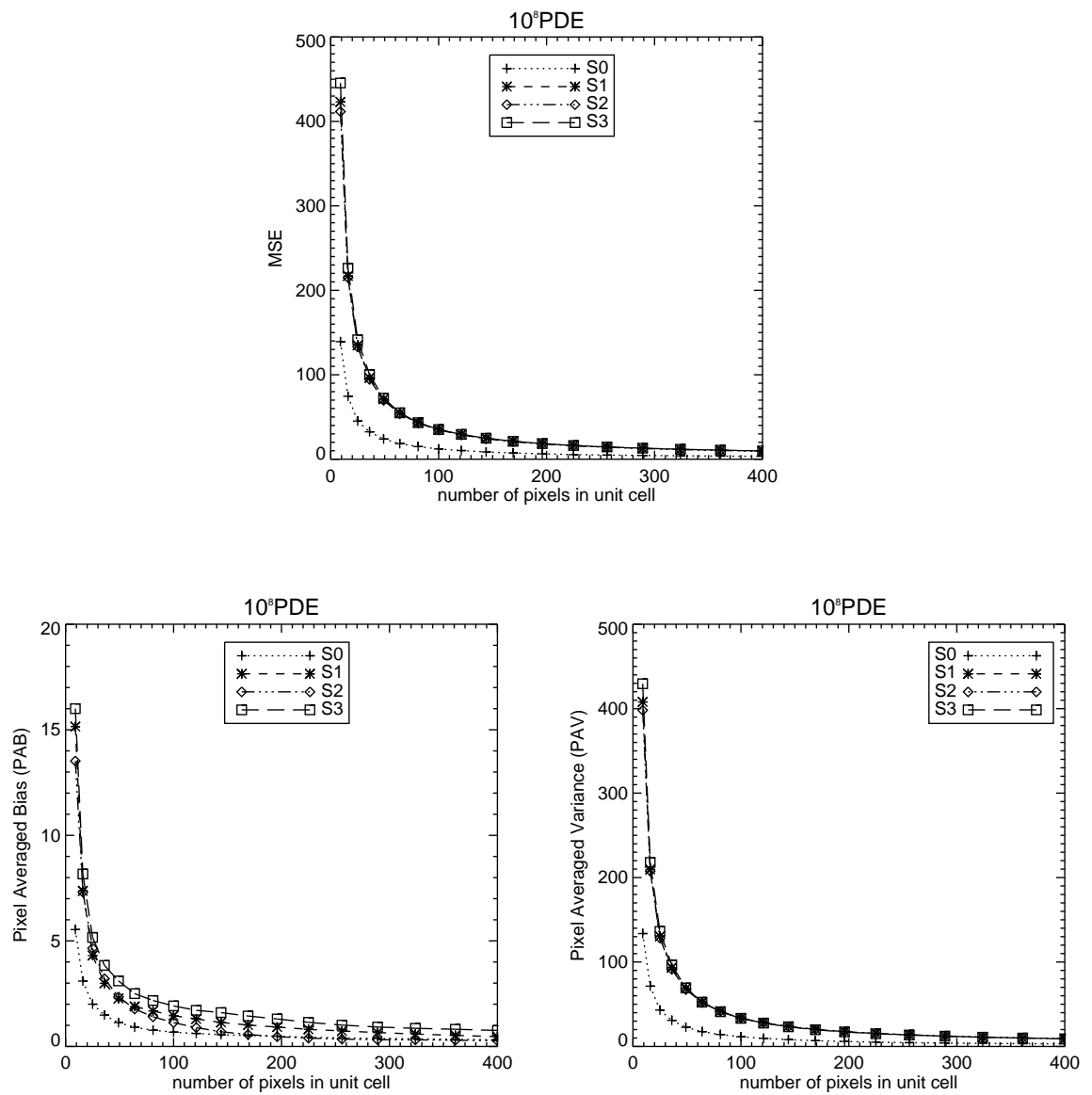


Figure 6.11: Flat field: MSE, bias, and variance curves (10^8 PDE).

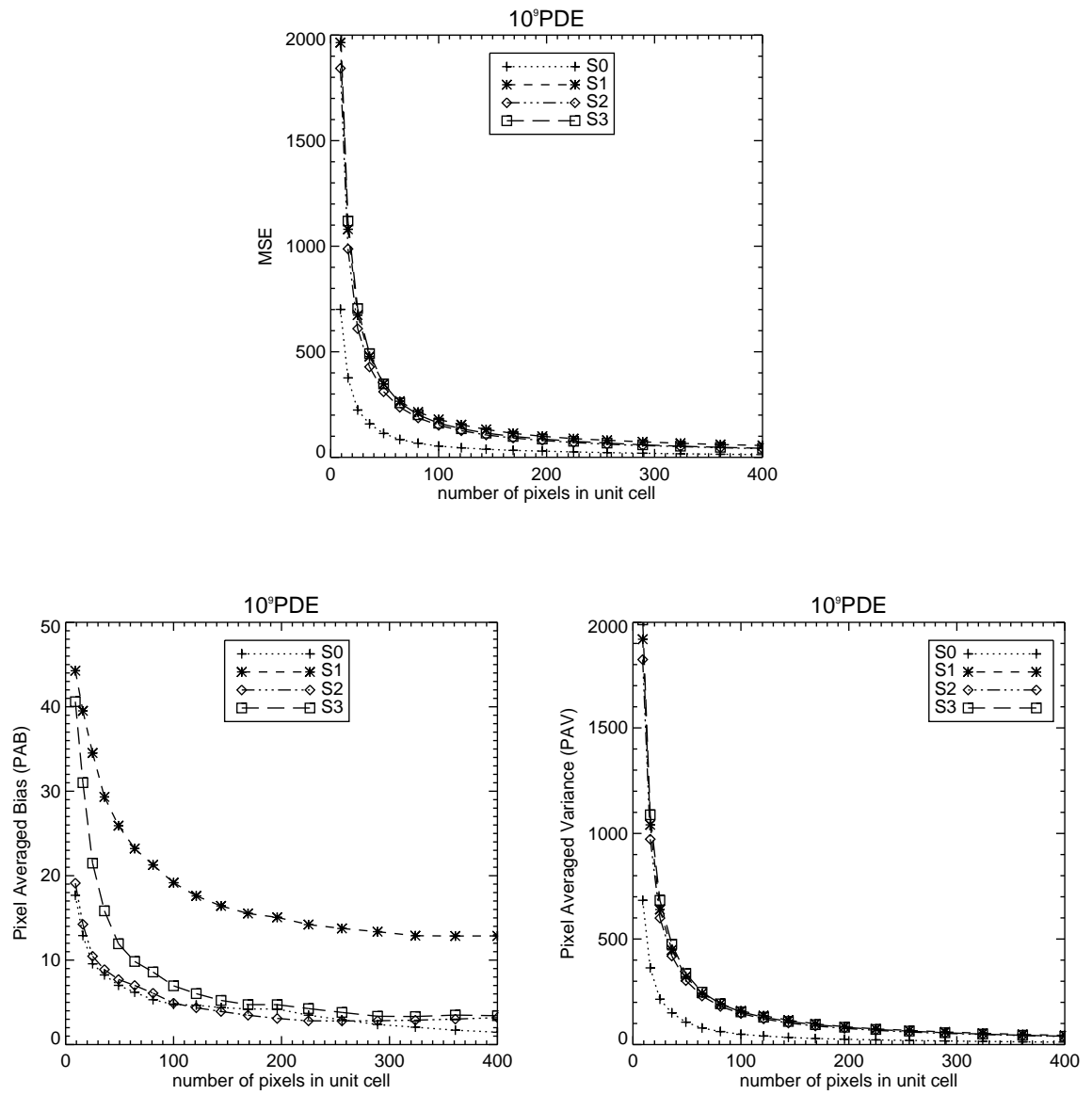


Figure 6.12: Flat field: MSE, bias, and variance curves (10^9 PDE).

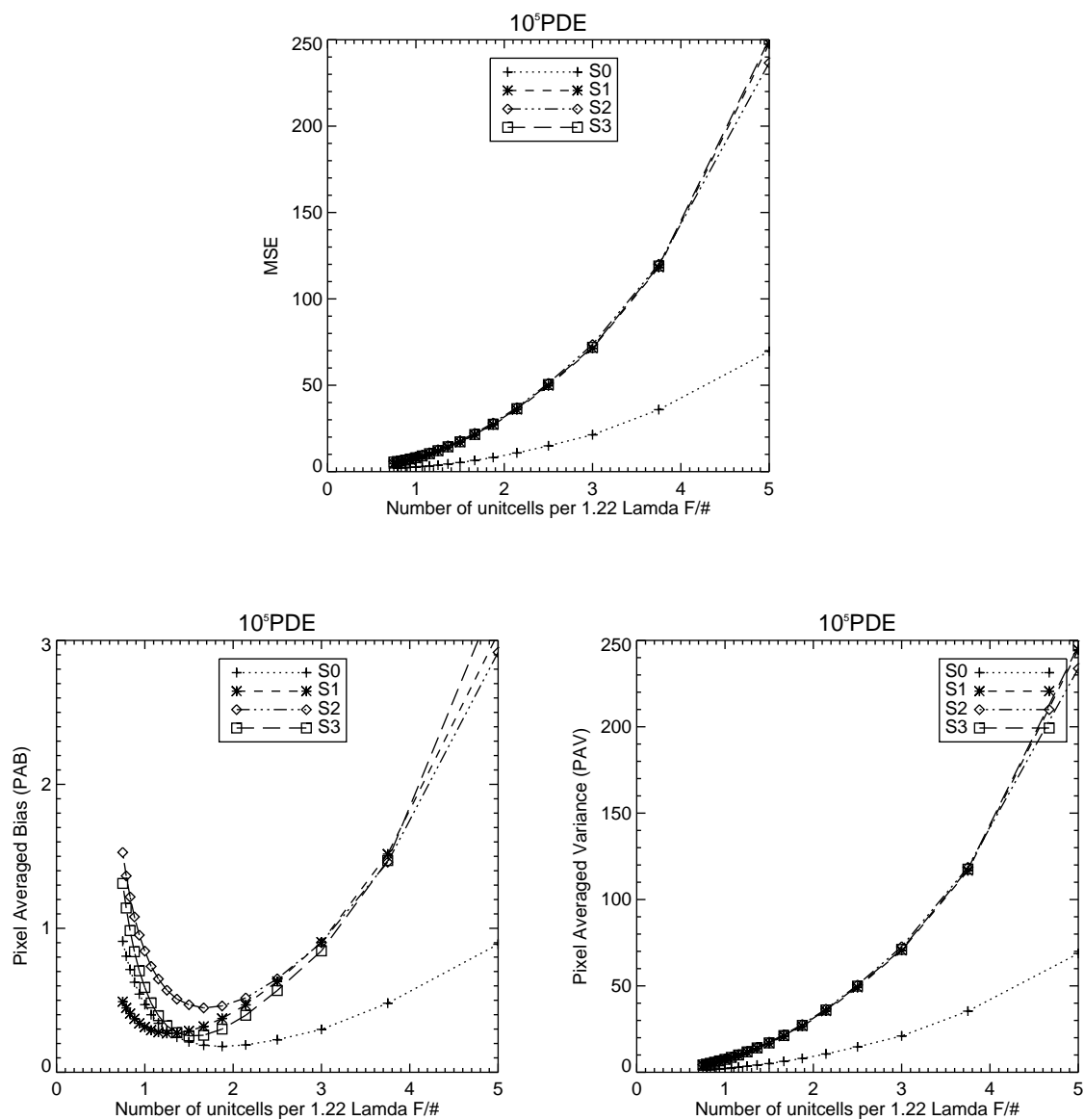


Figure 6.13: Satellite object: MSE, bias, and variance curves (10^5 PDE).

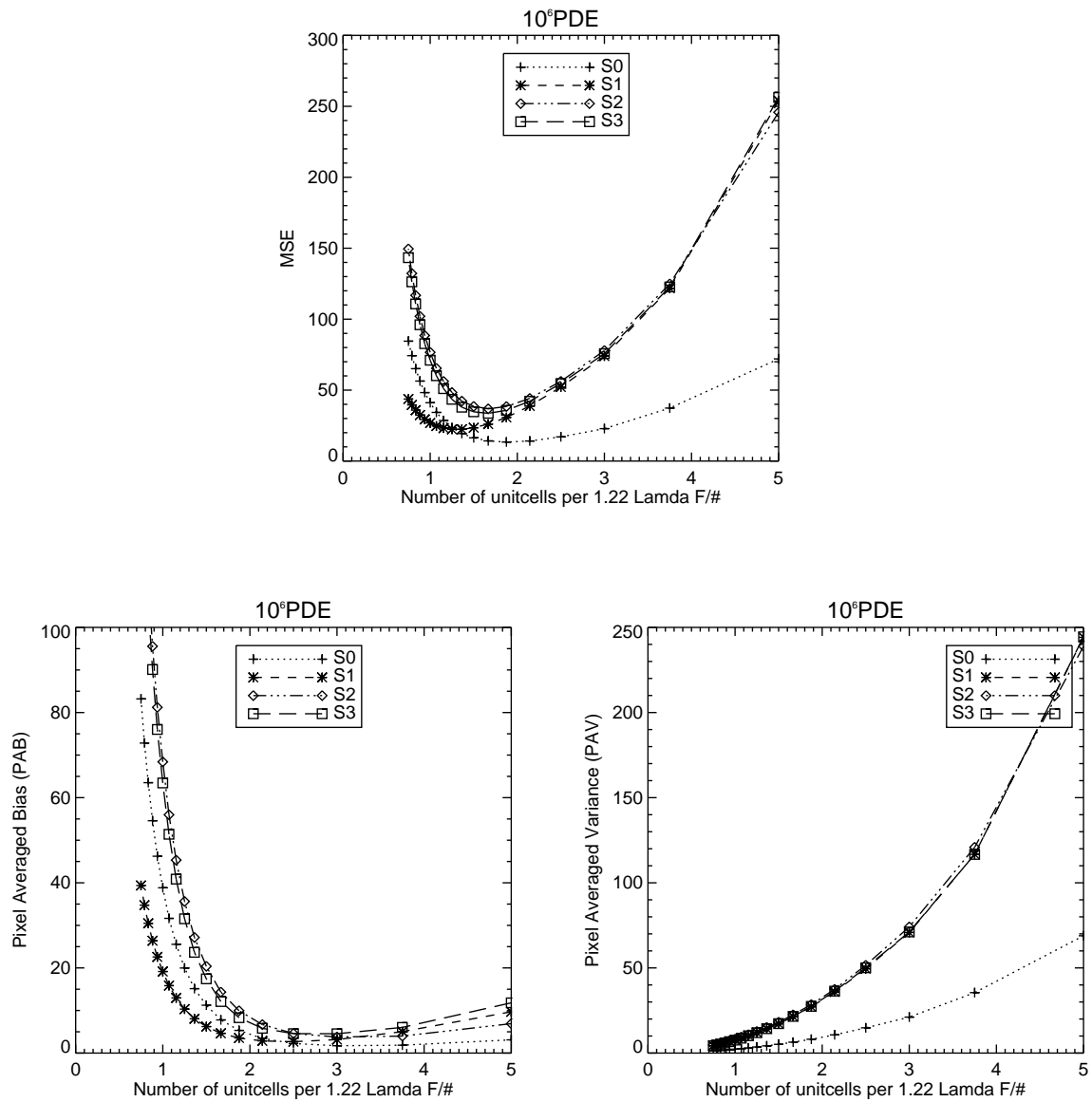


Figure 6.14: Satellite object: MSE, bias, and variance curves (10^6 PDE).

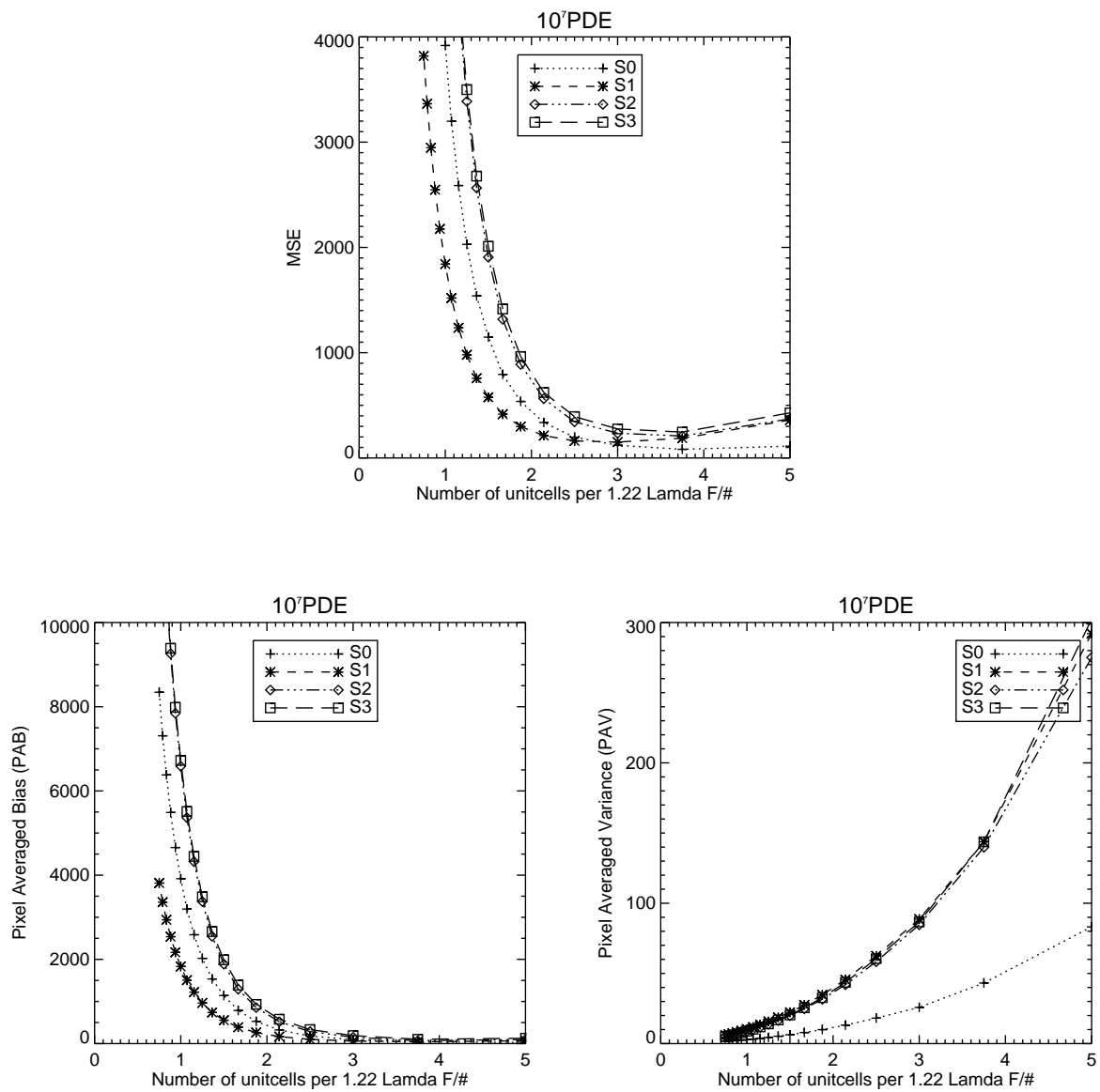


Figure 6.15: Satellite object: MSE, bias, and variance curves (10^7 PDE).

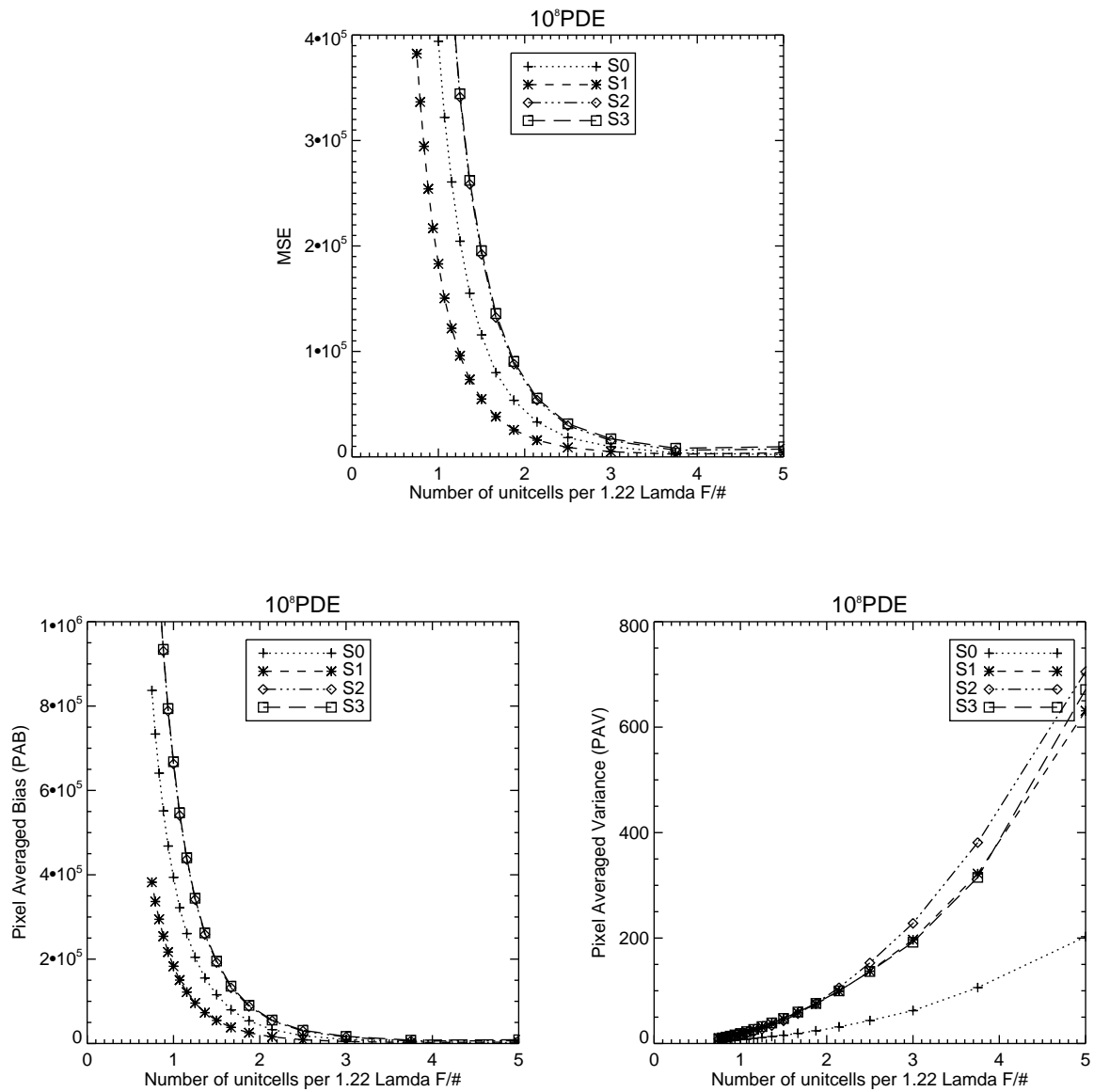


Figure 6.16: Satellite object : MSE, bias, and variance curves (10^8 PDE).

Figures 6.15 and 6.16) the reconstruction error due to bias effects of increased unit cell sizes dominates the decreasing variance and the Nyquist sampling rate (2 unit cells per $1.22 \times \lambda \times F/\#$) has to be satisfied when the choice of unit cell size is made.

In case of the flat field, there is no bias due to the physical size of unit cell chosen. The lack of bias is due to the uniform intensity and polarization over the unit cell. With increased number of pixels in the unit cell the variance decreases at all light levels (10^6 PDE ($SNR = 252$), 10^7 PDE ($SNR = 2010$), 10^8 PDE ($SNR = 9335$), and 10^9 PDE ($SNR = 31392$) PDE) as seen in Figures 6.9, 6.10, 6.11, and 6.12. The decrease in variance dominates any change in bias. The metric MSE in the case of flat field follows the variance as the magnitude of the variance is high compared to the bias at all light levels.

In reconstruction of polarization domain sizes less than the field of view of the detector the number of unit cells sampling the $1.22 \times \lambda \times F/\#$ width of the PSF is influenced by the SNR of the image from the detector. Flat field (covering the entire detector field) reconstructions do not have bounds on the size of the unit cells as there is no PSF involved and hence there are no bias-variance tradeoffs. In such cases the minimum size unit cell is 3×3 and maximum sized unit cell is the dimension of the detector field.

The bias and variance curves for S_0 are different for all objects due to increased energy compared to S_1 , S_2 , and S_3 . The increased energy makes the bias for S_0 rise fast and variance decrease slow compared to S_1 , S_2 , and S_3 in the point source case as the size of the unit cell is increased. In the flat field case, the variance decrease for S_0 is also slow compared to other Stokes components. For the case of the satellite object (Figures 6.13, 6.14, 6.15, and 6.16) the S_0 bias is averaged over the circular and rectangular regions. Consequently the rise in bias for S_0 falls in between S_1 , S_2 , and S_3 while the variance decrease for S_0 is slow compared to other Stokes components.

6.2 Bias-variance tradeoff: Dispersion effects

The BCA in the ISIP is made of positive uniaxial birefringent crystal wedges whose refractive indices - n_e and n_o vary with wavelength of incident light. Due to this dispersive nature of the crystals, the spatial period of the intensity fringes encoding the polarization information depend on the wavelength of input light. Hence, input light having finite spectral width results in a fringe pattern that can be approximated as a summation of individual fringe patterns corresponding to discrete wavelengths in the band. This summation results in a loss of fringe visibility due to destructive interference of the individual fringe patterns and this loss starts out at the edges of the image proceeding towards the center as the wavelength spread increases. For a narrow field of view the effects of angular dispersion of the birefringent crystals are pronounced at the edges of the image compared to the center. Consequently, a smaller spectral bandpass affects the visibility of the fringes at the edges of the image compared to the center. The visibility is related to the wavelength spread of input light by a Fourier transform. The wavelength spread of incident light on the BCA is usually limited by a bandpass filter used in the ISIP configuration. The use of a relatively narrow bandpass filter preserves the modulation of the fringes in most parts of the image and is useful when imaging objects or scene of high brightness levels. However, the use of a narrow bandpass filter can reduce the signal level when objects or scenes of low brightness are imaged thereby making the fringe modulation undetectable in a noisy image. A wide bandpass filter lets more light in compared to a narrow bandpass filter thereby increasing the signal level compared to noise level. The increase in signal level is accompanied by a loss of fringe visibility starting from the edge of the image and moves towards the center preventing faithful reconstruction of the polarization information. Since the polarization and temporal

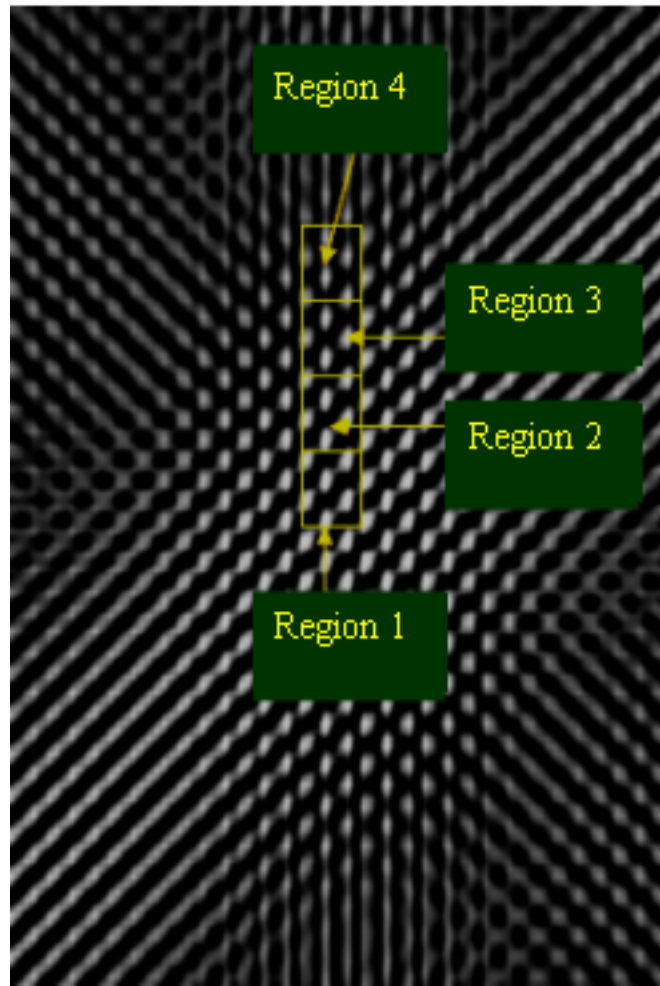


Figure 6.17: Dispersion effects of the BCA.

coherence are intimately related, use of a relatively wide bandwidth introduces some intrinsic bias in the estimation of the polarization at a particular wavelength; that is, if the polarization is a rapidly varying function of wavelength, using a relatively wide-band filter could result in significant bias independent loss in visibility. With objects and scenes of increasing brightness levels, the reconstruction error varies across the image as the bandwidth is increased gradually from a narrow band to a wider band.

To show the dispersive effects of the BCA, a flat field with $\text{DOP} = 1$ and equal energies in each of the Stokes components - S_1 , S_2 , and S_3 across a wide range of

wavelength (400nm to 700nm) is chosen to be the source of input light. A bandpass filter limits the wavelength spread of the input light incident on the entrance face of the BCA and the energy in each nm of incident light is assumed to be equal. The dispersion effects of the BCA for a 50 nm bandwidth is shown in Figure 6.17 with Regions 1, 2, 3, and 4 chosen to study the effects of increased bandwidth with input flat fields of the same polarization and different brightness levels. Region 1 is close to the centre of the image while Region 4 is the part of the image where the visibility decreases significantly for a 50 nm bandwidth. The noise free fringe modulated image obtained for each bandwidth value is corrupted with 100 different realizations of shot noise and read noise to form a stack of images. The slide reconstruction procedure is then used on each image of this stack to produce 100 different estimations for each of Stokes estimations - $\tilde{S}_0, \tilde{S}_1, \tilde{S}_2$, and \tilde{S}_3 . This process is then repeated for stacks from different bandwidths thereby producing 100 different estimations for all Stokes components for each bandwidth value.

In this study, the bias is mainly due to the loss in modulation of the fringes with increased bandwidth and the variance in the reconstructed components is due to the presence of noise in each of the individual image in the stack. The metrics - Normalized Mean Squared Error ($NMSE$), Pixel Averaged Normalized Bias ($PANB$), and Pixel Averaged Normalized Variance ($PANV$) for Regions 1, 2, 3, and 4 are evaluated are follows:

$$NMSE = \frac{MSE}{S_i^2}$$

$$= PANB + PANV$$

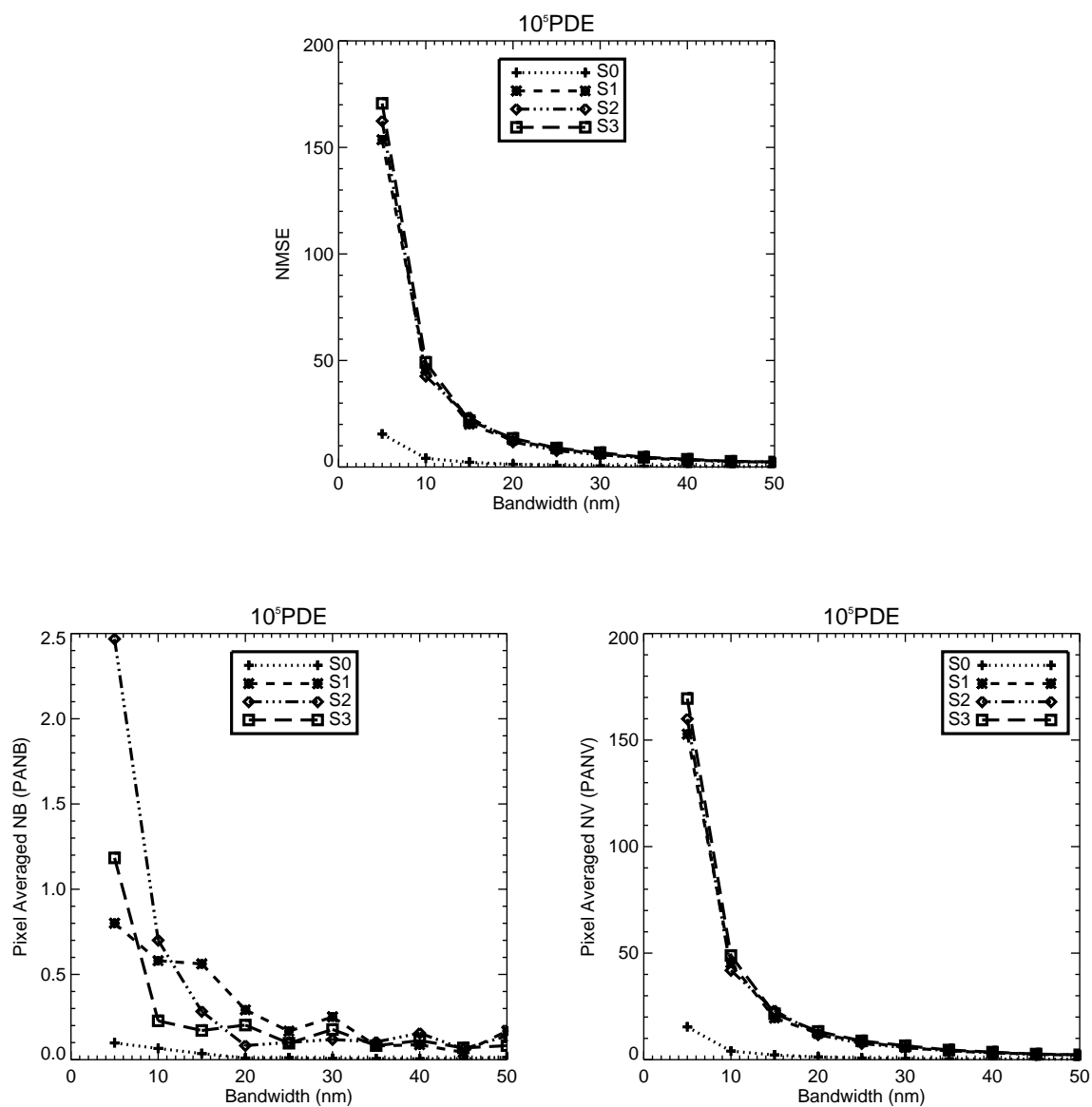


Figure 6.18: Region 1: Normalized MSE, Normalized Bias, and Normalized Variance - 10^5 PDE.

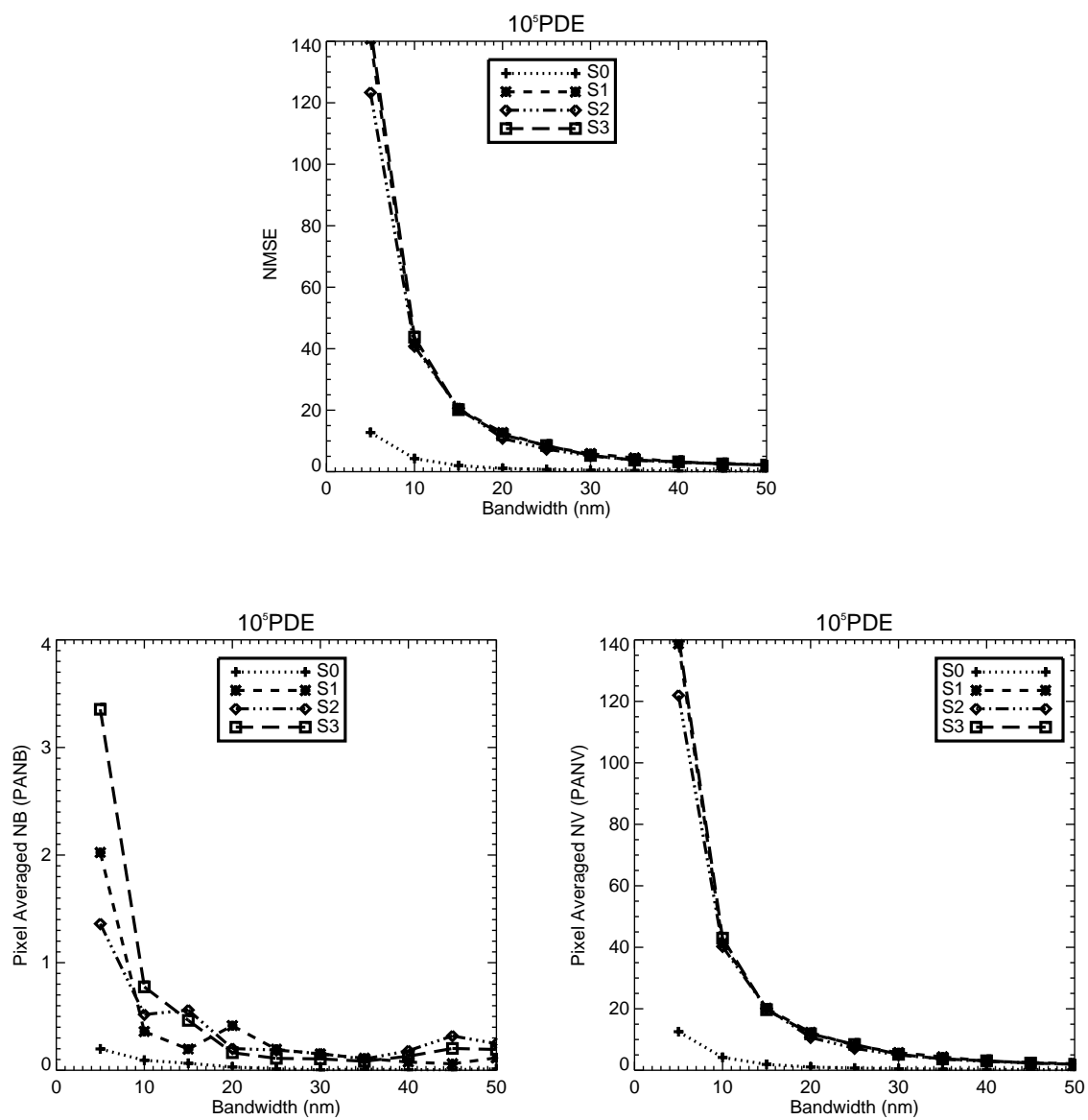


Figure 6.19: Region 2: Normalized MSE, Normalized Bias, and Normalized Variance - 10^5 PDE.

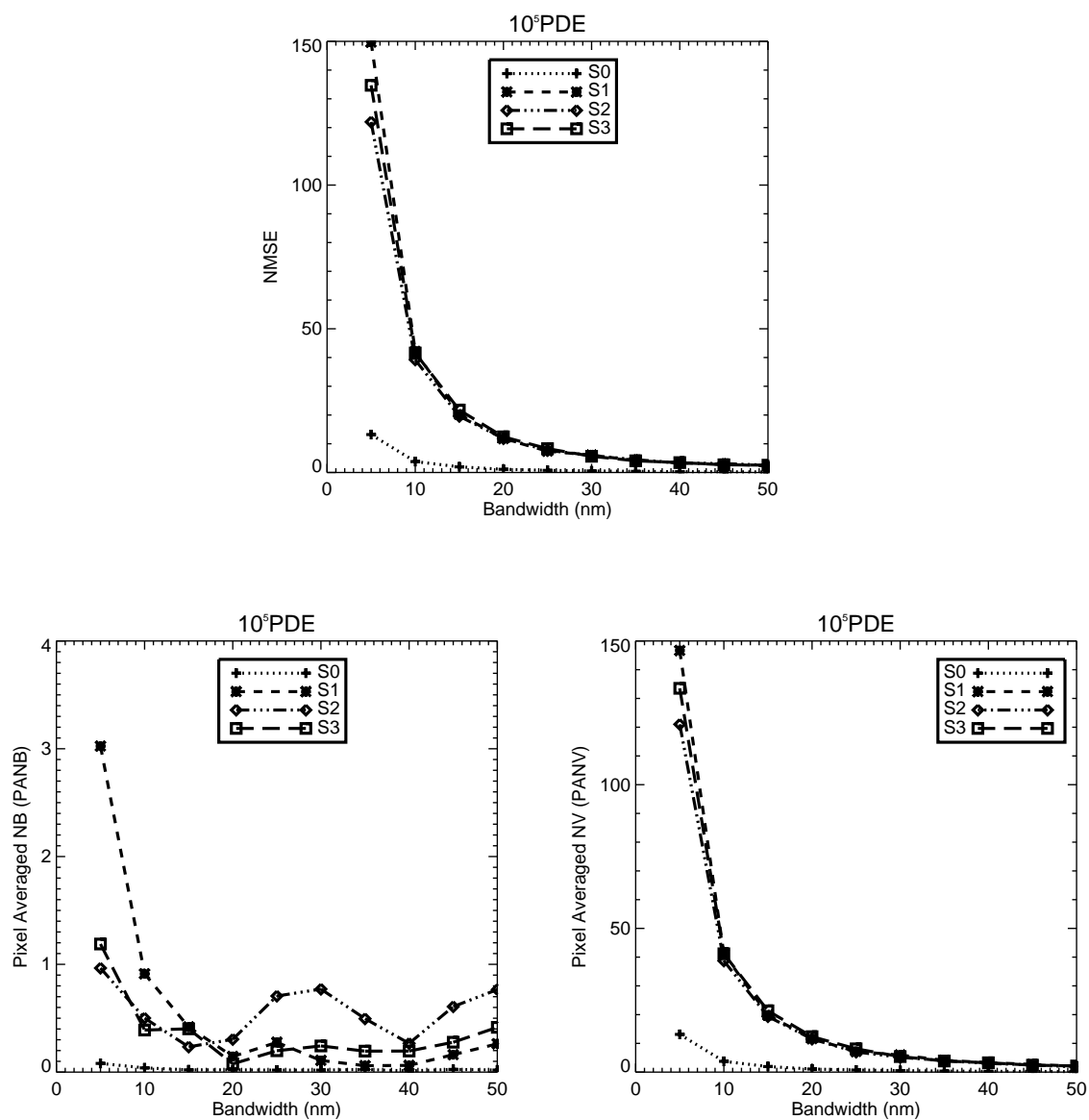


Figure 6.20: Region 3: Normalized MSE, Normalized Bias, and Normalized Variance - 10^5 PDE.

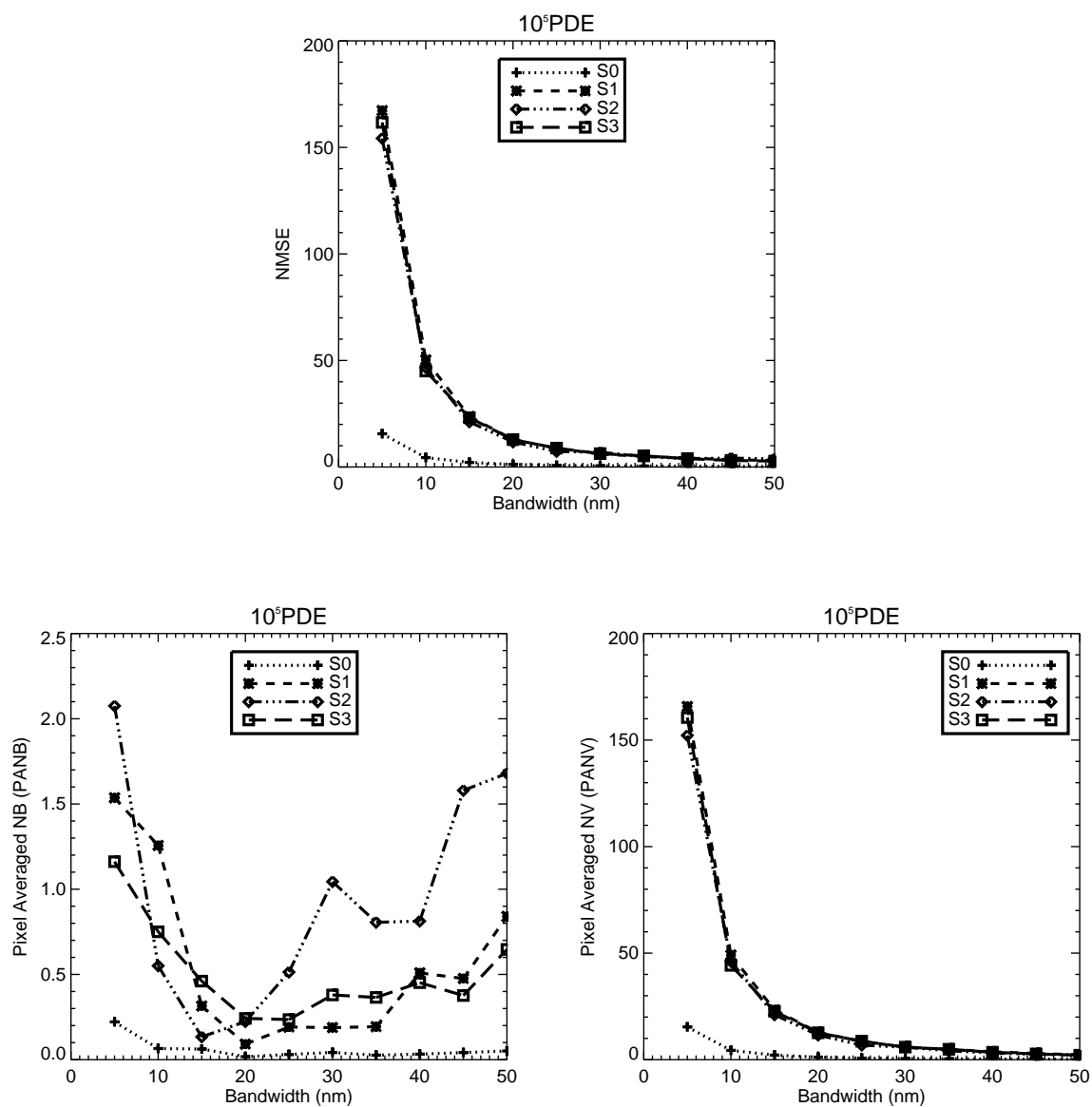


Figure 6.21: Region 4: Normalized MSE, Normalized Bias, and Normalized Variance - 10^5 PDE.

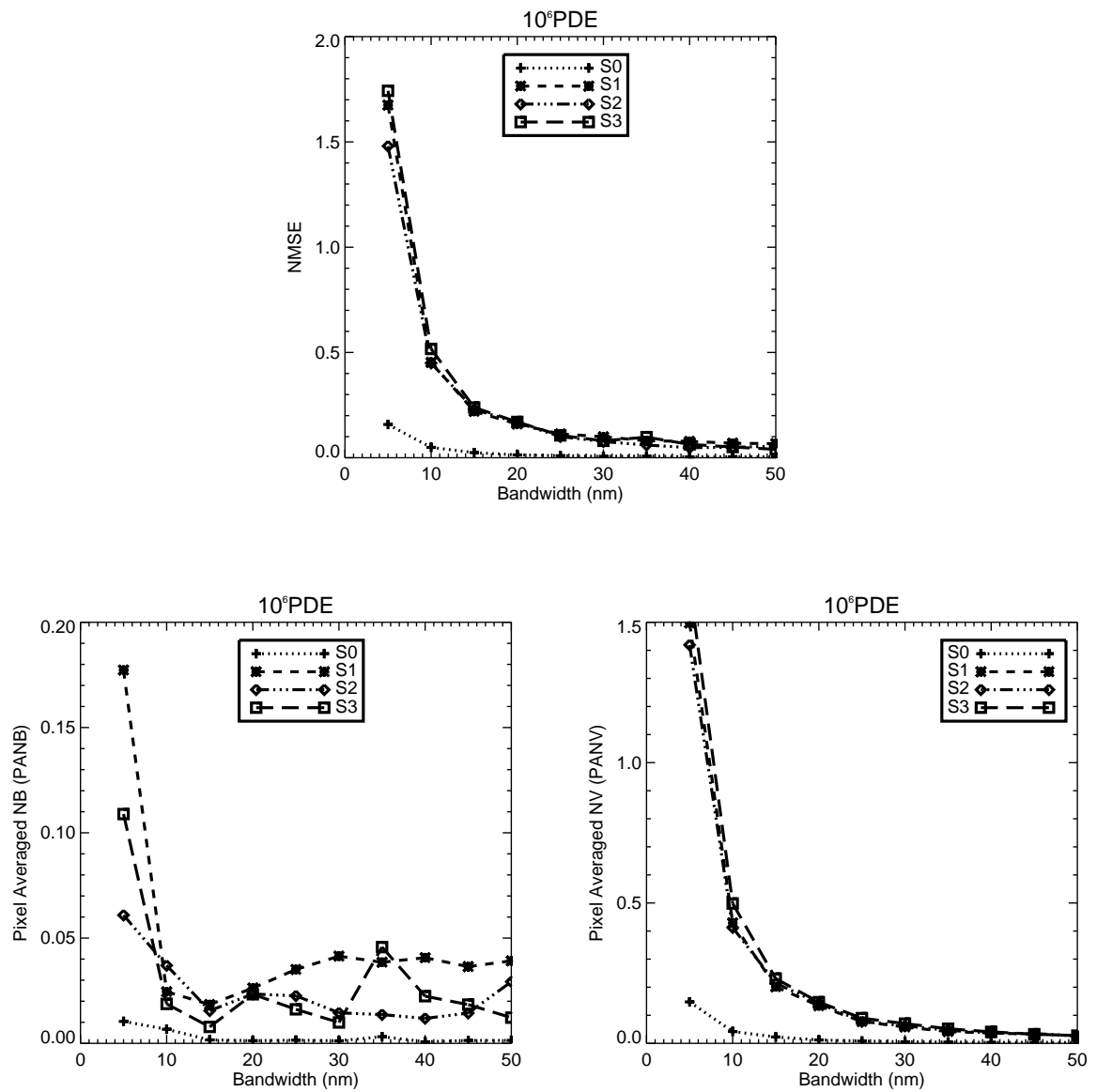


Figure 6.22: Region 1: Normalized MSE, Normalized Bias, and Normalized Variance - 10^6 PDE.

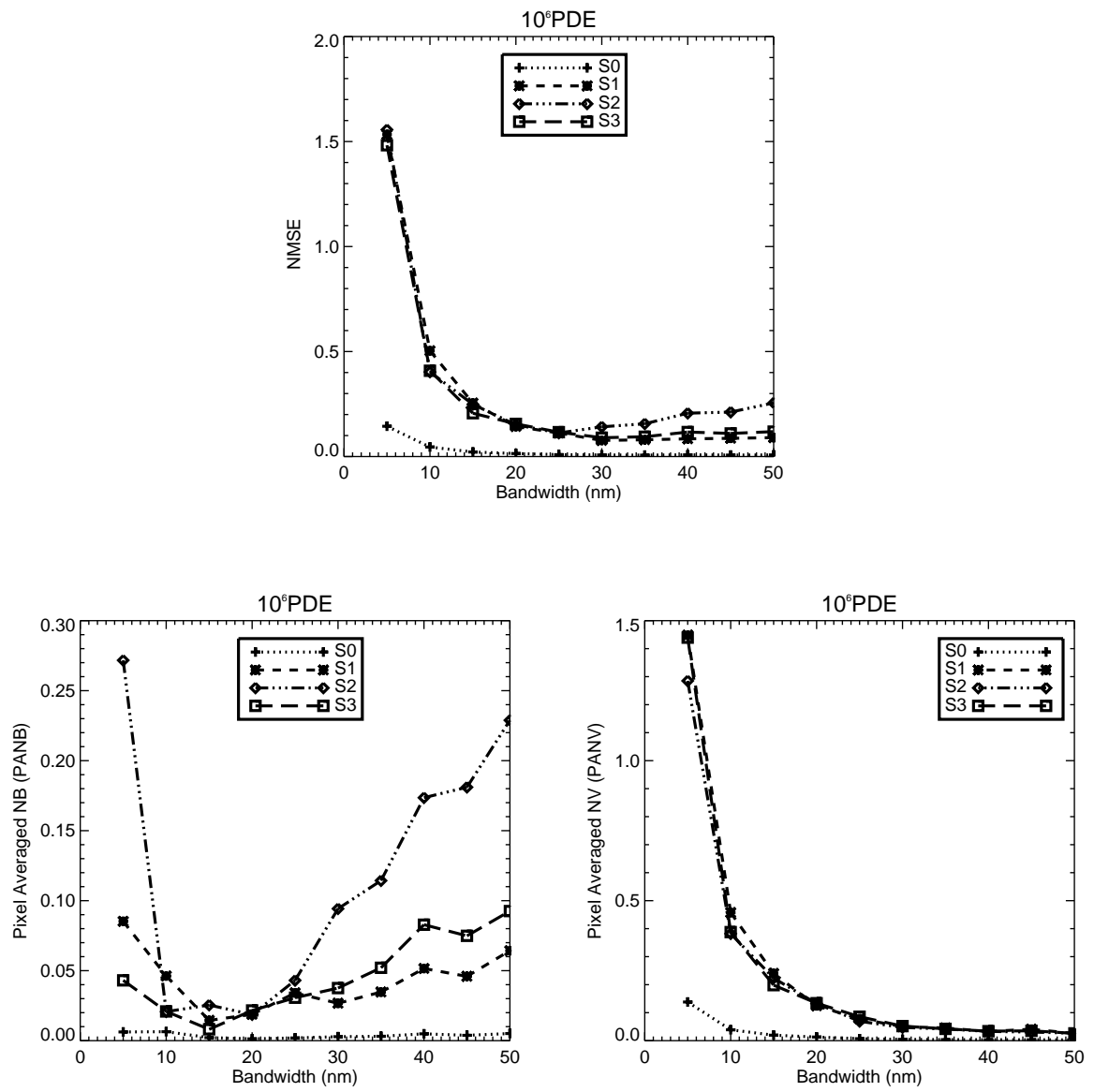


Figure 6.23: Region 2: Normalized MSE, Normalized Bias, and Normalized Variance - 10^6 PDE.

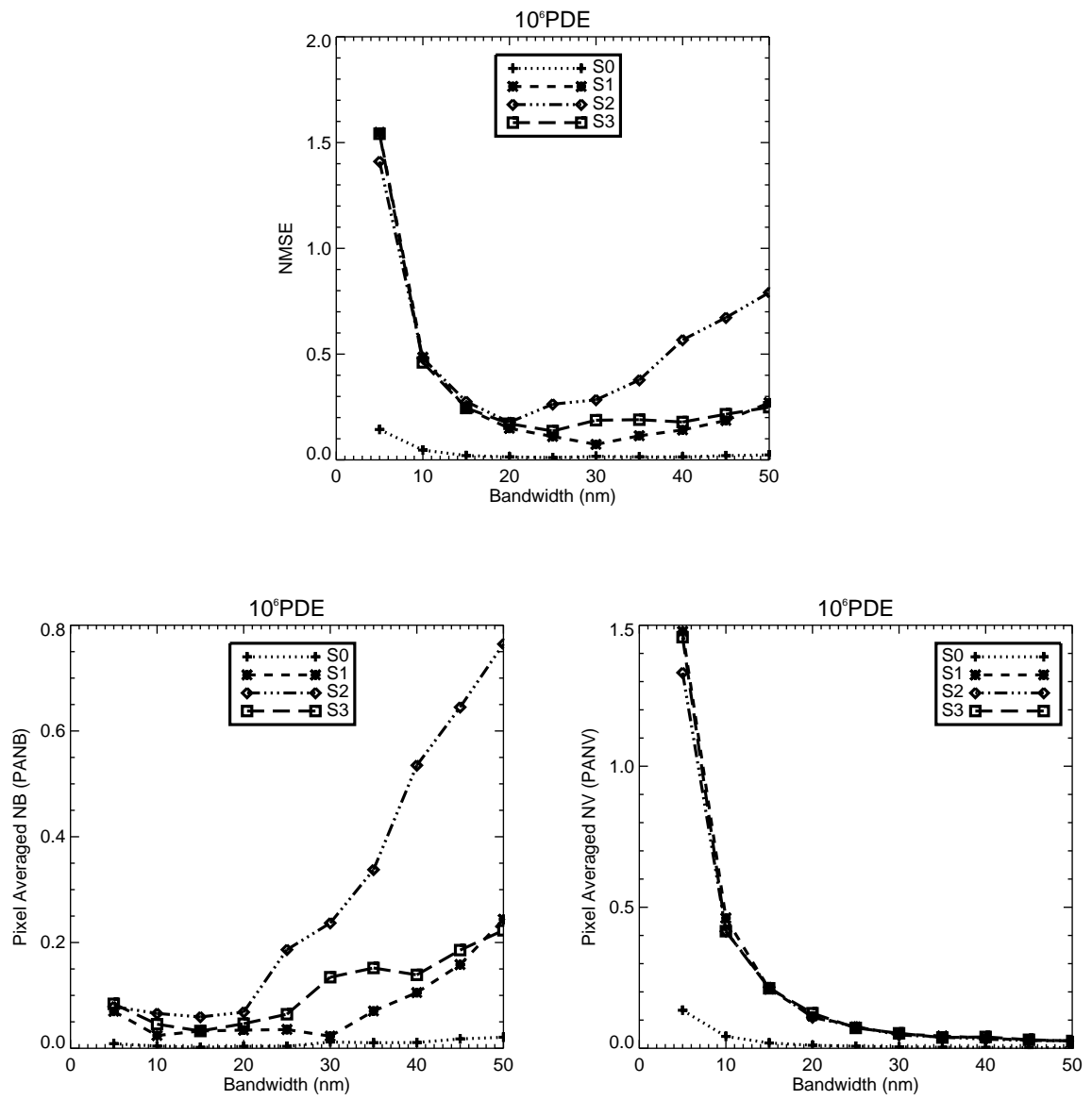


Figure 6.24: Region 3: Normalized MSE, Normalized Bias, and Normalized Variance - 10^6 PDE.

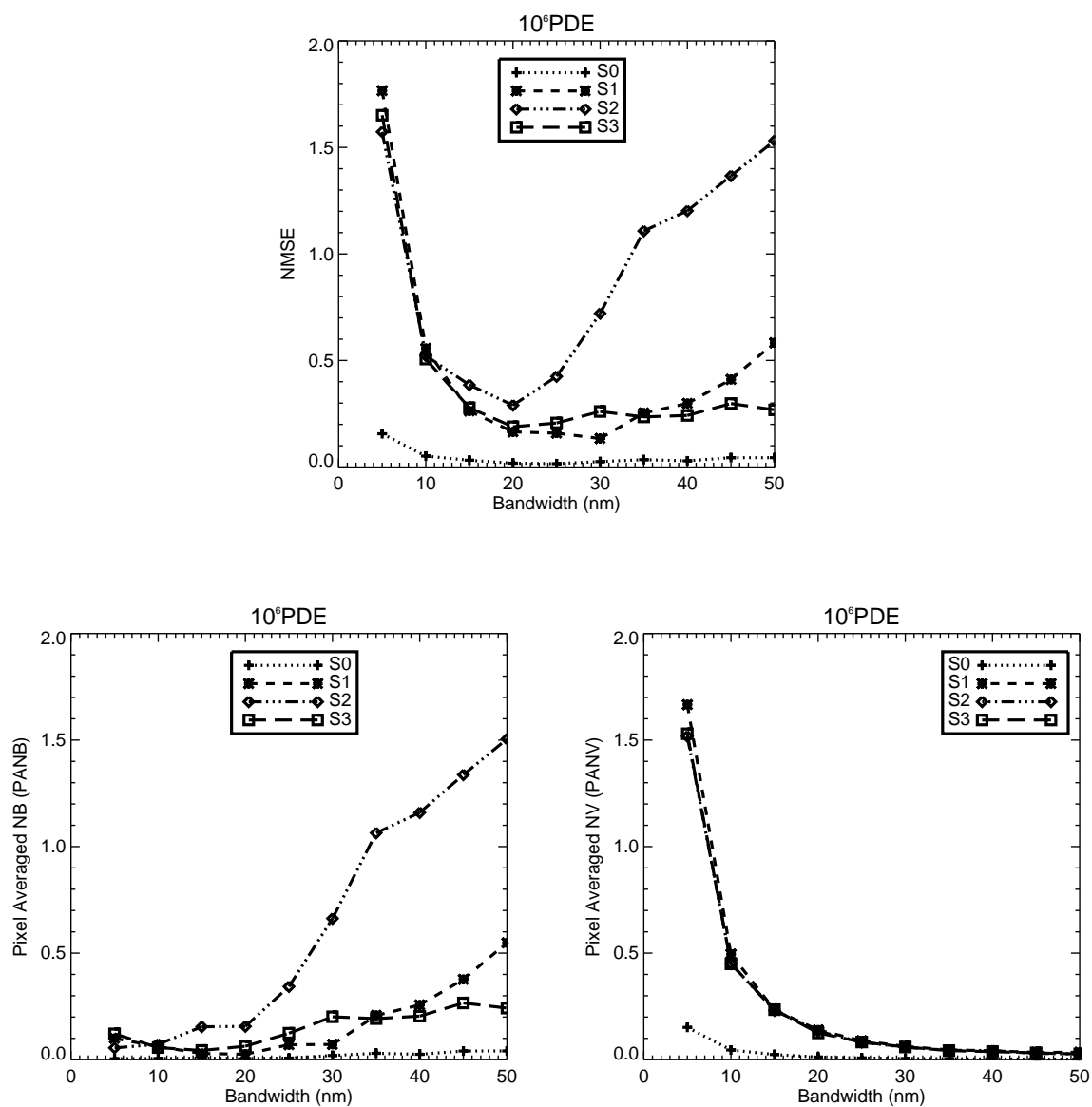


Figure 6.25: Region 4: Normalized MSE, Normalized Bias, and Normalized Variance - 10^6 PDE.

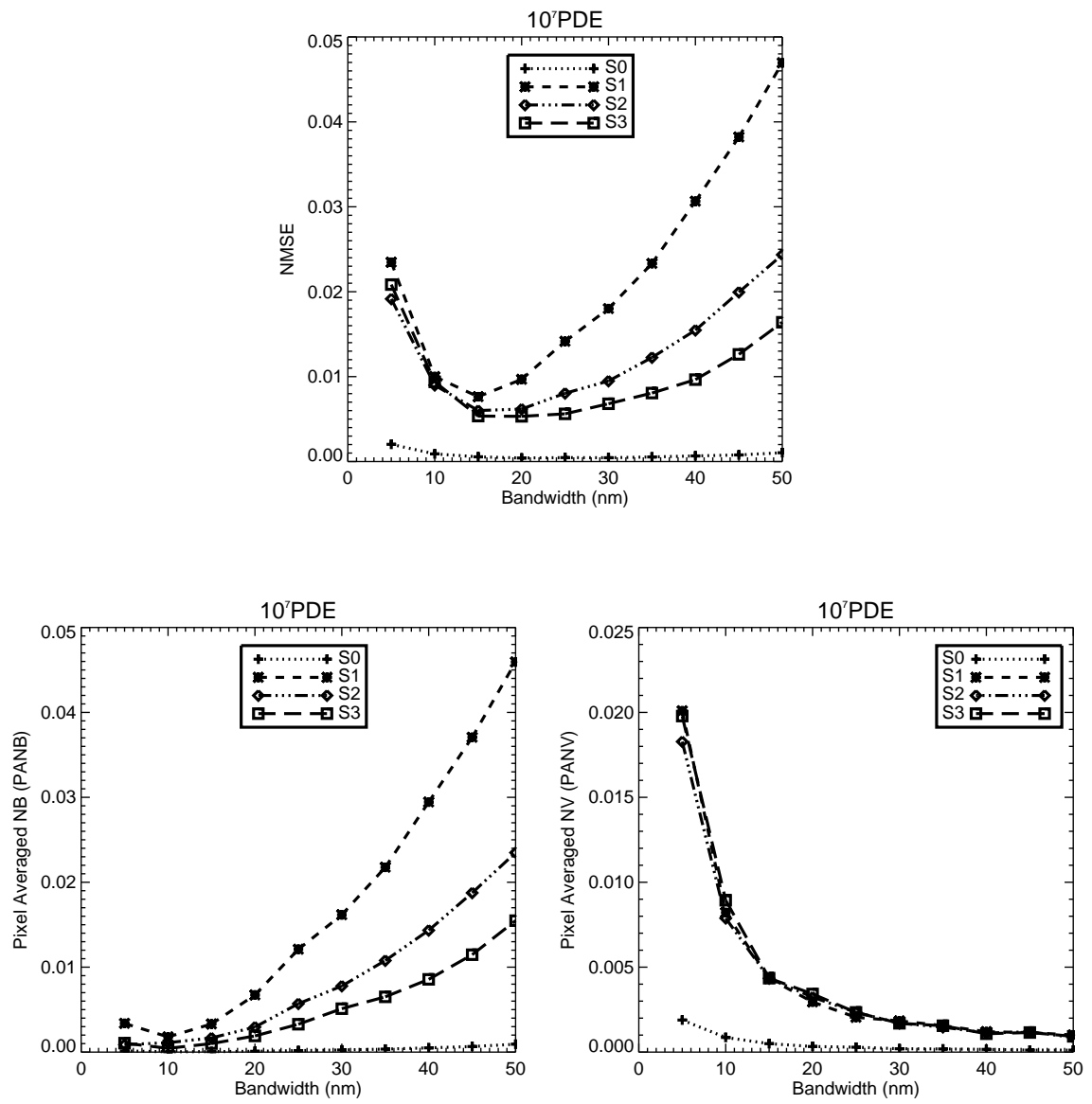


Figure 6.26: Region 1: Normalized MSE, Normalized Bias, and Normalized Variance - 10^7 PDE.

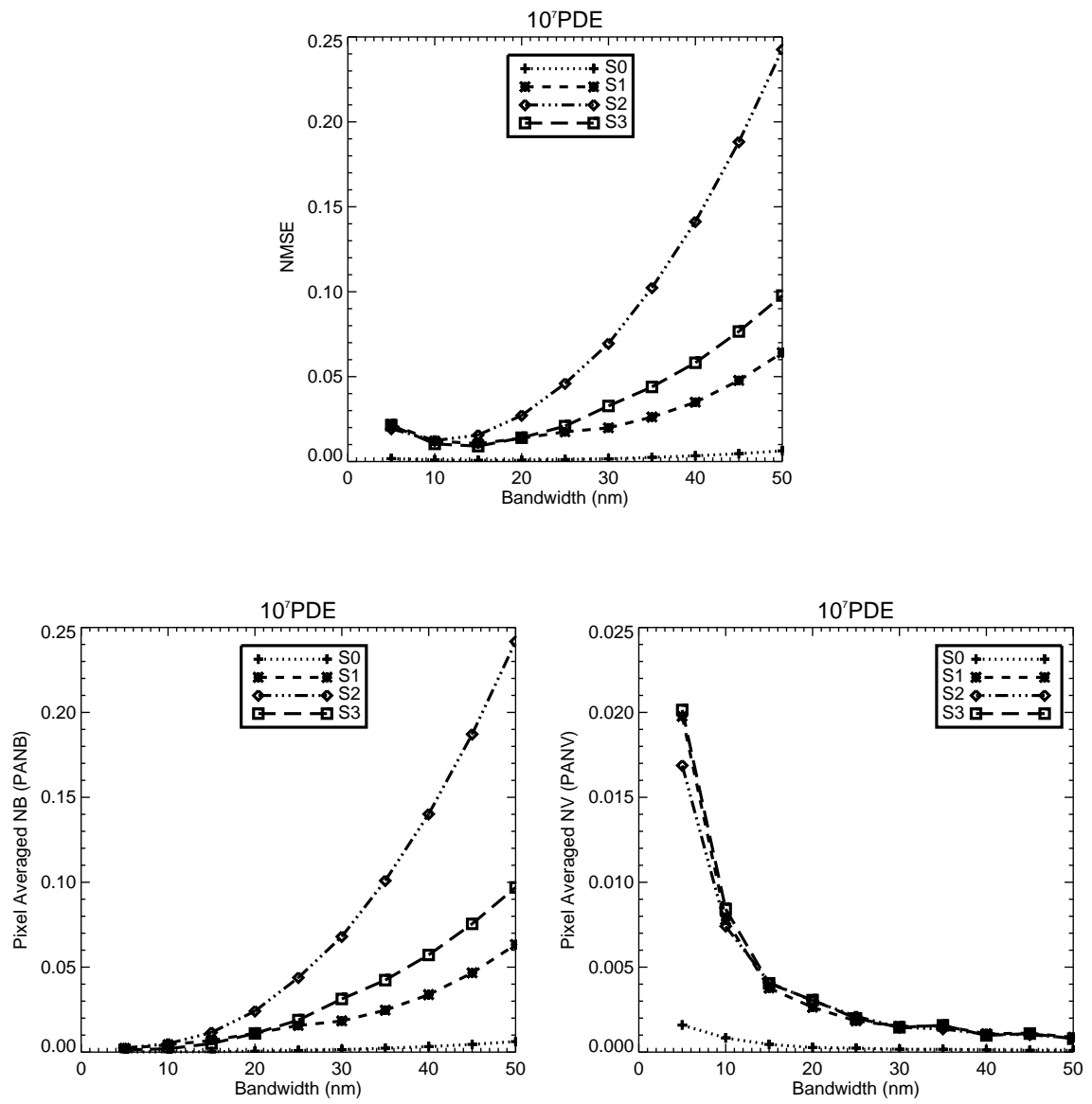


Figure 6.27: Region 2: Normalized MSE, Normalized Bias, and Normalized Variance - 10^7 PDE.

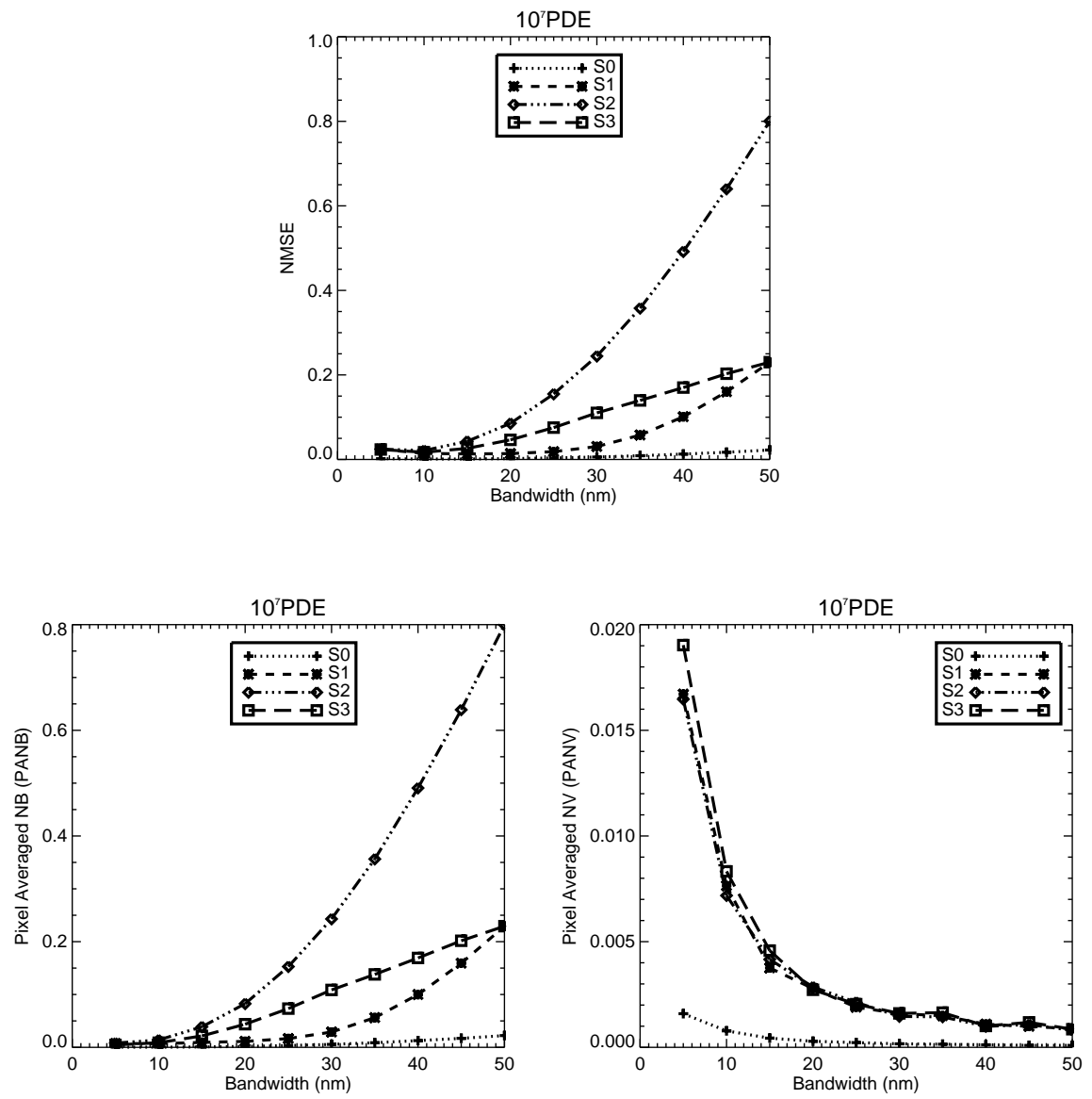


Figure 6.28: Region 3: Normalized MSE, Normalized Bias, and Normalized Variance - 10^7 PDE.

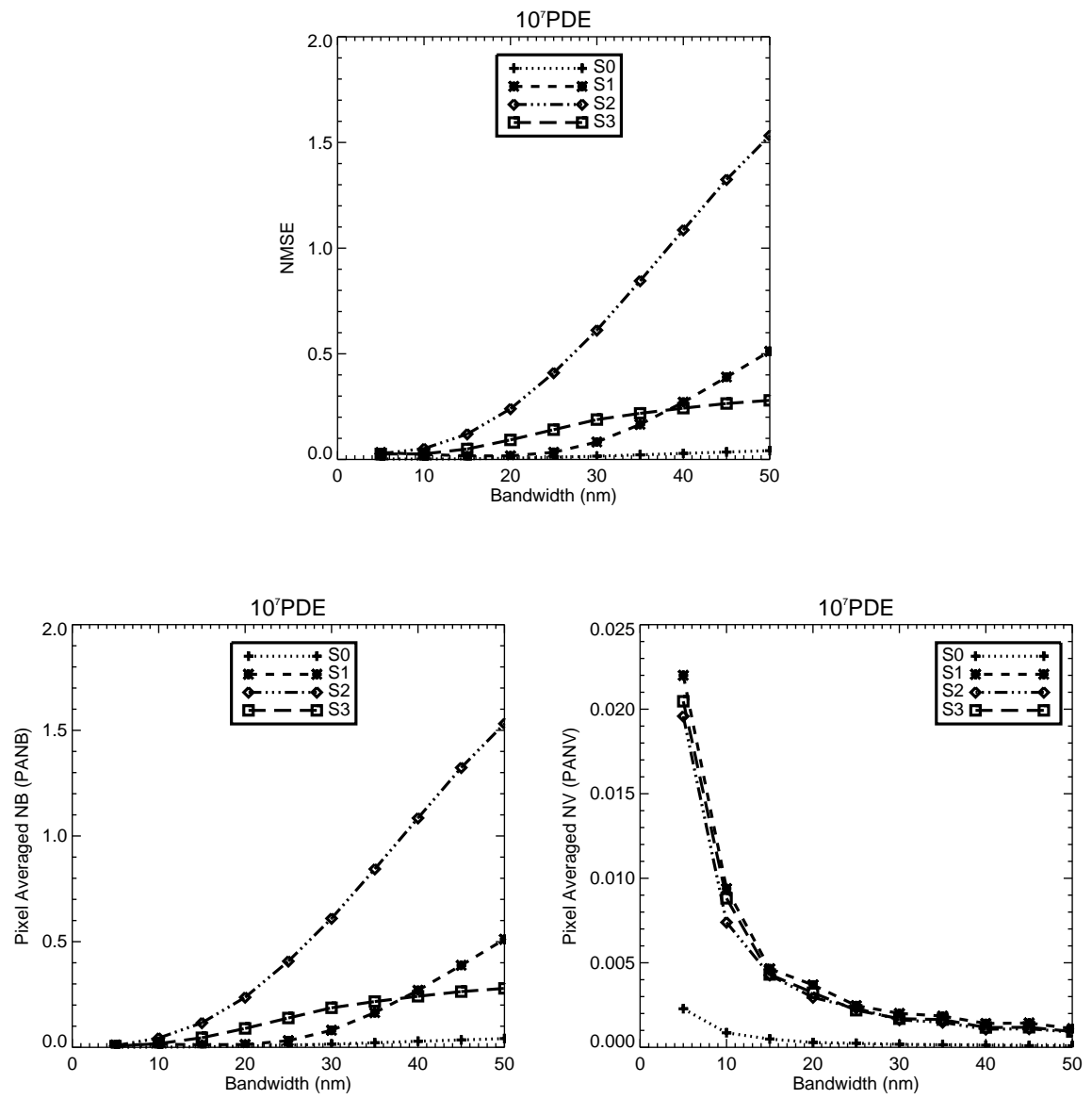


Figure 6.29: Region 4: Normalized MSE, Normalized Bias, and Normalized Variance - 10^7 PDE.

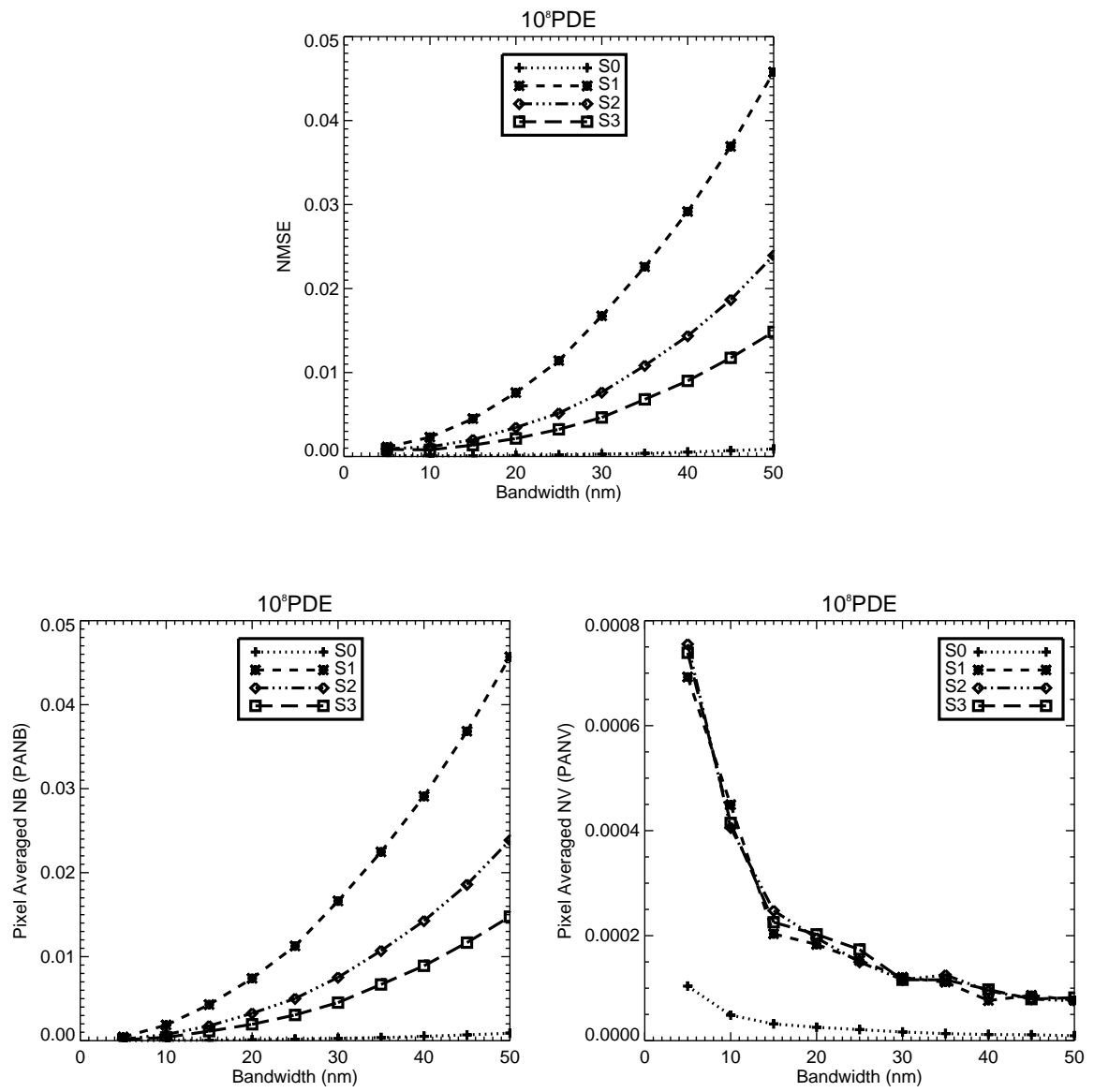


Figure 6.30: Region 1: Normalized MSE, Normalized Bias, and Normalized Variance - 10^8 PDE.

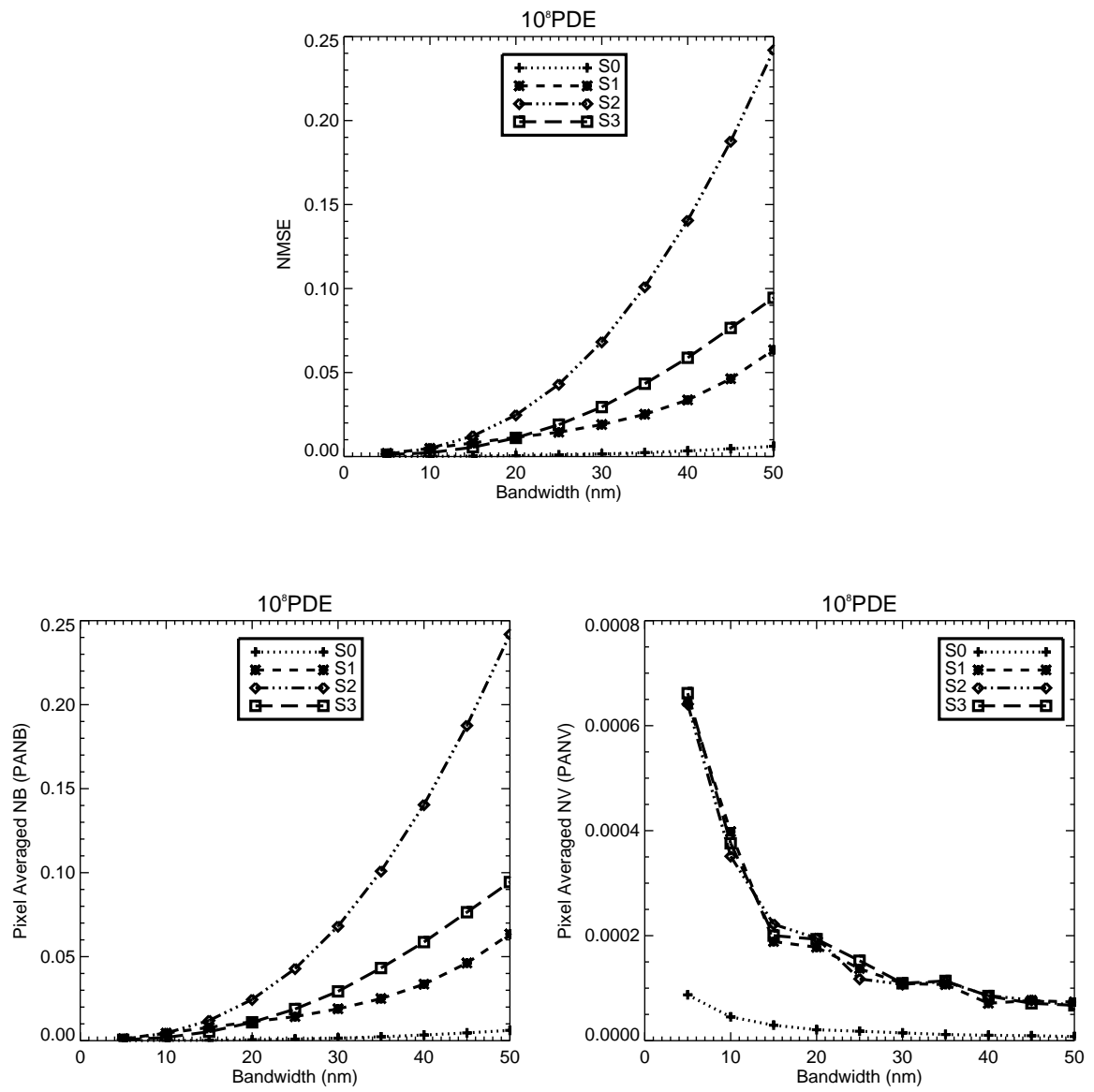


Figure 6.31: Region 2: Normalized MSE, Normalized Bias, and Normalized Variance - 10^8 PDE.

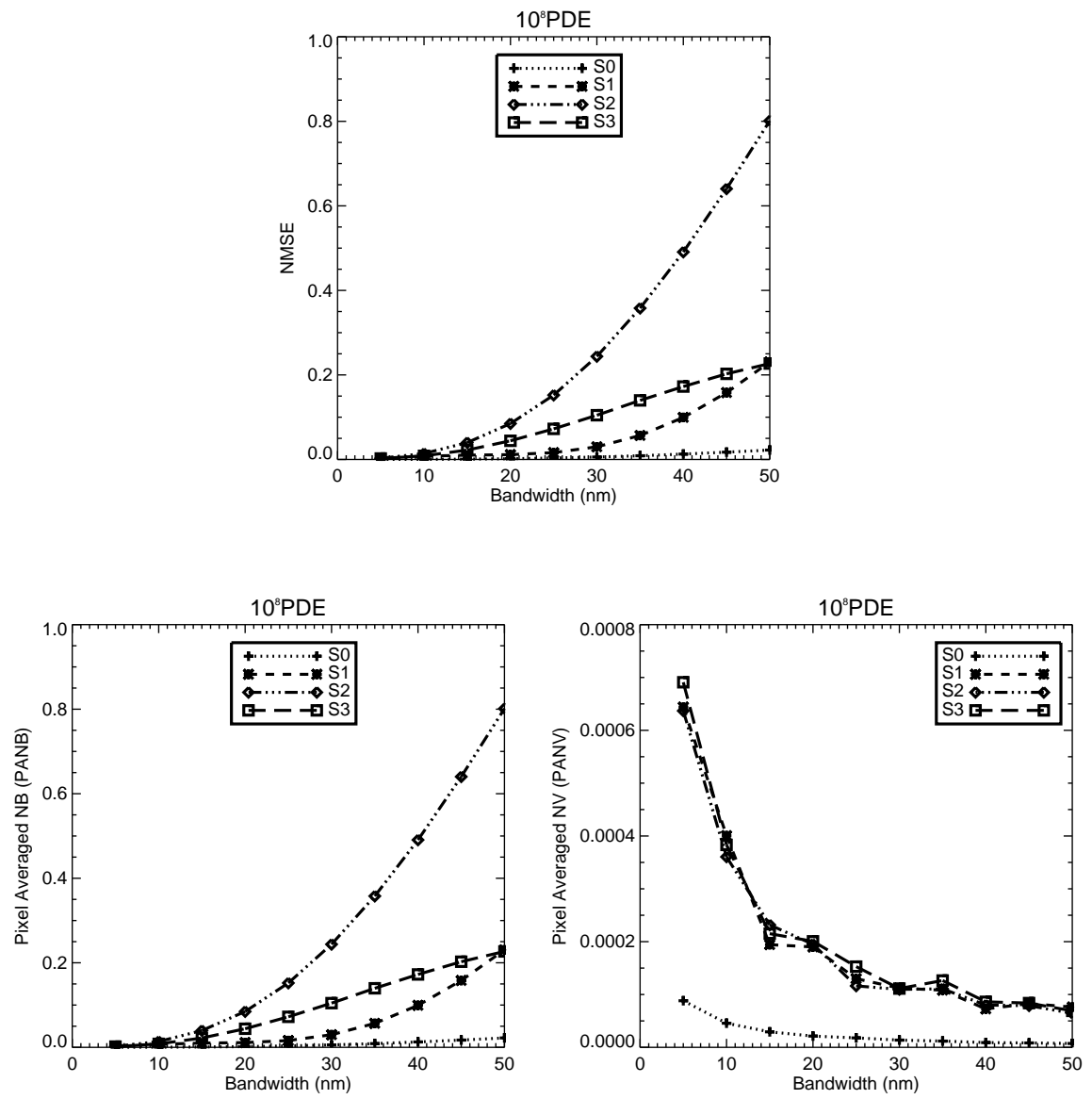


Figure 6.32: Region 3: Normalized MSE, Normalized Bias, and Normalized Variance - 10^8 PDE.

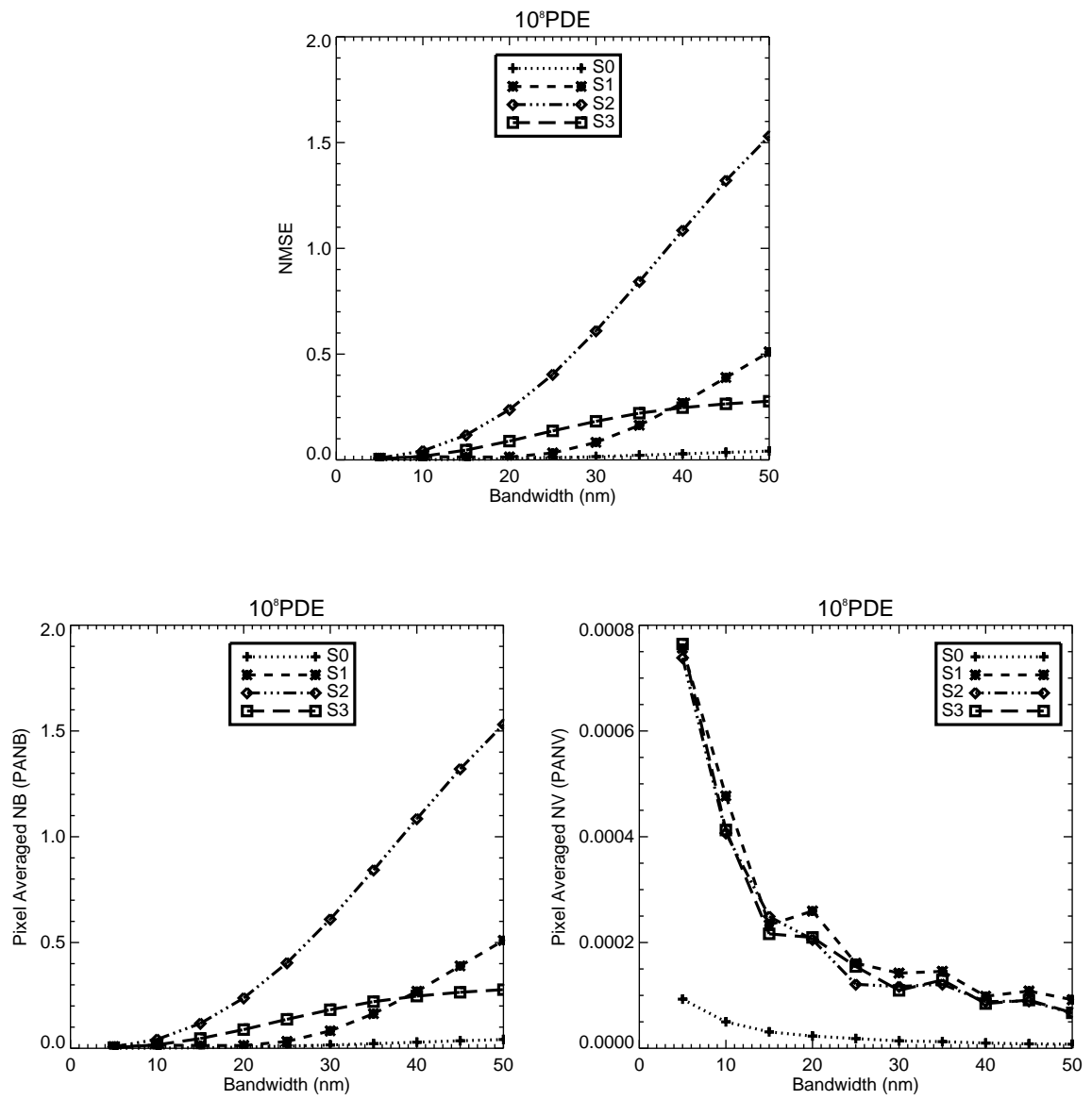


Figure 6.33: Region 4: Normalized MSE, Normalized Bias, and Normalized Variance - 10^8 PDE.

$$PANB = \frac{PAB}{S_i^2}$$

$$PANV = \frac{PAV}{S_i^2}.$$

Where $i = 0, 1, 2$, or 3 . The metrics MSE , PAB , and PAV have been normalized by the true value S_i^2 since the total incident energy in each of the polarization states changes as the transmission width of the bandpass filter is changed. The normalized metrics for Regions 1, 2, 3, and 4 are plotted as a function of the bandwidth for various flat field brightness levels. The brightness levels used - 10^5 , 10^6 , 10^7 , and 10^8 PDE, represent the number of PDE collected over the entire field per nm and per exposure time.

The NB , NV , and $NMSE$ as a function of bandwidth at various brightness levels for Regions 1, 2, 3 and 4 (Figures 6.18 - 6.33) confirms the competing effects of increasing bias due to loss in fringe modulations and decreasing variance due to increased throughput. At a given region in the detector or image plane, and a nominal light level, an optimal transmission width of the bandpass filter exists, which balances the bias and variance effects. For light levels lower than the level yielding an optimum, the decrease in variance dominates the increase in bias as the bandwidth increases and the $NMSE$ decreases monotonically. For light levels higher than the level yielding an optimum, the increase in bias dominates the variance reduction as the bandwidth increases, with a resulting monotonic decrease in $NMSE$. The dominance by bias or variance can be noticed by either the monotonic increase or decrease in $NMSE$ of the Stokes parameters as function of bandwidth.

In Region 1, for cases of object (flat field) brightness 10^5 and 10^6 PDE, the decrease in variance dominates the bias changes resulting a monotonic decrease in $NMSE$ for

all estimated Stokes components with increased bandwidth as seen in Figures 6.18 and 6.22. When the object brightness is at 10^7 PDE a tradeoff between the bias and variance for Region 1 is achieved with a bandpass filter of 15nm (Figure 6.26). An increased source brightness 10^8 PDE causes the bias to dominate the variance changes resulting in a monotonic increase in *NMSE* (Figure 6.30). Region 1 is located at the center of the image plane where the effects of the angular dispersion of the crystal wedges are comparatively minimal. Hence, the *NMSE* has a minimum at a relatively higher energy compared to Regions 2, 3, and 4. For Region 2, the minimum *NMSE* occurs at two source brightness levels - 10^6 and 10^7 PDE , and at bandwidths, 25 nm and 10 nm respectively (6.23, and 6.27). Region 3 exhibits the the minimum *NMSE* at the same source brightness levels as Region 2 at bandwidths 20nm and 10 nm respectively (6.24, and 6.28) while Region 4 exhibits the tradeoff at source brightness level of 10^6 PDE and a bandwidth of 20nm (6.25). The source brightness level of 10^5 PDE causes a monotonic decrease in *NMSE* with increased bandwidth for Regions 2,3, and 4 (Figures 6.19, 6.20, and 6.21). However, Regions 2, and 3 exhibit a monotonic increase in *NMSE* with increased bandwidth at source brightness level of 10^8 PDE (Figures 6.31, and 6.32) while Region 4 shows a similar pattern at two source brightness levels - 10^7 and 10^8 PDE (Figures 6.29 and 6.33). Region 4 is further away from the center of the detector compared to the other considered regions and most likely to be affected by effects of angular dispersion at comparatively low brightness levels. This is confirmed by the monotonic increase in *NMSE* with increased bandwidth at 10^7 and 10^8 PDE source brightness levels (6.29, and 6.33) while Regions 3 and 4 show this pattern at a higher source brightness level of 10^8 PDE (Figures 6.31, and 6.32).

6.3 Sensitivity analysis: Shot noise limited detection

The polarization information in the detector image is in the form of modulations in fringe intensity and the depth of these modulations is ideally equal to the DOP of the input light. As the DOP of the input light decreases the reconstruction of the Stokes components becomes difficult as the fringe modulations are lost against the statistical fluctuations of the detector noise, this happens even for relatively bright sources. These fluctuations can be due to the light-matter interactions from either unpolarized portion of the flux from the source and detector or unpolarized background flux and detector or both. All polarimeters suffer due to noisy measurements and it is essential to perform a sensitivity analysis of the instrument to ascertain its capability to detect polarization information in the presence of noise. The sensitivity of a polarimeter according to [33], is defined as the minimum modulated polarization flux needed to exceed the statistical fluctuations in the flux from the unpolarized background and unpolarized portion of the source. However, in an ISIP, the sensitivity is the minimum DOP required to produce interference fringes statistically distinguishable from noise. In the sensitivity analysis of the ISIP the flux from the source and background is assumed to be constant and the fluctuations are from the light-matter interactions (incident light and detector interactions) and read out process. The cases chosen for the sensitivity study of the ISIP are shot noise limited cases. The reason for this choice is to address a fundamental sensitivity - a sensitivity independent of detector parameters such as readout noise which varies not only with detector technology, cost, cooling, and material but also with readout speed.

A flat field with $\text{DOP} = 1$ and equal amounts of energy in S_1 , S_2 , and S_3 is imaged through the BCA. The total energy in the flat field is adjusted such that the number of PDE per exposure time for a detector with 256×256 pixels is equal to

1.64×10^7 . At this light level used for calculations, the detector the RMS read noise of 5 electrons is negligible relative to shot noise fluctuations. The total variance due to the shot noise and read noise in the detection process are as follows:

$$\textit{Shot noise total variance} = 1.64 \times 10^7$$

$$\textit{Read noise total variance} = 256 \times 256 \times 25 \cong 1.64 \times 10^6$$

$$\textit{Variance ratio} = \frac{\textit{Shot noise total variance}}{\textit{Read noise total variance}} = 10$$

and hence a shot noise limited detection scenario is created. In the first case of sensitivity analysis, the total number of the PDE at the detector is maintained at 1.64×10^7 (constant total energy) and the DOP of the incident flat field is decreased in steps from an initial DOP of 1 to a final DOP of 0.05. In the second case, the total number of photons from the completely polarized flat field is maintained at 1.64×10^7 PDE per exposure time at the detector (constant polarized energy) and the number of the PDE from the background is increased in steps such that DOP of the combination - background and the polarized portion of the incident light, is in the same range ($1 \geq \text{DOP} \geq 0.05$) as that of the former case.

The metric chosen for the sensitivity analysis of the ISIP is the Signal to Noise Ratio (SNR). The SNR for a Stokes component estimator \tilde{S}_i of some Stokes component S_i , $i = 1, 2$ or 3 can be written as follows ([62]):

$$SNR_{\tilde{S}_i} = \frac{\langle \tilde{S}_i \rangle}{\left[E \left\{ (\tilde{S}_i - \langle \tilde{S}_i \rangle)^2 \right\} \right]^{\frac{1}{2}}} = \frac{\langle \tilde{S}_i \rangle}{\sqrt{\sigma_{\tilde{S}_i}^2}} \quad (6.4)$$

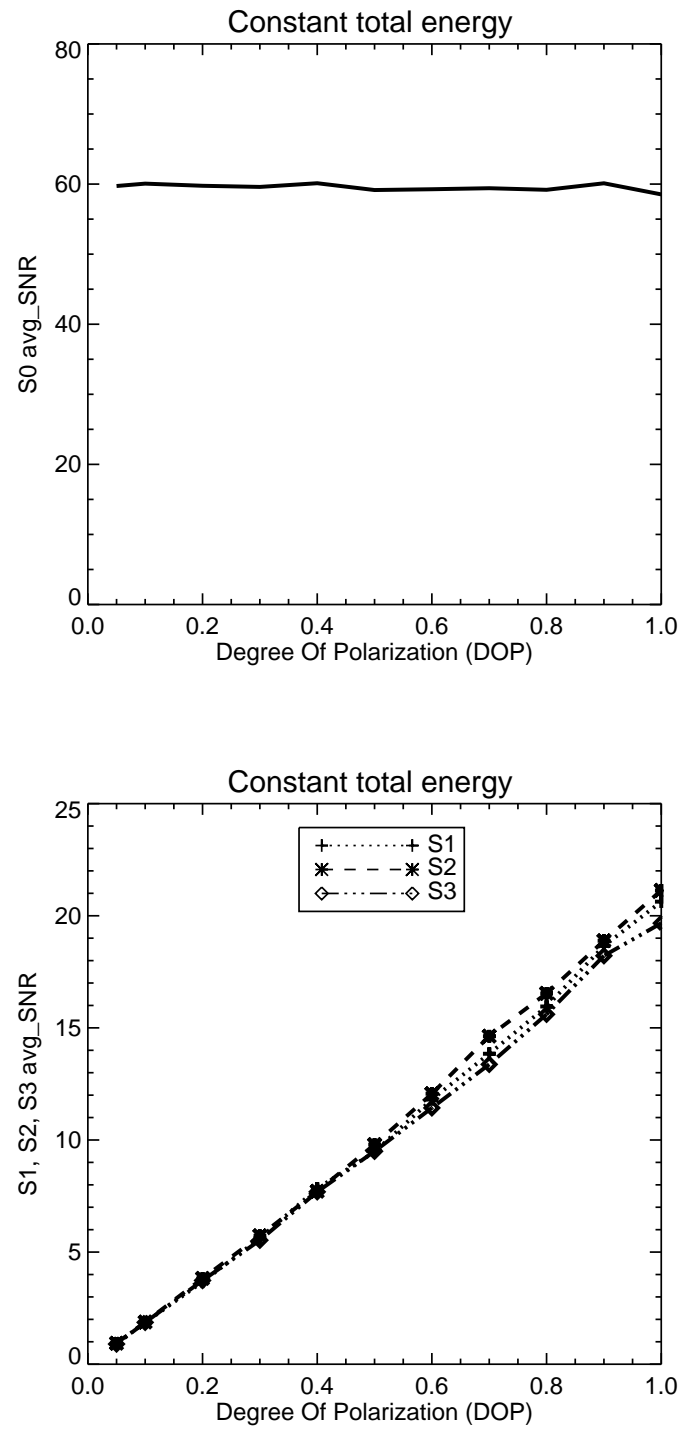


Figure 6.34: Signal to Noise Ratio (SNR) as a function of source DOP (shot noise limited case).

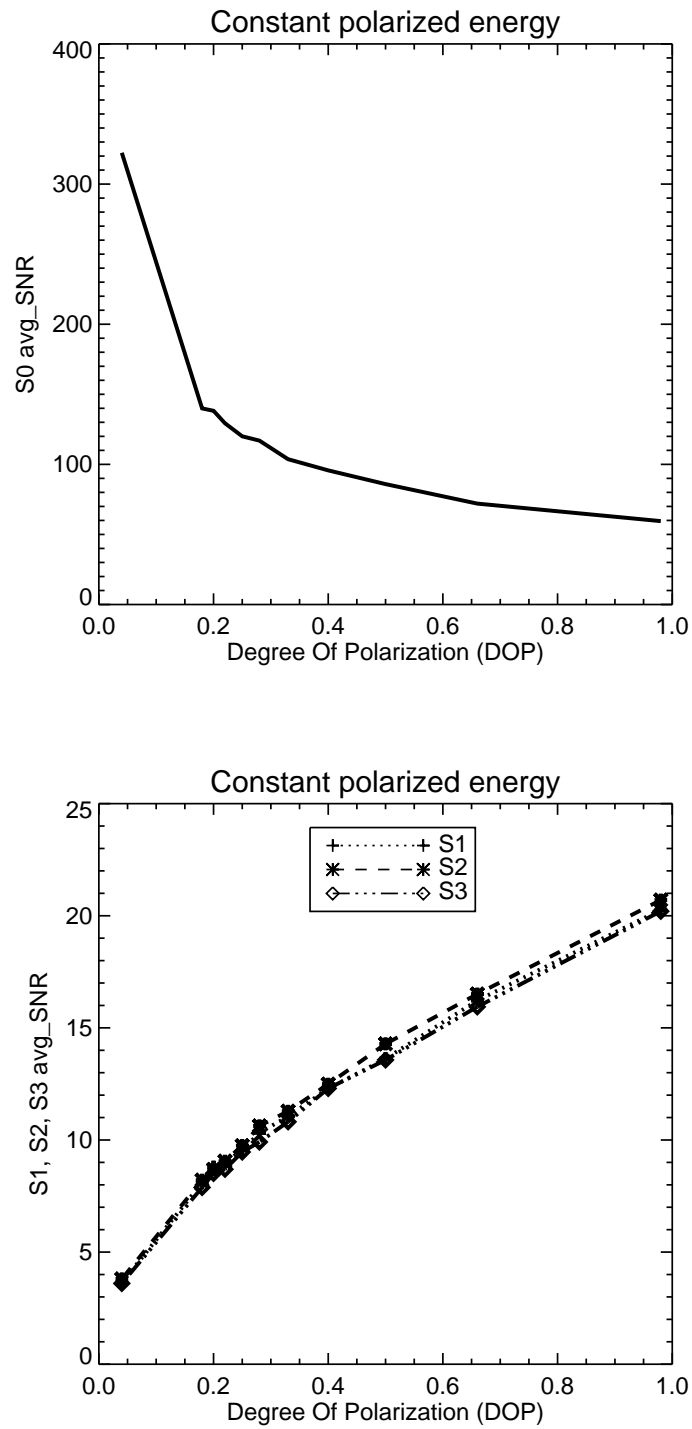


Figure 6.35: Signal to Noise Ratio (SNR) as a function of change in DOP due to unpolarized background (shot noise limited case).

where $\langle \tilde{S}_i \rangle$ is the expected mean value of \tilde{S}_i , $\sigma_{\tilde{S}_i}^2$ is the variance, $E(*)$ indicates the expectation operator.

Sensitivity analysis does not involve any bias-variance tradeoff study since there is not any bias to consider as only narrow-band, effectively monochromatic illumination is used in the simulations. In this case, the fringe visibility is not a function of field angle, because there is effectively no dispersion. The fringe modulated image of the polarized flat field is corrupted with 100 different realizations of shot noise and read noise to form a stack of 100 noise corrupted images. The Stokes images are reconstructed for every noise corrupted image in the stack with a 3 X 3 unit cell (minimum required unit cell size) and the estimated images are then used to evaluate SNR as in Equation 6.4 for every detector pixel. The evaluated SNR is then averaged over all the estimated pixels to form avg_SNR for each of the Stokes components and the entire process is repeated for various DOP settings for both unpolarized background and partially polarized source cases. Figures 6.35 and 6.34 shows the avg_SNR variations with DOP for the individual Stokes components in the unpolarized background and partially polarized source cases respectively.

As seen in Figures 6.35 and 6.34, for $DOP > 0.6$ the SNR of estimations for the S_1, S_2 , and S_3 components are linear. For cases of a) unpolarized background is added and b) DOP is decreased, the SNR drops significantly - $\cong 5$ (unpolarized background) , and $\cong 2$ (partially polarized source), from an initial value of about 20 for the Stokes components \tilde{S}_1, \tilde{S}_2 , and \tilde{S}_3 when the DOP is reduced from unity to 0.1. The ISIP is more sensitive for the Constant Polarized Energy (CPE) case at all DOP but the sensitivity rolls off more severely at low DOP than the Constant Total Energy (CTE) case. Both CPE and CTE behave linearly until a $DOP = 0.5$ or so. The drop in SNR is due to the fluctuations from the background and unpolarized portion of the source.

As the unpolarized flux of the source is increased the overall polarization decreases resulting in fringes with reduced modulation depth or visibility (< 1). The shot noise fluctuations from unpolarized flux follows Poisson statistics and the variance of the fluctuations increases as a square root of the incident unpolarized energy. Hence, an increase in unpolarized portion of the incident energy of the source is accompanied by a simultaneous decrease in fringe modulation of the polarized flux and increase in shot noise fluctuations. This results in reduced SNR in the Stokes estimations of incident light with low DOP as the fringe modulations are lost in the shot noise fluctuations from the unpolarized portion of the incident light. However, the SNR in the estimation of the Stokes component S_0 remains constant with changes in DOP in the partially polarized source case.

When the unpolarized flux from the background is increased the depth of the fringe modulations remains constant. However the magnitude of the shot noise fluctuations from the unpolarized background increases making the fringe modulations less detectable. This results in reduced SNR in the Stokes estimations S_1, S_2 , and S_3 of incident light with decreasing DOP. However an increased amount of overall energy increases the SNR in the S_0 estimation with decrease in DOP.

as the total incident energy is constant and shows an increase with decrease in DOP in the unpolarized background case. This increase of S_0 SNR with decreasing DOP in the latter case is due to the increase in unpolarized energy from the background and a constant polarized energy from the source which results in an overall increase in the total incident energy.

6.3.1 Design Considerations

Another important consideration in the sensitivity of the ISIP is the design of the BCA. Design parameters such as the orientation of the fast axis in the uniaxial crys-

tal wedges of the SVR and transmission axis of the linear polarizer determines the shapes of the calibration fringes and its modulation depth. These parameters have to be chosen in a way that the calibration fringe shapes for horizontal, 45° , and RHC polarization states are as different as possible from each other. The reconstruction algorithm must be able to uniquely identify these polarization states from their corresponding fringe patterns. Another important consideration in the design of the BCA is the visibility or modulation depth of the fringes produced for various input polarization states. An ideal design would produce fringe patterns with visibility = 1 for all input polarization states of $\text{DOP} = 1$. The modulation depth of the fringe patterns, and noise level in the detection process determine the sensitivity of the ISIP. The modulation depth must be approximately equal to the DOP of incident light for the ISIP to have the optimal sensitivity. The sampling requirements in the previous chapters have been assumed to be met in this discussion.

With the orientation of the analyzer transmission axis with respect to the x axis fixed, one way to choose the fast axis orientations of retarders that give optimal sensitivity is to calculate the ratio of the inner product of the vectors formed from the unit cell pixel measurements of two calibration fringe images to the product of their individual modulation depths. The value of this ratio for various combination of retarder angles forms a surface known as the ratio surface. The value at any point on on this surface is a function of the retarder angles used. Since the reconstruction algorithm requires three calibration fringe images - horizontal, 45° , and RHC, a total of three ratio surfaces one for each combination of calibration fringe images can be calculated for various retarder angle settings. Choosing the fast axis orientations for SVR 1 and SVR 2 based on the minimum value of the product of the ratio surface can be used to design the BCA. For each SVR, the choice of fast axis orientation in the front wedges fixes the fast axis orientation in the rear wedge completing the SVR.

This is due to the construction requirement that the fast axis orientation in the rear wedge must orthogonal with respect to the front wedge's fast axis orientation. This means that although there are four retarder wedges in the two SVR assemblies, there are only two free design parameters. All fast orientations discussed here are with respect to x axis. The following methodology is suggested as a starting point towards an optimal design for users who wish to design a desired BCA for an ISIP:

$$R_1 = \frac{\overrightarrow{U_H} \cdot (\overrightarrow{U_{45}})^T}{V_H \times V_{45}}$$

$$R_2 = \frac{\overrightarrow{U_{45}} \cdot (\overrightarrow{U_{RHC}})^T}{V_{45} \times V_{RHC}}$$

$$R_3 = \frac{\overrightarrow{U_H} \cdot (\overrightarrow{U_{RHC}})^T}{V_H \times V_{RHC}}$$

where $\overrightarrow{U_H}$, $\overrightarrow{U_{45}}$, and $\overrightarrow{U_{RHC}}$ are the vectors constructed from the horizontal, 45°, and RHC calibration unit cells. V_H , V_{45} , and V_{RHC} are the visibility values of the horizontal, 45°, and RHC calibration fringes. R_1 , R_2 , and R_3 represent the ratio surfaces formed from horizontal and 45°, 45° and RHC, and horizontal and RHC calibration fringe data.

$$Norm\ R_1 = \frac{R_1}{Max(R_1)}$$

$$Norm\ R_2 = \frac{R_2}{Max(R_2)}$$

$$Norm\ R_3 = \frac{R_3}{Max(R_3)}$$

$$R = \text{Norm } R_1 \times \text{Norm } R_2 \times \text{Norm } R_3$$

Where $\text{Norm } R_1$, $\text{Norm } R_2$, and $\text{Norm } R_3$ represent the normalized ratio surfaces formed from ratio surfaces R_1 , R_2 and R_3 respectively. R is the surface formed from the product of individual normalized ratio surfaces.

$$\text{Fast axis angle 1} = x \text{ coordinate of } \text{Min}(R)$$

$$\text{Fast axis angle 2} = y \text{ coordinate of } \text{Min}(R)$$

where Fast axis angle 1 and Fast axis angle 2 are the fast axis orientations in the front wedges of SVR 1 and SVR 2.

Another way of choosing the retarder angles that give the maximum modulation over the largest range of input polarization angles. The BCA with the retarder angles chosen should provide maximum modulation for input light ($\rho = 1$) of all possible polarization orientations. The BCA configuration used in this work has retarder angle1 = 30 degrees and retarder angle 2 = 150 degrees. The variation of the visibility of the fringes obtained with this BCA configuration for input light ($\rho = 1$) of all possible linear polarization orientations are shown in Figure 6.36. It can be seen that the visibility of the fringes generated for input polarization orientations of 120 and 310 degrees drops to 0.6. The ISIP with this BCA configuration is likely to be sensitive to shot noise fluctuations when it measures incident light with linear polarization orientations close to 120 degrees and 310 degrees with respect to the x axis. The modulation depth of the fringes for these polarization states is relatively small compared to the other linear polarization states. Hence the fringes from the

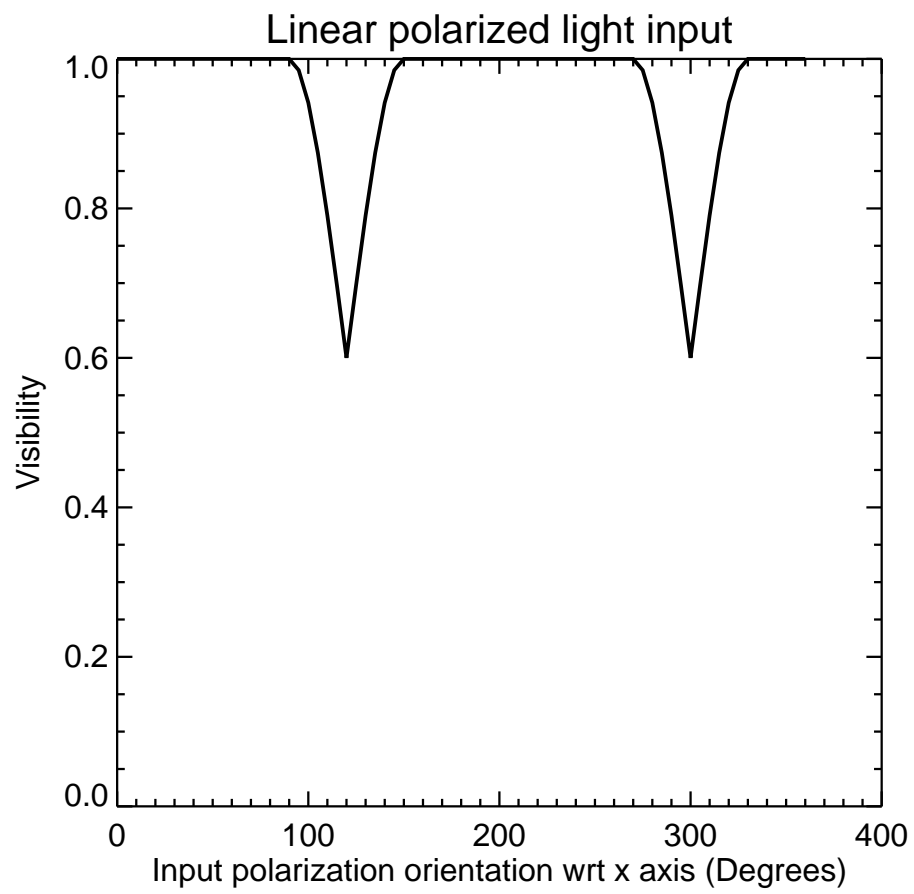


Figure 6.36: Visibility of Fringes obtained for linearly polarized input light.

120 degree and 310 degree input polarization states will be corrupted by shot noise fluctuations at a relatively high and would cause reconstruction errors associated with it to be high compared to other linear input polarization states.

It is shown that the sensitivity of the ISIP is closely related to the design of the BCA. Hence an optimal design procedure for the BCA involving a RMSE metric can be developed as a part of future work to improve the performance of the ISIP.

CHAPTER 7

SUMMARY, CONCLUSIONS, AND RECOMMENDATIONS

Interferometric Stokes imaging is a novel technique with significant potential in polarization measurement applications as it records all the required information in a single image. The appealing features of an ISIP are its compact size, lack of moving parts, and lack of errors from the image misregistration that occur due to beam wander or vibrations in the measuring assembly. An ISIP uses simultaneous imaging technique to record all the polarization information across the scene in form of a fringe modulated image. Mueller calculus is used to write the intensity measurement of the fringe modulated image as a linear combination of the product of input Stokes vector and calibration fringe derived measurement. The assumptions of uniform polarization and intensity of incident light over a unit cell leads to formation of a linear system of equations. The solution of the system of equations is the estimation of Stokes components for a unit cell and this approach is the basic idea for the reconstruction procedure. A slide approach employed for the reconstruction gives multiple Stokes component estimations for the same unit cell and average values are computed. This approach was shown to reduce errors associated with reconstruction at the edges and gave better estimations compared to a discrete reconstruction approach.

The wedge angle of the SVRs are adjusted till the chosen pixel size in the detector Nyquist sampled the calibration fringes. With the pixels Nyquist sampling the calibration fringes, the measurement matrices formed with 2×2 unit cells are found to unsuitable for reconstruction due to the presence of high condition numbers and the minimum sized unit cell size required is established to be 3×3 . The PSF spread of

the fore-optics and the importance of Nyquist sampling it with the unit cell is shown with a point source imaging example.

Bias-variance tradeoff approach by varying the unit cell size is used to obtain a minimum MSE in the presence of noise. The optimal unit cell size required for reconstruction is shown to depend on the SNR and size of the polarization domain. A similar study is used to analyze the effects of bandwidth and illumination changes on the reconstruction error at various regions of the detector field. It is shown that the optimal choice of the bandpass filter depends on the location of the polarization domain with respect to the detector field and brightness of the source. Finally, a sensitivity analysis is done for a shot noise limited detection scenario and found that the SNR in the estimated Stokes images decreased significantly at low degrees of polarization. The fringe modulations of a source becomes less detectable due to the shot noise fluctuations from the increased flux from the unpolarized background or the unpolarized portion of the source.

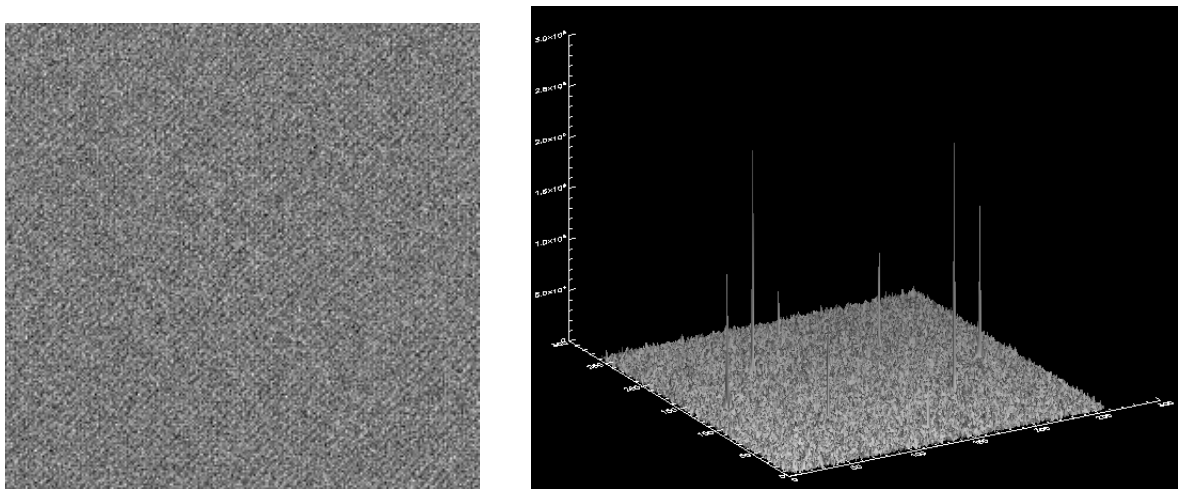
Although the ISIP shows a lot of promise in remote sensing and bio science applications there are a few inherent disadvantages associated with it. First, the beam splitting at the wedge plane of the SVRs results in a loss of spatial resolution in the detected image ([63]). The second and the most important disadvantage of the ISIP is its inability to measure polarization due to loss in visibility of the fringes under broad band illumination. Consequently, a bandpass filter is required to be used which causes a further reduction in the throughput of the system apart from the reduction from the linear polarizer used in the ISIP. Finally, the precision required for the small wedge angles and physical dimensions of the birefringent crystals forming the SVRs makes the fabrication process difficult.

The loss in spatial resolution issue has been addressed and the SVRs in the ISIP have been replaced by Savart plates ([39]). However, this system still suffers from the

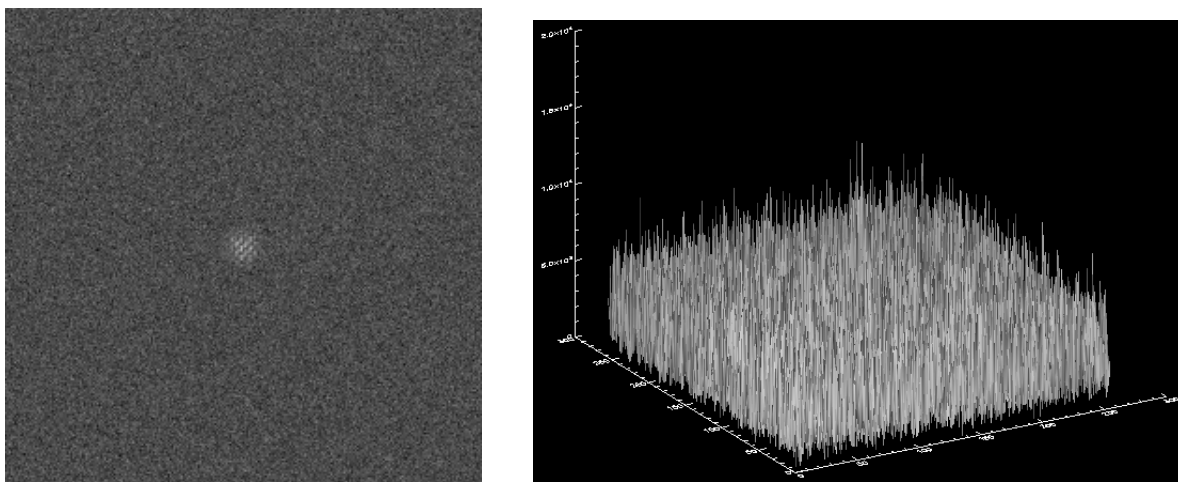
loss of fringe visibility when used under broad band illumination conditions. Replacement of the Savart plates with diffraction gratings to obtain a dispersion compensated polarization Sagnac interferometer (DCPSI) has improved the interferometric polarimetric detection capabilities under broad band illumination ([37]) The DCPSI uses a snapshot technique and is capable of measuring either S_1 and S_2 or S_2 and S_3 under white light illumination.

Based on this work it is inferred that the main problem of the use of ISIP in remote sensing applications is its sensitivity. The shot noise fluctuations from the unpolarized flux - either from the back ground or unpolarized portion of the source or both, corrupts the fringe modulations at low degrees of polarization. This limits the use of the ISIP to applications where the flux from the background is not significant and the light from the scene or object being measured has a high . Hence with the current design, instrumentation, and reconstruction approach the use of ISIP for making polarization measurements would most likely benefit applications in active polarimetry.

Modifications in the existing design, addition of new components, and a change in reconstruction approach can improve the SNR in the Stokes estimations from the fringe modulated image of the ISIP. The use of SVRs with achromatic wedges, dispersion correctors, optimal bandpass filter, and image intensifier in front of the detector are the recommended changes in the ISIP configuration that needs investigation. The SNR in the estimated Stokes images may increase if a Fourier domain approach is employed especially in reconstruction of fringe modulated images at low degrees of polarization. This recommendation is made considering the possibility of noise energy being lower than the fringe energy at the spatial frequencies encoding the polarization information. Figure 7.1 illustrates the potential cases that can benefit from each of the reconstruction approach. The Stokes estimations from the



(a) Flat field with $\sigma = .05$ and DC component removed in the Fourier domain.



(b) Noisy point source image with $\sigma = 1$.

Figure 7.1: Potential uses of Fourier approach and Slide reconstruction spatial approach.

Slide approach for noisy flat field fringe modulated image (Figure 7.1a) formed with a beam of light equally polarized in S_1 , S_2 and S_3 was found to have a SNR of $\cong 1$ in Figure 6.34. However, the Fourier domain of the noisy flat field image in Figure 7.1a reveals significant fringe power at spatial frequencies that encode polarization information that can be possibly used to generate Stokes estimations of higher SNR (> 1) with a Fourier reconstruction approach. Similarly, the Fourier domain of a point source image formed with equal polarization in S_1 , S_2 and S_3 (Figure 7.1b), corrupted with noise, reveals the lack of fringe power at the same spatial frequencies. However, Stokes reconstruction of this noisy point source is possible with the spatial domain reconstruction approach as shown in Chapter 6. Thus the development of a Fourier transform based Stokes estimation algorithm along with the existing spatial approach can increase reconstruction capabilities for a wide range of polarization scenarios.

Another important application that needs investigation is the use of ISIP to measure polarization of spatially coherent objects which would require a comprehensive development of the Jones model. Such a development would enable the study of interference effects from the different spatial regions of the object at the detector plane and the reconstruction issues associated with it.

REFERENCES

- [1] J.Scott Tyo, Dennis L. Goldstein, David B.Chenault, and Joseph A. Shaw, “Review of passive imaging polarimetry for remote sensing applications”, *Applied Optics* **45** (22), 5453-5469 (2006).
- [2] Gareth D.Lewis, David L. Jordan, and Eric Jakeman, “Backscatter linear and circular polarization analysis of roughened aluminium”, *Applied Optics* **37** (25), 5985-5992 (1998).
- [3] John Stryjewski, Dan Hand, David Tyler, Sukumar Murali, Mike Roggeman, Nick Peterson, “Microfacet Scattering Models for Pulse Propagation Ranging”, submitted to Advanced Maui Optical and Space Surveillance Technologies Conference, (2010).
- [4] K.Oka, J. Ikeda, Y.Ohtsuka, “Novel polarimetric technique exploring spatio temporal birefringent response of an anti-ferroelectric liquid crystal cell”, *Journal of Modern Optics* **40** (9), 1713-1723 (1993).
- [5] K.Oka and Y.Ohtsuka, “Polarimetry for Spatiotemporal Photoelastic Analysis”, *Experimental Mechanics*, 44-48 (1993).
- [6] J.S.Tyo. M.P. Rowe, E.N. Pugh, Jr., and N.Engheta, “ Target detection in optically scattering media by polarization-difference imaging”, *Applied Optics* **35** (11) 1855-1870 (1996).
- [7] L.J.Cheng, J.C.Mahoney, and G.Reyes, “Target detection using an AOTF hyperspectral imager”, *Optical pattern recognition V*, D.P. Casasent and T.Chao, eds., SPIE proceedings **2237**, 251-259 (1994).

- [8] Edward DeHoog, Haitao Luo, Kazuhiko Oka, Eustace L. Dereniak, and James Schiewgerling, "Snapshot polarimeter fundus camera". *Applied Optics* **48** (9), 1663-1667.
- [9] Matthew H.Smith, Jacob B.Woodruff, and James D.Howe, "Beam Wander Considerations in Imaging Polarimetry", *Measurement, Analysis, and Remote Sensing II : SPIE Conference on Polarization* **3754**, 50-54 (1999).
- [10] Christopher M.Persons, David B.Chenault, Michael W. Jones, Kevin D.Spradely, Michael G. Gulley, Craig A. Farlow SY Technology, a division of L3 Communications, Inc., " Automated registration of polarimetric imagery using Fourier transform techniques", *Polarization Measurement, Analysis, and applications V*, SPIE proceedings **4819**, 107-117 (2002).
- [11] Takashi Sato, Takeshi Araki, Yoshihiro Sasaki, Toshihide Tsur, Toshiyasu Tadakoro, and Shojiro Kawakami, "Compact ellipsometer employing a static polarimeter module with arrayed polarizer and wave-plate elements", *Applied Optics* **46**(22), 4963-4967(2007)
- [12] R.M.Azzam, "Extinction of the p and s polarizations of a wave on reflection at the same angle from a transparent film on an absorbing substrate: applications to parallel-mirror crossed polarizers and a novel integrated polarimeter", *Journal of Optical Society of America* **2**(2),189-197 (1985).
- [13] E.V. Spesivtsev, S.V. Rykhlytsky, V.A. Shvets, S.I. Chikichev, A.S. Mardezhov, N.I. Nazarov, and V.A. Volodin, "Time-resolved microellipsometry for rapid thermal processes monitoring", *Thin Solid Films* **455** – **456**, 700-704 (2004).

- [14] J.Scott Tyo, “Hybrid division of aperture/division of a focal-plane polarimeter for real-time polarization imagery without an instantaneous field-of-view error”, Optics Letters **31**(20), 2984-2986 (2006).
- [15] R.M.A. Azzam, “Division-of-wave-front thin-film beam splitter for generating binary patterns of orthogonal elliptical polarization states”, Journal of Optical Society of America, **5**(9), 1576-1580 (1988).
- [16] R.M.A. Azzam, “Division-of-wave-front polarizing beam splitter and half-shade device using dielectric thin film on dielectric substrate”, Applied Optics, **23**(9), 1296-1298 (1984).
- [17] R.M.A. Azzam, “Multichannel polarization state detectors for time-resolved ellipsometry”, Thin Solid Films, **234**, 371-374 (1993).
- [18] J.S.Tyo, “Imaging polarimetry in the LWIR with microgrid polarimeters”, EPJ Web of Conferences **5**, 04009 (2010).
- [19] Bradley M.Ratliff, Charles F.LaCasse, and J.Scott Tyo, “Interpolation strategies for reducing IFOV artifacts in microgrid polarimeter imagery”, Optics Express **17**(11), 9112-9125 (2009).
- [20] J.Scott Tyo, Charles F.LaCasse, and Bradley M.Ratliff, “Total elimination of sampling errors in polarization imagery obtained with integrated microgrid polarimeters”, Optics Letters, **34** (20), 3187-3189 (2009).
- [21] Eric Compain and Bernard Drevillion, “Broadband division-of-amplitude polarimeter based on uncoated prisms”, Applied Optics, **37** (25), 5938-5944 (1998).

- [22] Eric Compain, Bernard Drevillion, Jean Hue, Jean Yves Parey, and Jean Eric Bouree, “Complete Mueller matrix measurement with a single high frequency modulation”, *Thin Solid Films*, **313 – 314**, 47-52 (1998).
- [23] Patrick P.Collins, Brendan Shehan, Michael Redfern, and Andrew Shearer, “Galway Astronomical Stokes Polarimeter ”, *Proceedings of Science*, arXiv:0905.0084v1 [astro-ph.1M] (2009).
- [24] R. M. A. Azzam, “Division-of-amplitude Photopolarimeter (DOAP) for the Simultaneous Measurement of All Four Stokes Parameters of Light”, *Journal of Modern Optics*, **29** (5), 685 - 689 (1982).
- [25] A. Seifter, F. Sachsenhofer, and G. Pottlacher, “ A Fast Laser Polarimeter Improving a Microsecond Pulse Heating System”, *International Journal of Thermophysics*, **23** (5), 1267-1280 (2002).
- [26] Michael W.Kudenov, J.Larry Pezzaniti, Eustace L.Dereniak, and Grant R.Gerhart, “Infrared Stokes imaging polarimeter using microbolometers”, *SPIE Proceedings*, **7419**(741908), 1-12 (2009).
- [27] Jason Mudge, Miguel Virgen, and Peter Dean, “Near Infrared simultaneous Stokes imaging polarimeter”, *Lockhead Martin Advanced Technology Centre*.
- [28] Michael W.Roche, David B.Chenault, Justin P.Vaden, Art Lompado, David Voelz, Timothy J.Schulz, Ryan N.Givens, and Victor L.Gamiz, “Synthetic Aperature Imaging Polarimeter”.
- [29] Erich de Leon, Rebekah Brandt, Adam Phenis and Miguel Virgen, “Initial results of a Simultaneous Stokes Imaging Polarimeter”, *Lockhead Martin Advanced Technology Centre*.

- [30] Alexander Ling, Soh Kee Pang, Antia Lamas-Linares, and Christian Kurt-siefer “An Optimal Photon Counting Polarimeter”, Journal of Modern Optics, arXiv:quant-ph/0511053v2 (2006).
- [31] Michael W.Kudenov, J.Larry Pezzaniti, Eustace L.Dereniak, and Grant R.Gerhart, “2-Cam LWIR imaging Stokes polarimeter”, SPIE proceedings, Polarization: Measurement, Analysis, and Remote Sensing, **6972**(69720k), 1-12 (2008).
- [32] Dennis Goldstein, “Stokes Polarimetry”, *Polarized Light*, Second Edition, Revised and Expanded, Marcel Dekker Inc, New York (2003).
- [33] R.Bellazzini, L.Baldini, A.Brez, E.Costa, L.Latronico, N.Omodei, P.Soffitta and G.Spandre, “A photoelectric polarimeter based on a Micropattern Gas Detector for X-ray astronomy”, Nuclear Instruments & Methods in Physics Research A 510, 176-184 (2003).
- [34] Jay S. Van Delden, “Ortho-Babinet polarization-interrogating filter: an interferometric approach to polarization measurement”, Optics Letters **28** (14), 1173-1175 (2003).
- [35] Jay Scott Van Delden, “ The Babinet compensator”, *Principles and Measurement of Polarized Light: A Novel Interferometric Approach*, PhD dissertation, p.131, Vol.532, College Of Optical Sciences, University Of Arizona (2003).
- [36] Kazuhiko Oka , Toshiaki Kaneko, “Compact complete imaging polarimeter using birefringent wedge prisms”, Optics Express **11** (13), 1510-1519 (2003).

- [37] Michael W. Kudenov, Matthew E.L. Jungwirth, Eustace L. Dereniak, and Grant R. Gerhart, “White light Sagnac interferometer for snapshot linear polarimetric imaging”, *Optics Express* **17** (25), 22520-22534.
- [38] Haitao Luo, Kazuhiko Oka, Edward DeHoog, Michael Kudenov, James Schiewgerling, and Eustace L. Dereniak, “Compact and miniature snapshot imaging polarimeter”, *Applied Optics* **47** (24), 4413-4417.
- [39] Kazuhiko Oka and Naoki Saito. “Snapshot complete imaging polarimeter using Savart plates”, *Proceedings of SPIE* **6295** (629508), 1-6.
- [40] Harrison H. Barrett, and Kyle J. Myers, “Diffraction theory and Imaging”, *Foundations of Image Science*, Wiley Series in Pure and Applied Optics, New Jersey (2004).
- [41] Dennis Goldstein, “The Mueller Matrices for Polarizing Components”, *Polarized Light*, Second Edition, Revised and Expanded, Marcel Dekker Inc, New York (2003).
- [42] William A. Shurcliff, “Standard Mueller Matrices and Jones Matrices”, *Polarized Light*, Harvard University Press, Cambridge, Massachusetts (1962).
- [43] Y.Ohtsuka and K.Oka, “Contour mapping of the spatio temporal state of polarization of light”, *Applied Optics* **33** (13), 2633-2636 (1994).
- [44] Kazuhiko Oka, Takayuki Kato, “Spectroscopic polarimetry with a channel spectrum”, *Optical Society of America* **24** (21), 1475-1477 (1999).
- [45] Haitao Luo, Kazuhiko Oka, Edward DeHoog, Michael Kudenov, James Schiewgerling and Eustace L. Dereniak, “Compact and miniature snapshot imaging polarimeter”, *Applied Optics* **47** (24), 4413-4417 (2008).

- [46] Gilbert Strang, "Computations With Matrices", *Linear Algebra and its applications* , Fourth Edition.
- [47] G.H.Golub and C.F.Van Loan, "Matrix Analysis", *Matrix Computations*, third edition, John Hopkins University Press, Baltimore, Maryland, (1996).
- [48] Amrit Ambirajan, Dwight C.Look, Jr., "Optimum angles for a polarimeter": part I, *Optical Engineering* **34** (6), 1651-1655 (1995).
- [49] Amrit Ambirajan, Dwight C.Look, Jr., "Optimum angles for a polarimeter": part II, *Optical Engineering* **34** (6), 1656-1658 (1995).
- [50] R.M.Azzam, I.M.Elminyaw, and A.M.El-Saba, "General analysis and optimization of the four-detector photo polarimeter", *Journal of Optical Society of America* **5** (5), 681-689 (1988).
- [51] K.M.Twietmeyer, R.A.Chipman, "Optimization of Mueller matrix polarimeters in the presence of error sources", *Optics Express* **16** (15), 11589-11603 (2008).
- [52] Sergey N.Savenkov, " Optimization and structuring of the instrument matrix for polarimetric measurements", *Optical Engineering* **41** (5), 965 - 971 (2002).
- [53] Matthew H.Smith, "Optimization of dual-rotating-retarder Mueller matrix polarimeter", *Applied Optics* **41** (13), 2488-2493 (2002).
- [54] D.S.Sabatke, M.R.Descour, E.L.Dereniak, W.C.Sweatt, S.A.Kemme and G.S.Phipps, "Optimization of retardance for a complete Stokes polarimeter", *Optical Society of America , Optics Letters* **25** (11), 802 - 804 (2008).
- [55] D.S.Sabatke, Ann M.Locke, M.R.Descour, John P.Garcia, E.L.Dereniak, W.C.Sweatt, S.A.Kemme and G.S.Phipps, "Figures of merit for complete Stokes polarimeter optimization", *SPIE proceedings* **4133**, 75 - 81 (2000).

- [56] J.Scott Tyo, “Design of optimal polarimeters: maximization of signal-to-noise ratio and minimization of systematic error”, *Applied Optics* **41** (1), 619 - 630 (2002).
- [57] J.Scott Tyo, “Noise equalization in Stokes parameter images obtained by use of variable-retardance polarimeters”, *Optical Society of America* **25** (16), 1198 - 1200 (2000).
- [58] Antonello De Martino, Yong-ki Kim, Enric Garcia-Caurel, Blandine Laude, and Bernard Drevillion, “Optimized Mueller polarimeter with liquid crystals”, *Optics Letters* **28** (8), 616-618 (2003).
- [59] Antonello De Martino, Enric Garcia-Caurel, Blandine Laude, and Bernard Drevillion, “General methods for optimized design and calibration of Mueller polarimeters”, *Thin Solid Films* **455-456**, 112 - 119 (2004).
- [60] Enric Garcia-Caurel, Antonello De Martino, and Bernard Drevillion, “Spectroscopic Mueller polarimeter based on liquid crystal devices”, *Thin Solid Films* **455-456**, 120 - 123 (2004).
- [61] Hamamatsu Learning Center: “CCD Noise Sources and Signal-to-Noise Ratio”, *Concepts in Digital Imaging Technology*, <http://learn.hamamatsu.com/articles/ccdsnr.html>.
- [62] David W.Tyler and Jason D.Mudge, “Signal, noise, and bias for broadband, division-of-amplitude Stokes polarimeter”, submitted to *Optical Society of America* (2010).

- [63] Haitao Lao, Kazuhiko Oka, Tomasz Tkaczyk, and Eustace L.Dereniak, “Modeling and optimization for a prismatic snapshot imaging polarimeter”, *Applied Optics*, **45**(33), 8400-8408 (2006).